



TECHNISCHE
UNIVERSITÄT
WIEN

DISSERTATION

Next Generation HE-NMC Cathodes for Advanced Lithium-Ion Batteries

ausgeführt zum Zwecke der Erlangung des akademischen Grades einer
Doktorin der technischen Wissenschaften
unter der Leitung von

Ao. Univ. Prof. Dr. techn. Peter Blaha
E165
Institut für Materialchemie

eingereicht an der Technischen Universität Wien
Fakultät für Technische Chemie

von

Katja Fröhlich
0525541
Obere Donaustraße 17/1/10, 1020 Wien

Datum

Unterschrift

Danksagung

Besonderer Dank gilt meinen KollegInnen im Batterieteam des AIT Austrian Institute of Technology GmbH für das gute Arbeitsklima und die gute Zusammenarbeit. Auch durch den stetigen Einsatz von Assoc. Prof. Atanaska Trifonova, meiner Betreuerin von Seiten des AIT, wurden die Rahmenbedingungen geschaffen, die für die vorliegende Forschungsarbeit notwendig waren.

Ich möchte mich zusätzlich recht herzlich bei meinem Betreuer von Seiten der Technischen Universität Wien, Prof. Blaha, bedanken, der mich immer prompt mit Ratschlägen und Lösungen unterstützt hat. Die Möglichkeit mit dem Entwickler des Programmes zusammenzuarbeiten war für mich von großem Wert und ohne diese hätte die Arbeit nicht zustande kommen können.

Außerdem möchte ich mich bei Dr. Isaac Abrahams von der Queen Mary University in London bedanken, wo ein Teil dieser Arbeit durchgeführt wurde. Während meines Austauschaufenthalts in London hat er mich stets unterstützt und hatte immer ein offenes Ohr für Diskussionen und Gespräche.

Privat möchte ich mich recht herzlich bei meiner Familie bedanken; allen voran meinen Eltern, deren stetige Unterstützung in jederlei Hinsicht mich so weit gebracht hat. Ein großes Danke auch an meinen Freund für die Zuversicht und den Zuspruch, die mir bei der Vollendung der Arbeit sehr geholfen haben.

Mein Dank gilt auch der Andritz AG sowie der österreichischen Forschungsförderungsgesellschaft (FFG) und dem Bundesministerium für Verkehr, Innovation und Technologie (bmvit), ohne deren finanzielle Unterstützung diese Arbeit nicht zustande gekommen wäre.

Katja Fröhlich

Kurzfassung

Lithium-Nickel-Mangan-Kobalt-Oxide (NMC) gehören zu den vielversprechendsten Kathodenmaterialien für den Einsatz in elektrischen Antrieben. Dieses Material wurde in symmetrischer Zusammensetzung hinsichtlich der Übergangsmetalle bereits kommerzialisiert und von verschiedenen Fahrzeugherstellern wie Ford, Fiat und Volkswagen erfolgreich eingesetzt.

In dieser Arbeit wurden theoretische und experimentelle Methoden vereint: Vorab wurden Elektronenstrukturen von symmetrischem NMC mittels Dichtefunktionaltheorie berechnet. Es wurden Bindungslängen, Einheitszellenparameter und magnetische Momente der einzelnen Übergangsmetalle simuliert. Zusätzlich wurden die Zustandsdichten bei unterschiedlichen Ladezuständen berechnet, um Änderungen der Elektronenstruktur während des Ladens der Batteriezelle darzustellen. Es zeigte sich, dass es bei der Ladeschlussspannung von 4,2 V zu einer Neuordnung der Kristallstruktur kommt.

Aufgrund dieser Berechnungen wurden zwei unterschiedliche Zusammensetzungen an NMC Kathoden synthetisiert: NMC111 (symmetrisch 1:1:1; Ni:Mn:Co), und NMC532 (nicht-symmetrisch 5:3:2; Ni:Mn:Co). Die Verringerung des Kobaltanteils zugunsten von Nickel führt nicht nur zu einer Erhöhung der Ladeschlussspannung, sondern auch zu einer Verringerung der Toxizität und Kosten des Batterieaktivmaterials. Es wurden außerdem günstigere, sonst eher unübliche Chloridpräkursoren zur Synthese eingesetzt, die in großindustriellen Prozessen herangezogen werden könnten.

Die Charakterisierung der symmetrischen NMC Kathoden zeigte, dass Sauerstoff während dem Syntheseprozess eine entscheidende Rolle spielt und jene Probe, die ausgehend von Chloriden hergestellt wurden, im Vergleich zur Nitratsynthese vergleichbare Werte zeigten. Im Gegensatz dazu zeigten nicht-symmetrische NMC Kathoden, welche einen deutlich höheren Nickelanteil aufweisen, beim Einsatz von Chloriden die Bildung von Nebenprodukten, welche zu signifikanter Kapazitätserniedrigung und erhöhten Anteil an Chlorverunreinigungen führten.

Am Ende der Arbeit wird ein verbessertes NMC532 Kathodenmaterial vorgestellt, welches ausgehend von Nitraten in sauerstoffreicher Atmosphäre synthetisiert wurde und mit vielversprechend hoher spezifischen Kapazität ($117,40 \text{ mAhg}^{-1}$) und Wirkungsgrad (99,54%) nach 100 Zyklen sowie selbst bei 4,5 V Ladeschlussspannung hohe Stabilität aufweist ($146,88 \text{ mAhg}^{-1}$ und 100% Wirkungsgrad nach 100 Zyklen).

Abstract

Lithium Nickel Manganese Cobalt Oxides (NMC) are among of the most promising cathode materials for automotive applications. With a symmetric composition of the transition metals, this material is already commercialized and applied by different car manufacturers in electric vehicles such as Ford, Fiat, and Volkswagen.

In this work, symmetric NMC cathodes were characterized using different approaches: First, electronic structure calculations using large super cell models were performed. The results picture bond distances and differences in terms of nearness between different transition metals. Additionally, density of states were calculated for different lithiation stages for understanding of electronic changes with state of charge during cycling of the battery cell. Structural rearrangement was observed at 4.2 V, which is the usually applied cut-off voltage.

Encouraged by these findings, two compositions of NMC cathodes were synthesized: NMC111 (symmetric 1:1:1; Ni:Mn:Co) and NMC532 (non-symmetric 5:3:2; Ni:Mn:Co). Decreasing the cobalt content in favor of nickel not just solely leads to better stability at higher cut-off voltages, but also decreases the toxicity and cost of the battery active material. Unusual precursors (chlorides) were additionally applied, which are low in cost and of industrial interest due to their possible usage in large-scale production techniques.

The characterization of symmetric NMC cathodes revealed that oxygen content plays a crucial role during the synthesis process and chloride prepared samples show similar results compared to usual nitrate precursors, especially at higher temperatures. In contrast, for non-symmetric NMC, which has a significantly higher amount of nickel, the application of chloride precursors leads to irreversible formation of byproducts which remain in the structure, lead to significant capacity decrease and a higher amount of chloride impurities.

In the end it was shown that NMC532, synthesized using nitrate precursors, showed encouragingly high specific capacity (117.40 mAhg^{-1}) and efficiency (99.54%) after 100 cycles when synthesized under flowing oxygen-rich atmosphere, even when being cycled up to 4.5 V (146.88 mAhg^{-1} and 100% efficiency after 100 cycles).

*Und soll mein Denken zu etwas taugen
Und sich nicht nur im Kreise drehen
Will ich versuchen mit euren Augen
Die Wirklichkeit klarer zu sehen*

Hannes Wader

Contents

1	Introduction	1
1.1	Motivation	1
1.2	Objective	2
1.3	Outline	3
2	Lithium-ion batteries and materials	5
2.1	General remarks	5
2.2	Electrolytes	8
2.3	Anode materials	10
2.3.1	Lithium metal	10
2.3.2	Graphite and other carbonaceous materials	10
2.3.3	Lithium Titanium Oxide (LTO)	11
2.3.4	Silicon	11
2.4	Cathode materials	12
2.4.1	Layered structures	12
2.4.2	Olivines	14
2.4.3	Spinel	15
2.4.4	Cathode material characterization and improvement from first principles	16
3	Electronic structure calculations	19
3.1	Methods	19
3.1.1	Density functional theory	19
3.1.2	WIEN2k code	22
3.1.3	Preliminary studies	23
3.1.4	Li-NMC Supercell	30
3.2	Results and Discussion	33
3.2.1	Super cell structures at different states of lithiation	33
3.3	Conclusion	47

4	Syntheses	48
4.1	Coprecipitation method	48
5	Physico-chemical characterization	50
5.1	Methods	50
5.1.1	Gas adsorption measurements	50
5.1.2	Laser diffraction analysis	52
5.1.3	Scanning electron microscopy (SEM)	52
5.1.4	Transmission electron microscopy (TEM)	53
5.1.5	Inductively coupled plasma optical emission spectrometry (ICP-OES)	53
5.1.6	X-ray photoelectron spectroscopy (XPS)	53
5.1.7	X-ray diffraction (XRD)	54
5.2	Results and Discussion	56
5.2.1	Symmetric NMC	56
5.2.2	Non-symmetric NMC	66
5.3	Conclusion	75
6	Electrochemical characterization	77
6.1	Methods	77
6.1.1	General concepts	77
6.1.2	Slurry and half cell preparation	79
6.1.3	Cyclic voltammetry (CV)	80
6.1.4	Cycling tests	81
6.1.5	Galvanostatic Intermittent Titration Technique (GITT)	82
6.1.6	<i>Ex Situ</i> X-Ray Diffraction Analysis	84
6.2	Results and Discussion	85
6.2.1	Symmetric NMC	85
6.2.2	Non-symmetric NMC	101
6.3	Conclusion	110
7	Conclusions and further perspective	112
7.1	Conclusions	112
7.2	Further perspective	114

1 Introduction

1.1 Motivation

Environmental matters and the associated reduction of greenhouse gases are among of the most important issues nowadays. The increase of renewable energy sources and emission reduction in the automotive sector are key targets towards a greener future. Electrical energy storage is strongly linked to many aspects of this.

Increasing demand of worldwide electricity requires a greater share of energy from renewable resources in our grids. Electricity generation is now mostly delocalized from consumer needs. When a high amount of renewable energy shall be available while electricity demand is constantly rising, long-term energy storage will be needed, which also implies a need for very large storage capacities.

Additionally, cities all over the world play a key role with respect to emission restrictions and further electrification of the automotive sector: in order to reduce local emissions and particulate pollution, many cities have been establishing a low emission zone within their centers (within Europe, for example: London, Paris and large parts of Norway) [1].

If both goals - growth of renewable energy resources and electrification of the automotive sector - are achieved, electric drives are a great step towards a greener future. Both sectors can be linked to each other.

For example, to ensure optimal usage of electric power in smart grids, electric drives can be used and integrated as an additional storage system. If a photovoltaic system is integrated into a household with electric drives, the electric vehicle (EV) can be integrated into the grid as an additional electrical energy storage system, buffering and saving energy from the grid in peak-times during fluctuations [2].

So far, the market share of electric vehicles in the overall automotive sector is limited. This is caused by several factors, for example short driving ranges, lack of charging infrastructures (especially in sparsely populated areas), long charging times and above all the high costs, which are dominated by the battery system.

The market of electric vehicles and hybrid technologies (plug-in oder range extended versions) is strongly connected to the battery market [3]. Li-ion batteries are nowadays the worldwide leading battery cell chemistry in mobile applications. Nearly all small electronic devices include secondary batteries based on Li-ion technology.

Lithium, being highly reactive and the lightest and most electropositive alkali metal, is the best candidate for building light-weight electrochemical energy storage systems. The costs of Li-ion batteries are influenced by the cathode more than by any other components including packaging, and therefore not only the cell chemistry but also the industrial synthesis route of the corresponding materials are a great influencer regarding the overall battery costs [4] [5].

The requirements for battery cell chemistries for electric drives are different from other applications, especially in terms of safety, costs, and energy density. By 2030, the worldwide leading cell chemistry is expected to be completely different than current ones. Several cell chemistries are candidates for meeting future market requirements; among them, mixed metal oxides (especially combinations of nickel, manganese and cobalt) have strong chances of becoming the next generation cathode material.

1.2 Objective

Lithium nickel manganese cobalt oxide, abbreviated as NMC, is one of the most promising cathode materials for application in electric drives. This cathode material, with symmetric composition of the transition metals, has a high specific capacity (practically up to 180 mAhg^{-1}), but a low lifespan and power density. Due to its layered structure it provides optimal diffusion pathways for fast lithium intercalation and deintercalation during charging and discharging.

NMC has two different working plateaus: at higher voltages (3.8 until 4.2 V) it shows excellent storage capacity and low costs per kWh. Anyway, the application of higher potentials reduces this advantage after long term cycling and leads to irreversible capacity fading. At lower voltages (3.0 until 3.8 V) the storage capacity is lower and therefore also the costs per kWh increase, but the cycle stability is higher compared to cycling at higher voltage ranges.

Another challenge is the cation mixing: due to the similar ionic radii of Ni^{2+} and Li^+ , they tend to share sites to a certain extent. Therefore, some lithium is trapped in the structure and cannot be intercalated and deintercalated. This further leads to shortening of the lifetime of the battery cell. Cation mixing mainly occurs during synthesis of the material and therefore, the conditions are to be monitored accurately.

All these phenomena are directly linked to the micro- and crystal structure of the material and therefore also to the synthesis conditions (choice of precursor, temperature, method).

The aim of this work is the improvement of this very promising cathode material as the future material of choice with main focus for application in electric drives.

To fully understand structural failure and capacity fade with cycling, different syntheses of symmetric and non-symmetric NMC were performed under various conditions and then characterized physico-chemically. Electronic structure calculations assist in understanding crystal structure changes during cycling as well as oxidation states and distribution of the transition metals for charge compensation. Chosen materials were additionally characterized electrochemically, and correlations between their performance, characteristics and synthesis conditions were drawn.

1.3 Outline

This thesis consists of three main parts: electronic structure calculations, physico-chemical characterization, and electrochemical characterization. An introduction into lithium-ion batteries and commercialized materials at the beginning and final conclusions round out the work. The syntheses methods, materials and conditions are described in an additional section after the introduction. The applied analytical methods are introduced and described in the corresponding sections and the results are presented and discussed.

The WIEN2k code was used for electronic structure calculations of NMC at different stages of lithiation, which correspond to specific points in state of charge during cycling of the battery. Lithium cobalt oxide was chosen to determine optimized input parameters, and different super structures were calculated to reduce the number of atoms at the beginning and evaluate differences in stability for different metal ordering. Based on these calculations, a so-called "super cell" of NMC was created as a final model.

Optimized crystal parameters at different stages of lithiation were calculated and used for further monitoring of structural changes, density of states with main focus on contribution of transition metal states, magnetic moments, bond lengths and unit cell parameter variation during cycling of NMC.

Different symmetric and non-symmetric NMC samples were synthesized and characterized physico- and electrochemically.

For physico-chemical characterization, following methods were applied:

- Gas adsorption (specific surface area & porosity)
- Laser diffraction (particle size distribution)
- X-ray diffraction (crystallography)
- Scanning electron microscopy (optical evaluation)
- Transmission electron microscopy (plane distance)
- Inductively coupled plasma optical emission spectroscopy (composition)
- X-ray photoelectron spectroscopy (oxidation states)

Electrochemical measurements were performed for chosen NMC material, to obtain their real specific capacities, cycle stability, diffusion coefficients and cycling performance. All these measurements were performed in half cells versus lithium metal, using LP30 as standard electrolyte, in order to avoid unwanted side effects or phenomena which might be caused by other battery components.

Ex situ crystallographic analysis of cycled cathodes via Rietveld fit of recorded X-ray diffraction pattern is presented. Therefore, cyclic voltammetry measurements were stopped at different stages of lithiation and the cathode structure was analyzed. The resulting unit cell parameters are in good agreement with the optimized super cell model of NMC as derived by application of density functional theory.

Conclusions are drawn at the end of the thesis. The influence of different synthesis parameters on the performance of these cathode materials is evaluated and the results are presented. Additionally, future perspectives based on this work and NMC as promising cathode material are discussed.

2 Lithium-ion batteries and materials

2.1 General remarks

The lithium-ion battery is the world's leading battery system and is used in various fields, such as mobile applications (notebooks, phones, coin cells...), stationary applications and in electric or hybrid-electric vehicles. The first commercially available lithium-ion technology was patented by Peter Busch in 1989 [6] and used by Sony for the Hi8 Camcorder CCD TR1; it consisted of two cells having a capacity of 1200 mAh.

Secondary batteries generally consist of a positive electrode (cathode) and a negative electrode (anode), both inserted into an electrolyte and separated by a separator to prevent short-circuits (see Figure 2.1). In commercial lithium-ion batteries, the anode consists mostly of carbonaceous materials (for example graphite) on a copper current collector, while on the cathode side different active materials such as mixed or single transition metal oxides or phosphates on an aluminium current collector are in use. The electrolyte is aprotic and contains a lithium salt to provide good ionic transport for the lithium ions to move from one side to the other during charging/discharging of the cell. Due to the reactivity of the electrolyte with the carbonaceous anode in the regarding voltage window, a stable solid-electrolyte-interface (or phase, also referred to as SEI) is built during the formation process at the anode side. This interface can be altered with different additives in the electrolyte to provide good diffusion of the lithium ions through the phase.

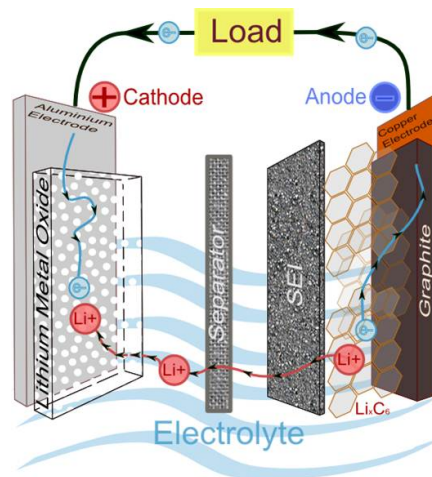
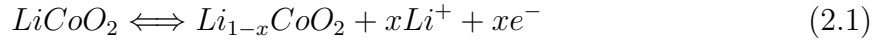


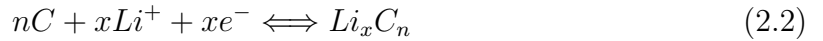
Figure 2.1: Schematic working principle of Li-ion batteries.

When the cell is fully charged, the anode side is fully lithiated while the cathode side is delithiated. The amount of lithium remaining in the host structures depends on their corresponding stability; e.g. for lithium cobalt oxide, only half of the lithium can be reversibly extracted. When the cell is discharged, lithium moves from the negative electrode (anode) to the positive electrode (cathode). First, the lithium ion is deintercalated from the anode host matrix and diffuses to the surface of the particle. The lithium ion is solvated in the liquid phase (electrolyte) after passing through the SEI layer, leaving an electron behind in the anode structure. This electron meanwhile migrates through the external circuit and the consumer (load) to the cathode side, where it meets the lithium ion again to ensure electroneutrality within the host matrix. Therefore, the electrode materials has to be stable in different oxidation states, depending on the chemical formula.

Assuming lithium cobalt oxide (LiCoO_2) and graphite (C_6) as positive and negative electrode materials, the reactions at the cathode can be described as:



The reactions at the negative electrode are:



Combining these reactions leads to the overall cell reaction:



These electrochemical reactions take place at the corresponding interfaces between the electrodes and the electrolyte. To provide large active reaction areas at the cathode and anode sides, the electrodes have porous structures soaked with electrolyte. The porosity of the electrodes depends on the specific surface areas of the active materials - type of material and synthesis conditions - as well as the formulation of the electrodes, which also contains additives for better electrical contact (carbon) as well as binder materials to combine them and stick them to the current collector. Additionally, the porosity is altered through the electrode fabrication method - via coating, rolling, pressing, and heat treatment - to achieve a final porosity of 50 - 70%.

Many different combinations of cathode and anode materials are already commercialized and well-established in their corresponding fields of application. The compositions and properties of the most important cathode materials are summarized in Table 2.1 [7].

Table 2.1: Commercialized cathode materials and their characteristics.

Chemical formula	Code	Voltage vs. Li/Li ⁺ [V]	Spec. capacity (theory/real) [mAhg ⁻¹]	Safety	Cost
LiCoO ₂	LCO	3.8	274/148	-	-
LiNi _{1/3} Mn _{1/3} Co _{1/3} O ₂	NMC	3.8	278/160	~	~
LiMn ₂ O ₄	LMO	4.1	148/120	~	+
LiFePO ₄	LFP	3.4	170/140	+	+
LiNi _{0.8} Co _{0.15} Al _{0.05} O ₂	NCA	3.8	279/199	-	-

The advantages of lithium nickel manganese cobalt oxide (NMC) over other commercialized cathode materials are clear: relatively high safety, low cost, high specific energy density, and high operation voltage. NMC combines the advantages of the incorporated transition metals - nickel for specific energy, manganese for cost and cobalt for stability.

The reduction of the cobalt proportion within the structure further improves the material in terms of costs and safety, especially for industrial production of the active powders. Much research regarding composition variations in terms of cobalt reduction and nickel enhancement was therefore performed and is still ongoing [8] [9] [10].

NMC as one of the most promising commercial cathode materials is of great interest for automotive applications since it already meets the main requirements. Further variation of the transition metals ratio can improve its energy density, cost and safety.

2.2 Electrolytes

The electrolyte is very important for the efficient operation of any battery and plays a key role in providing fast ionic transfer and good cycle performance. Electrolytes with low lithium ion transport numbers and diffusion coefficients may cause large concentration polarizations during operation of Li-ion batteries which lead to poor high-rate performance, unwanted side reactions, and faster ageing [11] [12] [13].

The requirements for electrolytes include

- good solubility of the salt in the solvent
- large electrochemical window
- good wettability of the electrodes and the separator
- high thermal stability (low melting, high boiling point, high flash point)
- high conductivity of the ions in the solvent
- low viscosity
- low toxicity
- low cost

Overall, the major requirement is chemical stability in the operation voltage as the electrolyte is in contact with all other components of the battery system (see figure 2.2).

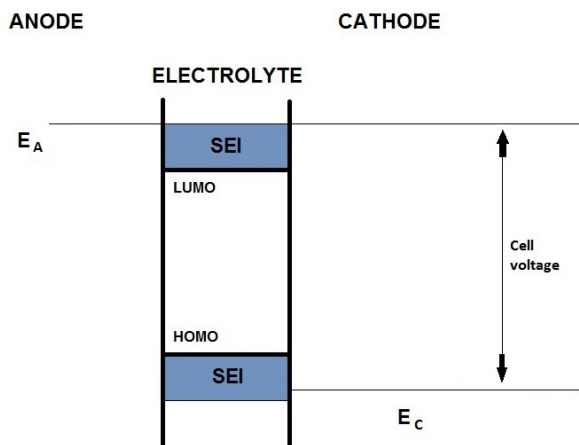


Figure 2.2: Electrochemical window of the electrolyte (recreated from [14]).

The electrolyte mainly consists of a solvent or, as in most cases, a mixture of different solvents and the corresponding conducting salt. State-of-the-art electrolytes for Li-ion battery systems mostly are non-aqueous. The solvents are organic carbonates such as ethylene carbonate (EC), dimethyl carbonate (DMC), diethyl carbonate (DEC), propylene carbonate (PC), and/or ethyl methyl carbonate (EMC). Lithium hexafluorophosphate (LiPF_6) as conducting salt is dissolved in the solvent. Even though thermal stability is poor and small water residues can lead to HF formation, no replacement of LiPF_6 with another substance is expected to take place in the near future. Possible other salts are LiClO_4 , which is highly explosive and not applicable for mixed oxide cathodes, LiAsF_6 , which is toxic, or LiBF_4 , which leads to passivation on the anode [12].

The major drawback of commercial organic carbonates besides their high flammability is their instability at higher voltages, i.e. when the cell is charged above 4.5 V. As research is going towards high voltage and high capacity materials (which increase the risk of ignition), extensive research into possible replacements for the conventional non-aqueous solution electrolytes is done by various groups [15] [16] .

One possibility would be the use of ionic liquids, which enhance the safety and stability of the battery cell under harsher conditions. Ionic liquids are salts with low melting points, caused by the strong interaction of the organic groups with the salt to reduce the ability to form stable crystal lattices. Common cations are quaternary ammonium cations with alkyl substituents (for example EMIM), while a variety of anions exist, such as perfluoroanions, TFSI... . Still, ionic liquids don't meet the major requirement for commercial applications. Their mayor drawback is the electrostatic interaction of Li^+ with the anion, which leads to slow desolvation of lithium [17]. Additionally, the viscosity of ionic liquids is very high, which leads to higher internal resistance compared to conventional solvents.

Other advances, such as solid electrolytes, have many advantages like no side-film formation or passivation of the electrodes or current collectors, no need for separators, high safety and flexible battery design. On the other hand, solid electrolytes suffer from low ionic conductivity compared to liquid ones, and the internal resistance is very high. Therefore, the developments in the field are still far away from market readiness [18].

Overall, the composition of future electrolytes is strongly linked to the electrode materials in use and therefore development and research on both must be strongly linked.

2.3 Anode materials

2.3.1 Lithium metal

Having the highest theoretical capacity among other materials, lithium metal was the first anode material used in Li-ion battery cells. It has many advantages such as lightweight, highest specific capacity, maximum cell voltage, and no need for a host matrix for lithium intercalation. Electrode fabrication is simple due to its compact design, and lithium is a good reducing agent, providing high conductivity and mechanical stability.

Unfortunately, the deposition of lithium during charging is disordered, leading to a mossy structure and dendrite formation. These spikes which arise during cycling can lead to short circuit of the cell when they penetrate the separator towards the cathode side. Additional efforts have been made, especially when using a polymer electrolyte, to suppress dendrite formation. Still, due to safety issues, no commercial anode is made of lithium metal and research progressed to less hazardous materials [19].

2.3.2 Graphite and other carbonaceous materials

Due to the challenges using lithium metal as anode, the use of carbonaceous intercalation materials instead of lithium metal was established. The first research on graphite as negative electrode was performed by Yazami et al [20]. Graphite consists of graphene layers, which provide optimum two-dimensional pathways for lithium ions to intercalate and de-intercalate between them.

To date, graphite is one of the most commonly used anode materials in commercial lithium-ion secondary batteries. Nevertheless, there are some disadvantages in this material. First, side-film formation occurs within the first cycles which absorbs a substantial amount of the whole cell capacity (10 - 20%). This is caused by electrolyte decomposition at the low operating voltage of the anode, which leads to formation of a thin layer (solid-electrolyte interphase, SEI) between the electrode and electrolyte. This layer grows within the first cycles in a so-called formation process and is nowadays altered by different additives to the electrolyte. The layer is electronically insulating but ion-conducting for lithium-ions to pass. As the volume expansion of graphite during cycling is relatively low (around 10%) compared to high-capacity anode materials such as silicon, the SEI is not altered much during the subsequent cycles.

As the theoretical capacity of graphite (372 mAhg^{-1}) is nearly fully attained and its volumetric capacity is still low, other anode materials are being investigated. The main attempts are made in the field of using other carbon materials, such as carbon nanotubes (CNT) [21] - as arrays or as a mixture with metal oxides, single-walled or multi-walled. The idea is to enlarge the reaction surface area, which consequently also includes a larger area for side-film formation and enhances the capacity loss of the respective materials. Graphene layers and graphene oxides are of great interest for electrochemical applications [22], but their synthesis method is difficult to set up for large scale production and their volumetric capacity is still low.

2.3.3 Lithium Titanium Oxide (LTO)

Lithium titanate ($\text{Li}_4\text{Ti}_5\text{O}_{12}$) - LTO - is another already commercialized anode material. The advantages of this spinel are its high thermal stability and low cost. Additionally, the operating voltage above 1 V suppresses the decomposition of the electrolyte and side-film formation, and the corresponding capacity loss within the first cycles is therefore not an issue. Also the volume changes of LTO are very small and the cycleability is very high [23] [24]. Unfortunately, the theoretical specific capacity (175 mAhg^{-1}) of this anode material is low, and the high lithium ion intercalation potential leads to a smaller operating window of the battery compared to graphite and consequently to significant losses in the energy content. Their application is therefore limited to safe high power, long cycle life, but low energy batteries [7].

2.3.4 Silicon

Silicon is one of the most promising future anode materials. It offers very high specific capacity (theoretically 3579 mAh^{-1}) and can take up to 3.75 moles Li per mole Si. Silicon belongs to the alloying electrodes which are, in contrast to graphite and LTO, not intercalation electrodes but react with lithium when being charged or discharged. This is the reason for the large volume expansion during cycling, which leads to particle cracking, pulverisation, and loss of electrical contact between the single components of the anode [25]. Additionally, there is a side-film formation similar to the SEI on graphite anodes, which is permanently altered due to particle cracking and volume changes and therefore contributes to permanent capacity loss.

This happens in such that particle cracking further leads to formation of new surfaces which consequently again to be passivated during cycling. This means more electrolyte reduction at the arisen surfaces, resulting in continuous irreversible capacity losses. To prevent this, surface coating of silicon, combined with carbon and composites, or application of alloys; which means blending of silicon with carbonaceous materials, is state-of-the art in this research field [26].

2.4 Cathode materials

2.4.1 Layered structures

Layered structures were among the first cathode materials studied. Their layers provide fast two-dimensional diffusion paths, which are favorable for lithium-ions. The first commercially available layered transition metal oxide was LiCoO_2 (LCO), which was invented by Goodenough et al. [27].

Layered metal oxides have typically $R\bar{3}m$ symmetry of the $\alpha\text{-NaFeO}_2$ structure. The transition metal oxide layers consist of MO_6 octahedra, where the oxygen anions form a close-packed cubic lattice. Oxygen occupies 6c sites, while lithium prefers 3b sites. Metals, for example cobalt in LCO, are placed on 3a sites (see Figure 2.3).

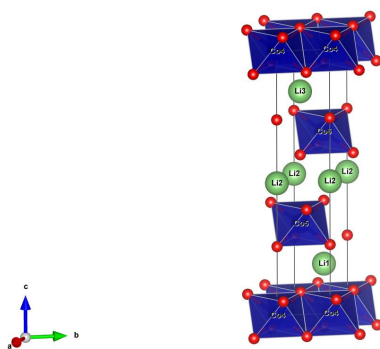


Figure 2.3: Three dimensional image of the structure of LiCoO_2 .

Cobalt is toxic, expensive, has low thermal stability, and is classified as critical raw material (CRM) by the European Commission [28]. Therefore, extensive research has been performed to replace it partly or fully with other transition metals. First, the research concentrated on nickel oxides. LiNiO_2 (LNO) theoretically offers similar energy density as the cobalt-containing intercalation electrode and is much cheaper. However, there are several disadvantages. First, bivalent nickel has a similar ionic radius as the monovalent lithium ion, which leads to so-called cation mixing during synthesis and cycling [29]. This leads to passivation of the diffusion pathways of lithium ions and therefore drastically reduces capacity. Additionally, LiNiO_2 is difficult to synthesize in pure form.

Manganese is even cheaper and more environmentally benign compared to nickel and cobalt; therefore, research was performed for replacement of cobalt with manganese [30]. LiMnO_2 offers up to 200 mAhg^{-1} within the first cycle, but the capacity decreases rapidly after few cycles. There are several reasons for this: first, the instability of the Mn^{3+} ion, which disproportionates into Mn^{2+} and Mn^{4+} during delithiation and leads to further dissolution of manganese in the electrolyte. Additionally, LiMnO_2 is not stable and tends to form the spinel phase LiMn_2O_4 [31] [32].

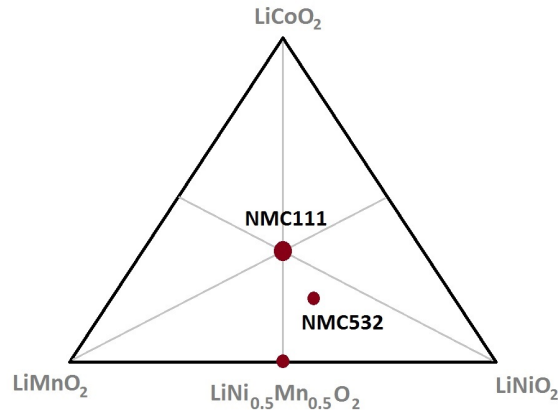


Figure 2.4: The ternary system between LCO, LNO and LMO.

In order to combine the advantages of the mentioned transition metals, mixtures of these transition metal oxides discussed above were studied. The symmetric combination of nickel and manganese oxide leads to $\text{LiNi}_{0.5}\text{Mn}_{0.5}\text{O}_2$, which consists of Ni^{2+} and Mn^{4+} ions.

This combination is very interesting, as only nickel is electrochemically active and oxidized up to 4+ during charging [33]. As manganese remains inactive in the 4+ oxidation state, the effect of unstable manganese in lower oxidation states is suppressed. The main drawback of this material is the high amount of cation mixing (similar to LNO), which was already discussed above and leads to low practical capacity of the cathode. The next step in research was to introduce also cobalt into the structure as well, to decrease cation mixing and increase capacity, which leads to $\text{LiNi}_{1/3}\text{Mn}_{1/3}\text{Co}_{1/3}\text{O}_2$ (NMC) (see Figure 2.4).

This material offers a wide range of advantages such as high energy density, high capacity, relatively low cost, and safety. Even though the effect of cation mixing is still present, due to the lower nickel content it is much lower compared to $\text{LiNi}_{0.5}\text{Mn}_{0.5}\text{O}_2$, and the voltage plateau is flat, which makes it more attractive for commercial applications [34] [35] [36].

2.4.2 Olivines

Olivine type structures, for example the already commercialized LiFePO_4 (LFP), were investigated in order to reduce costs and enhance safety, which are both important issues for automotive applications. LFP was first discovered in 1997 by Padhi et al [37].

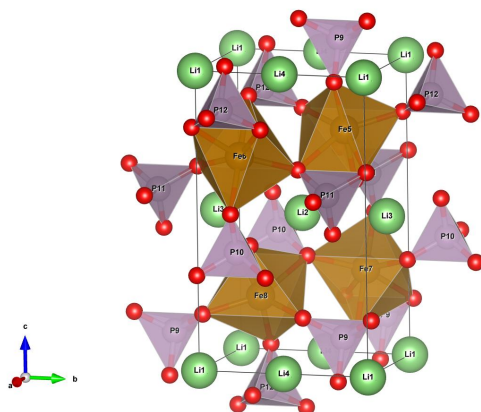


Figure 2.5: Three dimensional image of the structure of LiFePO_4 .

Olivines have typically $Pnma$ symmetry and an orthorhombic crystal system. In LFP, lithium and iron ions occupy octahedral sites, while phosphorus occupies tetrahedral sites. The olivine frame network provides one-dimensional pathways for Li^+ intercalation and deintercalation (see Figure 2.5).

The strong covalently bonded oxygens in the phosphate group lead to high thermal stability of the compounds, which would make LiFePO_4 (LFP), the most widely studied polyanionic cathode material, an attractive candidate for applications in electric vehicles. Olivine structure type LiMPO_4 have considerable advantages when it comes to rate capability, safety, and stability. Unfortunately, they suffer from poor electronic and ionic conductivity and small operating voltage window [38]. Different other transition metals were introduced, for example cobalt, manganese, nickel, or combinations of them. However, they all suffer from (sometimes even lower) conductivity, even though some show higher capacity compared to LFP [39] [40].

To improve the conductivity, the electrode formulation includes more conductive carbon than for other cathode materials. The need of adding more non-active material than usual for conductivity enhancement leads to low packing density. LFP is therefore additionally a less attractive option for future automotive applications.

2.4.3 Spinel

The next group of cathode structures includes spinels. The most common and already commercialized spinel is LiMn_2O_4 , which was widely studied by Thackeray et al. in 1997 [41]. In this Fdm3m symmetry, manganese occupies octahedral sites and lithium is located at tetrahedral sites in cubic closed packaged oxygen anion array. The lithium can diffuse in three dimensions through vacant tetrahedral and octahedral sites in the cubic framework (see Figure 2.6).

The lithiated manganese oxide in spinel structures, offers the highest average discharge potential, which is 4 V versus lithium. Additionally, manganese is non-toxic and low cost compared to cobalt or nickel compounds. However, this material suffers from low energy density and the disproportion of trivalent manganese according to the following reaction [42]:



which leads to dissolution of bivalent manganese in the electrolyte and further capacity loss [43]. Additional phase transition to $\text{Li}_2\text{Mn}_2\text{O}_4$, especially at the particle surfaces, decreases the cycleability of the manganese oxide spinel. In order to reduce this effect, mixtures and blends with layered oxides are applied with promising results [44].

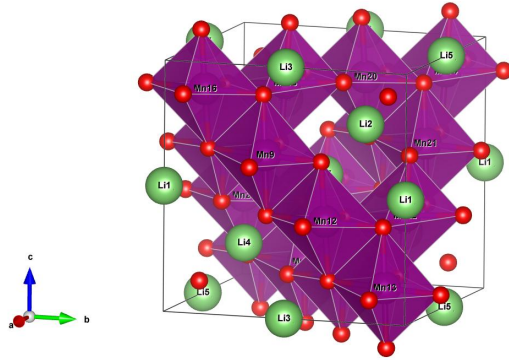


Figure 2.6: Three dimensional image of the structure of LiMn_2O_4 .

LiMn_2O_4 nowadays has its commercial applications in the field of power tools. Additionally to this, LMOs can be found in several commercially available cells as blends with layered oxides - for example NMC.

2.4.4 Cathode material characterization and improvement from first principles

Development and design of battery materials requires deep understanding of the relation between their chemistry, structure, and properties. *Ab initio* calculations provide information from which the materials' usability in electrochemical cells can be predicted and further details about their structure and stability are obtained. The main advantage of this approach is that no experimental input data is needed (except some knowledge about the structure), and therefore, personal and material costs are greatly reduced.

This work concentrates on electronic structure calculations based on density functional theory, which is nowadays implemented in different codes such as VASP [45], Quantum Espresso [46], and WIEN2k [47], to name just a few of them. They differ in the treatment of the electrons (pseudopotentials versus all-electron) as well as the basis sets (plane waves versus augmented plane waves), which leads to differences in accuracy of electronic structure predictions.

Many scientists use first principles calculations for cathode material design, characterization, and enhancement. Ceder et al. calculated phase diagrams of different lithium transition metal oxides to predict phase transitions during cycling [48].

His early work mostly concentrates on LiCoO_2 , an already commercialized layered oxide cathode material [49]. In early simulations, he calculated the intercalation voltage curve, the free energy of formation as a function of lithium content, and, as already mentioned, phase diagrams.

Some applications for *ab initio* calculations shall be pointed out here. One is the evaluation of the effect of different dopands or polyanionic substitution, where the densities of states are compared and evaluated to find the optimal dopand or substitute [50] [51] [52]. The average voltage of lithium intercalation is usually underestimated by first principles simulations, but still useful for pre-screening and comparison of different possible host structures [53] [54]. This approach is also applied when new cathode materials for lithium-ion batteries or future battery systems such as magnesium-ion or sodium-ion systems are evaluated [55] [56] [57].

Ab initio studies of coatings, surfaces, or even interfaces are more tricky as one has to have a good idea of what the crystal structure at the surface looks like, which requires an educated guess and/or experimental data. Supercells with sufficiently large vacuum regions to avoid neighbouring effects above the surfaces are therefore created and calculated [58] [59].

When it comes to NMC, many simulations have already been performed in the field, as this cathode material is already commercialized. Caused by the symmetric mixture between the transition metals, which equally share (mostly, not taking into account the lithium-nickel cation mixing) 3a sites in the structure, the minimum size of calculated super cells contains three formula units.

An early example for a combined study of NMC was given by Hwang et al. in 2003 [60]. In this work, they proposed the oxidation states of nickel, manganese and cobalt to be 2+, 4+ and 3+, respectively, from *ab initio* simulations and proved the results with X-ray absorption near-edge spectroscopy (XANES) of sol-gel synthesized materials.

However, the results regarding nickel oxidation states during cycling are not consistent for different groups and approaches [61] [62]. Miao et al. combined electron energy loss spectroscopy (EELS) with first principles calculations and concluded that charge compensation during lithiation occurs at hybridized 2p states of oxygen atoms [63].

A reason for the differences between the computational and the experimental results may lie in the sample preparation for microscopic or spectroscopic analysis which often includes crushing the active materials in a mortar, and possible air exposure while transferring the sample to the equipment.

Another important point is the usage of small unit cells for their calculations, which included a maximum of three formula units of NMC. The small number of atoms included in these calculations implies the assumption of high symmetry or ordering, which does not seem representative for real crystal structures.

In this work, the number of atoms in the final model is very high (108 atoms in total) and the ordering of the transition metals is completely random. In that way, one can clearly see the effect of neighbouring atoms and draw concrete conclusions about different stages of lithiation and the effect on the local electronic structure, which, to the author's knowledge, has not been performed yet.

3 Electronic structure calculations

Computational methods like *ab initio* calculations are a very powerful tool for evaluation of existing and future intercalation host structures for Li-ion batteries. The gained information can greatly improve our knowledge about the calculated structures, and therefore reduce the optimization time. Due to the independency from experimental data, first principle calculations build an efficient complementary tool to laboratory work.

In this work, the WIEN2k code, based on density functional theory for solving the Schrödinger equation for solids, was used to predict structural changes, density of states, and stability during cycling and finally draw conclusions regarding the redox processes of the transition metals during cycling.

3.1 Methods

3.1.1 Density functional theory

As lithium insertion compounds, in this particular case lithium transition metal oxides, are complex solid systems, solving the Schrödinger equation to obtain a solution for the many-body plane wave function Ψ is not straight-forward. Many-body systems implies here the coexistence of heavy, positively charged particles (nuclei) and light, negatively charged particles (electrons). Therefore, some approximations are necessary when solving the time-independent Schrödinger equation [64]:

$$\hat{H}\Psi = E\Psi \quad (3.1)$$

Where \hat{H} represents the Hamiltonian operator, Ψ the wave function, describing the electrons in the many-body system, and E the total energy of the solid in the ground state. The Hamiltonian operator contains the kinetic energy of all particles as well as all electrostatic potential terms and is the quantum mechanical counterpart to the Hamilton function.

Due to their large mass difference, the movements of the nuclei are much slower and can therefore be fixed in contrast to the fast electrons surrounding them. This is called Born Oppenheimer Approximation [65] and leads to the first simplification in the Schrödinger equation.

The nuclei are fixed, their kinetic energy remains zero and we are dealing with the kinetic energy of the electrons, e^-e^- and e^- -nuclei interactions, which are determined as a function of the nuclear positions. Still, for a ne^- system, the many-body wavefunction $\Psi(x_1, x_2, \dots, x_n)$, which depends on the coordinates x_n of all e^- , is a very complex function and cannot be obtained for realistic systems.

Hohenberg and Kohn showed that the total energy of an interacting inhomogeneous electron gas (as in solids) is a functional of the electronic density and can in principle be described exactly without solving the Schrödinger equation [66]. This would simplify the calculation of the total energy E , but unfortunately the functional form is unknown.

In 1965, Kohn and Sham reformulated the equations, which lead to a practical scheme of the density functional theory [67]. They decomposed the unknown functional and set up the so-called Kohn-Sham equations, which are single-particle Schrödinger-like equations, describing an effective non-interacting system (quasi-particles) that moves in an external potential producing the same total density as the original many-body system.

The form of these equations in atomic units is

$$\left[-\frac{1}{2} \nabla^2 + V_{ext}(\vec{r}) + V_C[\rho(\vec{r})] + V_{xc}[\rho(\vec{r})] \right] \Phi_i(\vec{r}) = \epsilon_i \Phi_i(\vec{r}) \quad (3.2)$$

These terms represent the kinetic energy of non-interacting electrons, $\left(-\frac{1}{2}\nabla^2\right)$, the external potential - the nuclear potentials $\frac{Z}{r}$, $(V_{ext}(\vec{r}))$, the classical Coulomb potential of the electrons $\frac{\rho(r)}{r}$, $(V_C[\rho(\vec{r})])$, and the exchange-correlation potential, (V_{xc}) . The last term contains all quantum mechanical contributions, and since the exchange-correlation functional is also not known exactly, it must be approximated. Nevertheless, the other three terms are dominating compared to V_{xc} , which makes the method reasonably accurate.

These equations can now be solved iteratively to obtain self-consistency; where in the first cycle the starting density ρ_0 is guessed from the atomic densities and the equations are solved to obtain the corresponding wave functions Φ_1 , whose density ρ_1 is again calculated. The starting density ρ_2 for the next cycle is obtained by mixing the obtained densities in previous steps. This procedure is repeated until the density changes are insignificant and/or another pre-defined stop criterion is reached [68].

As already mentioned above, the exact exchange-correlation potential is unknown and must therefore be approximated. A lot of research was performed and is still ongoing regarding this topic, encouraged and further improved by steadily increase of computer performance and efficiency. Two different types of approximations are to be mentioned here: the local density approximation (LDA), in which the exchange-correlation energy density is approximated by that of the homogenous electron gas. In this case, the exchange part is known analytically while the correlation term was determined numerically by a Monte Carlo Method [69] and fitted to some simple functions [70] .

An extension of this approach is the generalization gradient approximation (GGA), where not only the local density $\rho(r)$ also the gradient $\frac{d\rho(r)}{dr}$ is included in the functional. Many different GGAs have been developed, often optimized for some systems (e.g. organic chemistry) or some properties (energies, geometries).

The Kohn-Sham equations are solved using the variational principle and the wave functions are obtained as linear combination of some basis functions:

$$\Phi_i = \sum_n c_n \phi_{in} \quad (3.3)$$

Plane waves form a complete basis set, but in principle such a basis would never converge. Two approaches for treatment of basis sets are to be mentioned here:

- **Pseudo potentials**

Pseudo potentials were introduced to cut off the strong nuclear potential in the core regions of atoms by Hellmann in 1935. In this core region, the strong full-potential is replaced by a soft pseudo potential which leads to smooth and nodeless wave functions, which still resemble the exact wave functions outside this core region.

- **Augmentation methods**

These methods were first introduced by Slater in 1937 [71]. In this method, the unit cell is partitioned into two regions: one surrounding the atoms (I) and a remaining interstitial region (II) (see Figure 3.1).

In the atomic spheres around the nuclei the movement of the electrons is similar to that in a free atom, while in the interstitial region, electrons move freely and plane waves can be used for their description. For decreasing computational time, it is beneficial to choose the atomic spheres as large as possible but without overlapping them.

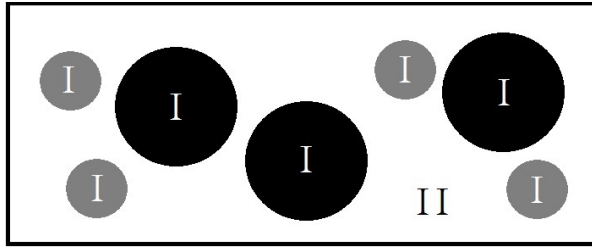


Figure 3.1: Partition of a unit cell in the augmented plane wave method, where two different types of atoms (black and grey) are included.

In this work, first principle calculations were carried out using the full-potential linearized augmented plane-wave approximation (FLAPW) as implemented into the WIEN2k program package [47] [72]. In this package, one can choose between different approximations for the exchange-correlation functional.

3.1.2 WIEN2k code

An appropriate choice of input parameters for calculations based on density functional theory is very important to optimize the results in terms of time and accuracy. The input parameters in ascending order which are needed to run a simulation using the WIEN2k code are presented in Figure 3.2.

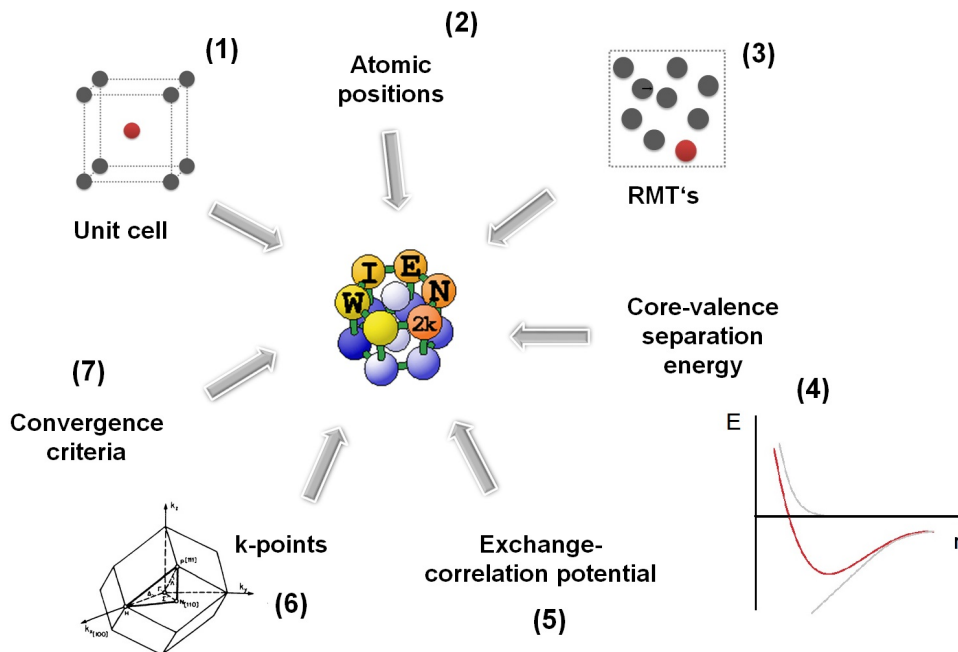


Figure 3.2: Input parameters for *ab initio* calculations using WIEN2k.

Unit cell parameters such as space group, lattice parameters (lengths and angles) as well as atomic positions are provided in the case.struct file. This file can be manually created within the w2web graphical user interface or using a case.cif file from databases or experiments.

During initialization of the calculation, other input parameters have to be specified. In our cases, spin polarization was chosen for all the calculations. At the beginning, the number of k-points and the value of RKmax were varied to find appropriate convergence for the calculations.

3.1.3 Preliminary studies

Lithium cobalt oxide (LCO)

Due to their similarity in terms of structure and to reduce the number of atoms at the beginning, the first simplified model consisted of three atoms, where only cobalt was included as transition metal. This model was used to estimate appropriate input parameters and evaluate differences between the approximation methods for the exchange-correlation potential.

Optimized crystallographic data of this initial model in hexagonal lattice parameters are presented in Table 3.1.

Table 3.1: Crystallographic parameters of LCO.

Parameter	Value
Crystal system	Rhomboedral
Space group	R -3 m
a (Å)	2.833398
c (Å)	14.09250
α (°)	90.00000
γ (°)	120.00000

In addition to the unit cell parameters, also atomic positions and RMT values for partitioning of the unit cell are necessary inputs. These data are presented in Table 3.2.

Table 3.2: Fractional atomic coordinates in rhombohedral setting and RMT values for LCO.

Atom	x	y	z	RMT [bohr]
Li	0.000000	0.000000	0.000000	1.78
O	0.239815	0.239815	0.239815	1.68
Co	0.500000	0.500000	0.500000	1.95

The LCO structure has 12 symmetry operations; all states below -6.0 Ry are treated as non-interacting core states, the plane wave cut-off parameter RKmax was set to 7.0 and 10000 k-points were chosen as initial input parameters. Volume optimization was performed for LCO, to determine the optimum volume and use the resulting structural parameters as a starting point for further NMC calculations. It showed that the theoretical equilibrium volume is 20% increased. Unfortunately, such an overestimation of the theoretical equilibrium volume is quite common when the PBE-GGA is used [73].

The nominal voltage was calculated via the Nernst equation [74]

$$V = -\frac{\mu_{Li}^c - \mu_{Li}^a}{z \cdot F} \quad (3.4)$$

where lithium metal was used as anodic potential (represented by μ_{Li}^a), while μ_{Li}^c was obtained by the variation of the Gibbs free energy of the intercalated and deintercalated structures; represented by their total energies:

$$\mu_{Li}^c = \frac{\delta G}{\delta x} = \frac{\Delta E}{\Delta x} \quad (3.5)$$

When electron volts are used, the Faraday's constant remains one, which is also the number of electrons passing through the outer circuit during charging/discharging [48].

Table 3.3 presents the calculated total energies and calculated voltage per unit cell in Rydberg for discharged, intercalated (LCO) and charged, deintercalated (CO) lithium cobalt oxide using different methods of approximation for the exchange-correlation potential (V_{xc}).

Table 3.3: Comparison of different approximation methods for the exchange-correlation functional of intercalated and fully deintercalated LCO structures.

V_{xc}	LCO [Ry]	CO [Ry]	Voltage [V]
LSDA	-3096.5263	-3081.4280	3.78
WC-GGA [75]	-3101.8354	-3086.6032	3.53
PBEsol-GGA [76]	-3099.6427	-3084.4626	3.54
PBE-GGA [77]	-3103.1667	-3087.8734	3.39

LCO, being the first commercialized cathode material for Li-ion batteries, is well-studied via both; experimental and theoretical work (e.g. [78]). According to other published DFT calculations using VASP and the LDA approximation [79], a theoretical average voltage of 3.75 V was observed for this material [80], which is in good agreement with the data presented here.

The local spin density approximation (LSDA) gives surprisingly accurate results for transition metal oxides and their corresponding properties. This can be explained to some extent by error cancellation of exchange and correlation effects as well as the fact that it fulfills known exact constraints (e.g. exchange-correlation holes) [81].

The optimized structure was further used for calculation of simple NMC super structures, where minimal super cells of 3x1x1 and 3x1x3 were created (see 3.1.3).

Body-centered cubic lithium (bcc Li)

A model of lithium metal in the bcc structure was additionally set-up and used for all further calculations of nominal voltages, where the RKmax value was changed accordingly for consistency within the calculations. The input data of lithium metal is presented in Table 3.4

Table 3.5 presents the calculated total energies per unit cell in Rydberg for body-centered cubic lithium using different methods of approximation for the exchange-correlation potential (V_{xc}).

The body-centered cubic lithium model was used for voltage calculations for LCO (as already presented) and NMC (following section).

Table 3.4: Model input parameters of lithium metal.

Parameter	Value
Crystal system	Cubic
Space group	Im -3 m
a (Å)	3.426666
α (°)	90.00000
Atom	Li
x	0.00000
y	0.00000
z	0.00000
RMT [bohr]	1.78

Table 3.5: Comparison of different approximation methods for the exchange-correlation potential of bcc Li.

V_{xc}	Total energy [Ry]
LSDA	-14.82046
WC-GGA [75]	-14.97254
PBEsol-GGA [76]	-14.92017
PBE-GGA [77]	-15.04406

Simple super structures of lithium nickel manganese cobalt oxide (NMC)

The primitive rhombohedral LCO cell contains 4 atoms, which forms the basis for the conventional hexagonal NMC cell (1x1x3, 12 atoms) and a conventional NMC cell containing 36 atoms (3x1x3). The symmetry was broken and 2/3 of the Co were replaced by Ni and Mn atoms, respectively. These two different NMC unit cells are hereby referred to as "simple super structures" and represent different extrema regarding the arrangement of the transition metals.

In version 1 (V1), the primitive cell of NMC, the transition metals are distributed over the c-direction, which results in alternating layers of NiO₆, MnO₆ and CoO₆ octahedra.

In the conventional cell, version 2 (V2), the transition metals are distributed alternating within these layers (see Figure 3.3).

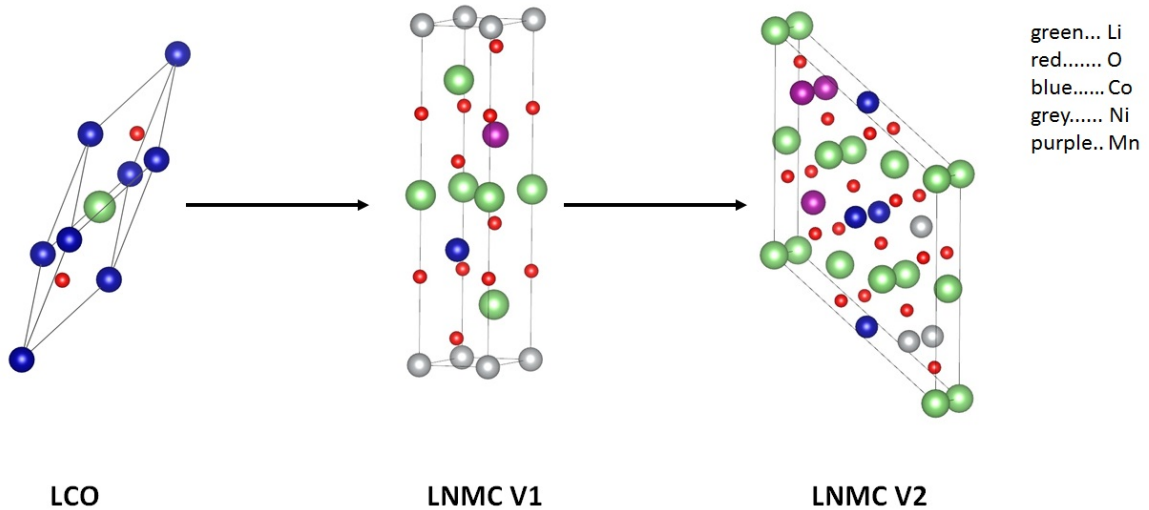


Figure 3.3: Initial minimal models of $\text{LiNi}_{1/3}\text{Mn}_{1/3}\text{Co}_{1/3}\text{O}_2$ based on LiCoO_2 .

Both super structure versions were calculated and compared, whereas the presented total energies refer to 12 atoms. Input parameter were optimized with respect to convergence for the structure version resulting in the lowest energy per primitive unit cell. The volume was varied in 5% steps between -10% and 10% with constant a:b:c ratio, the numbers of k-points was varied between 1 and 10000 and RKmax was varied between 3 and 9. For each parameter, the calculations were performed and the total energy was determined. If the total energy difference between the calculations was below 0.015%, the input parameter was fixed. This way, the most suitable set of RKmax and k-points was established.

Table 3.6 compares the total energies of both versions (V1 and V2) with and without lithium incorporated into the structure (LNMC and NMC) using different approximations for the exchange-correlation functional (E_{xc}) for 10000 k-points and $\text{RKmax} = 7$.

Table 3.6: Total energy in Rydberg of the intercalated and deintercalated NMC structures.

E_{xc}	LNMC V1	NMC V1	LNMC V2	NMC V2
LSDA	-9074.8309	-9029.5729	-9074.7237	-9029.4354
WC-GGA	-9090.5601	-9044.9253	-9090.4929	-9044.8345
PBEsol-GGA	-9084.0739	-9038.6018	-9084.0032	-9038.5087
PBE-GGA	-9094.5281	-9048.7148	-9094.4980	-9048.6731

These results showed that the V1 version possesses the lowest total energy, disregarding the used exchange-correlation method. Still, the differences between V1 and V2 do vary for different V_{XC} .

The largest difference between the two versions was observed for LSDA, where > 0.1 Ry in their total energy was calculated for both, the lithiated (LNMC) and fully delithiated (NMC) structure. Meanwhile, when PBE-GGA was used for the calculations, the difference between the calculated total energies of V1 and V2 for charged and discharged case was < 0.05 Ry.

Taking into account the huge difference in terms of transition metal distribution - where version 1 (V1) is built from mono transition metal oxide layers, while in version 2 (V2), the transition metals are alternately distributed within each layer - the differences are quite small in absolute values between the two versions.

Table 3.7 presents the thus calculated nominal voltages of the super structures of NMC compared to previous work.

Table 3.7: Theoretical nominal voltages of NMC.

V_{xc}	Voltage V1	Voltage V2	Previous work
LSDA	3.615 V	3.751 V	3.745 V [61]
WC-GGA	3.253 V	3.360 V	–
PBEsol-GGA	3.227 V	3.330 V	–
PBE-GGA	3.089 V	3.142 V	3.435 V [82]

These values show only small differences, revealing that both calculated simple super structures have strong similarities in terms of stability and electrochemical performance. The experimentally obtained average voltage of NMC cathodes in half cell configuration against Li/Li^+ was 3.8 V (see electrochemical section 6). The LSDA method again gives results which are closest to the experimentally derived values. The lowest voltage values were obtained for PBE-GGA.

No clear evidence of transition metal ordering was observed from the results of the presented calculations. This supports the assumption that the transition metals are randomly distributed over the layers, which asks for large-size super cell configuration for clarification of possibly neighbouring effects.

Input parameter determination

The determination of appropriate input parameters (RKmax and number of k-points) for the NMC super cell model was performed for version 1 of the simple super structures, as it exhibits the lower total energy compared to version 2.

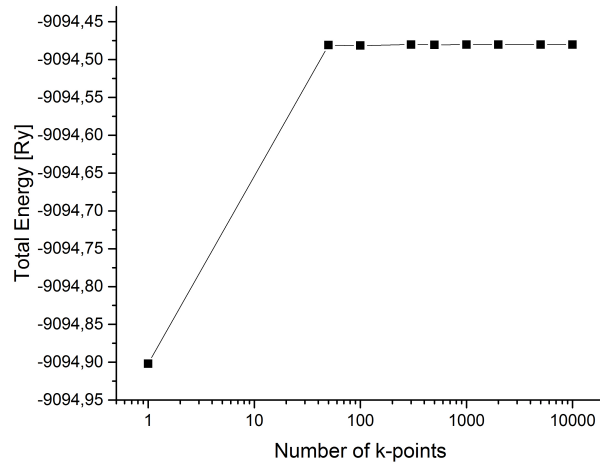


Figure 3.4: Total energy of NMC V1 with respect to the number of k-points.

Figure 3.4 and Figure 3.5 present the results of the input parameter determination.

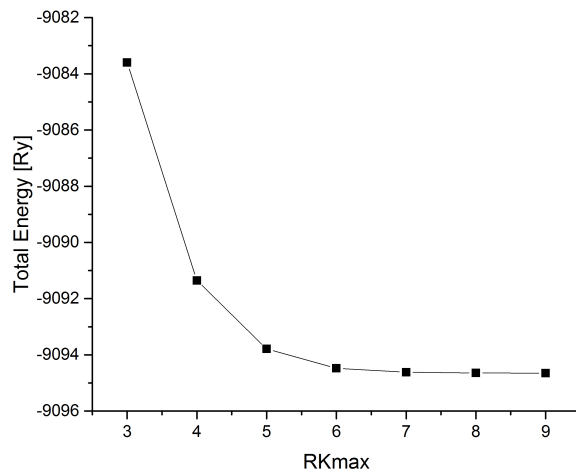


Figure 3.5: Total energy of NMC V1 with respect to RKmax.

For determination of the optimum number of k-points, RKmax was initially set to 6. After the calculation, the number of k-points was fixed to 300, which seemed the optimum value. Thenafter, RKmax was varied for 300 k-points and reasonable convergence was reached using $RKmax = 6$ (see Figure 3.5), which was used in all further calculations. The number of k-points for calculation of the super cell structures was reduced accordingly, due to the increase of the unit cell size.

Volume optimization was performed using the PBE-GGA functional, accordingly as described in the previous section. It was found that the LNMC V1 already had the optimum volume (minimum at 0% volume change) and was therefore not changed for super cell creation.

3.1.4 Li-NMC Supercell

A NMC super cell was constructed from the optimized model V1 as described above. Therefore, the V1 model was multiplied 3x3x1 (axbxc) using the unit cell parameters as shown in Table 3.8.

Table 3.8: Initial unit cell parameters of NMC supercell.

Parameter	Value
Crystal system	Hexagonal
Space group	R -3 m
a (Å)	16.7486
c (Å)	27.7789
α (°)	90.00000
γ (°)	120.0000
RMT (Li)	1.71 bohr
RMT (TM)	1.80 bohr
RMT (O)	1.60 bohr

The 27 transition metal (TM) sites were randomly occupied by Ni, Mn and Co, resulting in a final model of 108 atoms without inversion symmetry. This model was calculated and optimized regarding the atomic positions.

Optimization of the atomic positions at different states of lithiation

Four super cell models, representing four different levels of lithiation (or charge in terms of the cathode), including the full lithiated structure, were set up. In the fully lithiated case, the NMC super cell contains 27 lithium ions. The distribution of the transition metals within the layers was kept constant (see Figure 3.6). These calculated structures are valid for both cases, charging and discharging; for illustrative reasons only the charging case is presented here.

Table 3.9 summarizes the different states of lithiation and corresponding experimental voltages as well as number of lithium ions incorporated into the host structure.

Table 3.9: Calculated super cell models and corresponding states of lithiation for x in $\text{Li}_{1-x}\text{Ni}_{1/3}\text{Mn}_{1/3}\text{Co}_{1/3}\text{O}_2$.

x	No. Li	exp. Voltage
0.00	27	3-3.5 V
0.07	25	3.73 V
0.37	17	3.90 V
0.63	5	4.38 V

It must be pointed out here that the measured voltage values for the same lithiation state might differ between real NMC cathodes, due to variation in their real specific capacities. Additionally, the displayed values refer to a real half-cell measurement against Li/Li^+ when current is applied and not the current-less open-circuit voltages (OCV). The OCV curve for a specific cathode is obtained via applying a current pulse, followed by long relaxation time until the voltage stabilizes (also known as galvanostatic intermittent titration technique - GITT, see electrochemical section 6).

Partial density of states for lithium, oxygen and the transition metals for the optimized structures were plotted using the tetrahedron method as implemented into the WIEN2k package. The partial and total density of states for each element were obtained via summation of the DOS of the corresponding non-equivalent atoms using a spreadsheet.

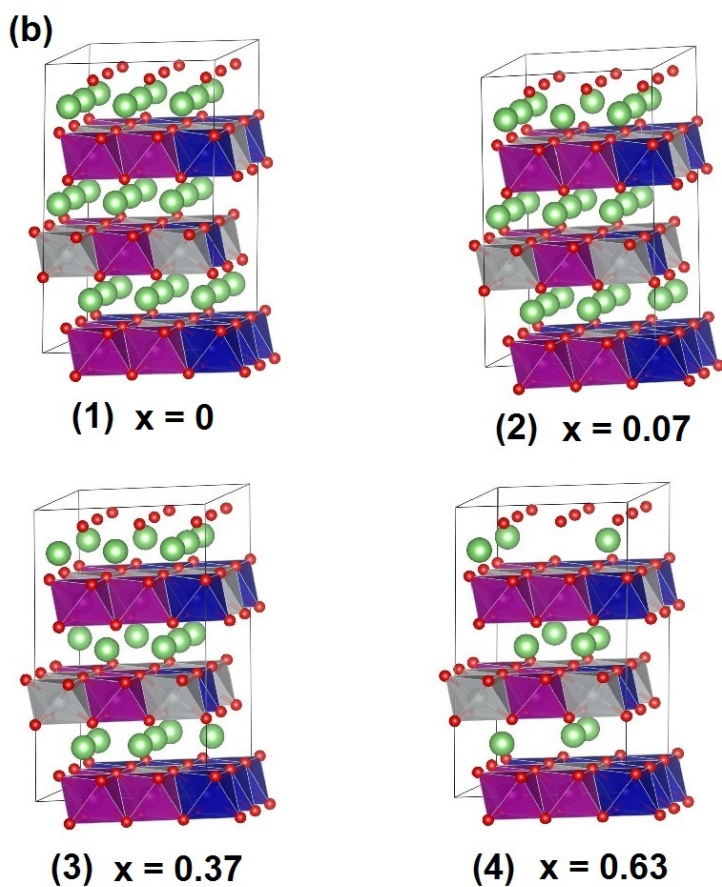
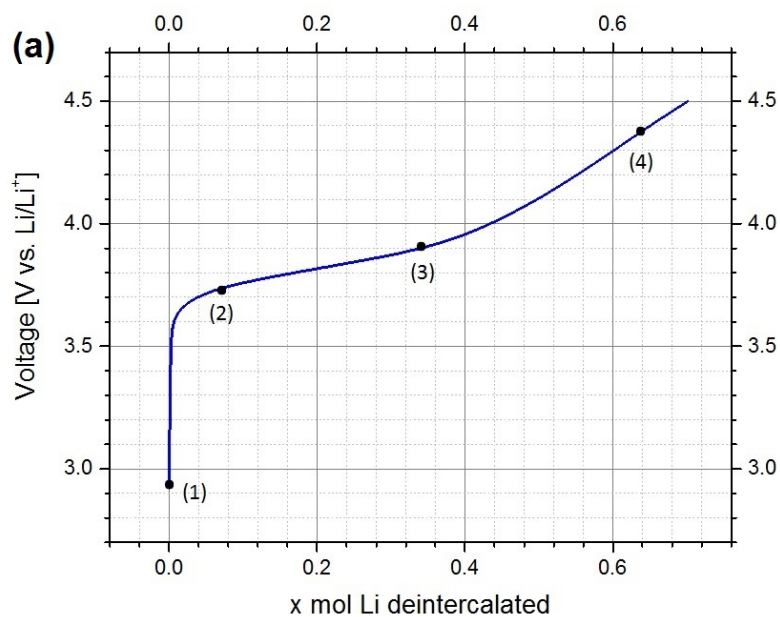


Figure 3.6: Initial super cell models and corresponding state of lithiation at various points during charging. (a) Experimentally derived NMC charging curve and selected points for electronic structure calculations (b) Initial models before optimization and their lithium content for x in $\text{Li}_{1-x}\text{Ni}_{1/3}\text{Mn}_{1/3}\text{Co}_{1/3}\text{O}_2$ (1) - fully lithiated, 27 lithium ions (2) - 25 lithium ions (3) 17 lithium ions (4) 5 lithium ions.

3.2 Results and Discussion

3.2.1 Super cell structures at different states of lithiation

All four super cell structures were fully relaxed and optimized regarding their atomic positions, volume and c/a -ratio. As the smallest unit cell of NMC crystallizes in hexagonal lattice, a and b parameter values were constrained to each other.

Results presented in this section correspond to their particular optimized final super cell structure. The final atomic positions of the optimized structures are enclosed in the appendix (see 7.2).

Unit cell parameter variation

The optimized unit cell parameters for one formula unit are presented in Figure 3.7 for all calculated NMC super cell structures containing different amounts of lithium.

The a -axis represents the intraslab distance between the transition metal oxides, while the c -axis represents the interslab distance between these layers, where lithium ions are intercalated and deintercalated.

A general decreasing trend for the a -axis while charging (decreasing lithium content) was observed. Still, at $x = 0.07$, the a -axis first strongly increases, followed by strong decrease. In contrast, the c -axis shows an increasing trend, having a local maximum at $x = 0.07$. In absolute values, the a -axis varies around 0.01 \AA , while the c -axis variation with lithiation is about an order of magnitude larger (about 0.1 \AA).

Moreover, the c/a -ratio is nearly constant over the calculated range, while strongly increasing at $x = 0.37$. This can be a hint for structural rearrangement and instability at this state of lithiation, as the commercially applied upper cut-off voltage is 4.2 V , corresponding to higher amounts of lithium in the NMC cathode material. This will be proven in the following sections.

The unit cell volume is mainly dominated by the c -axis, first increasing, followed by a strong decreasing trend, having a minimum at $x = 0.37$ and slightly increasing again up to charged state (corresponding to 4.3 V).

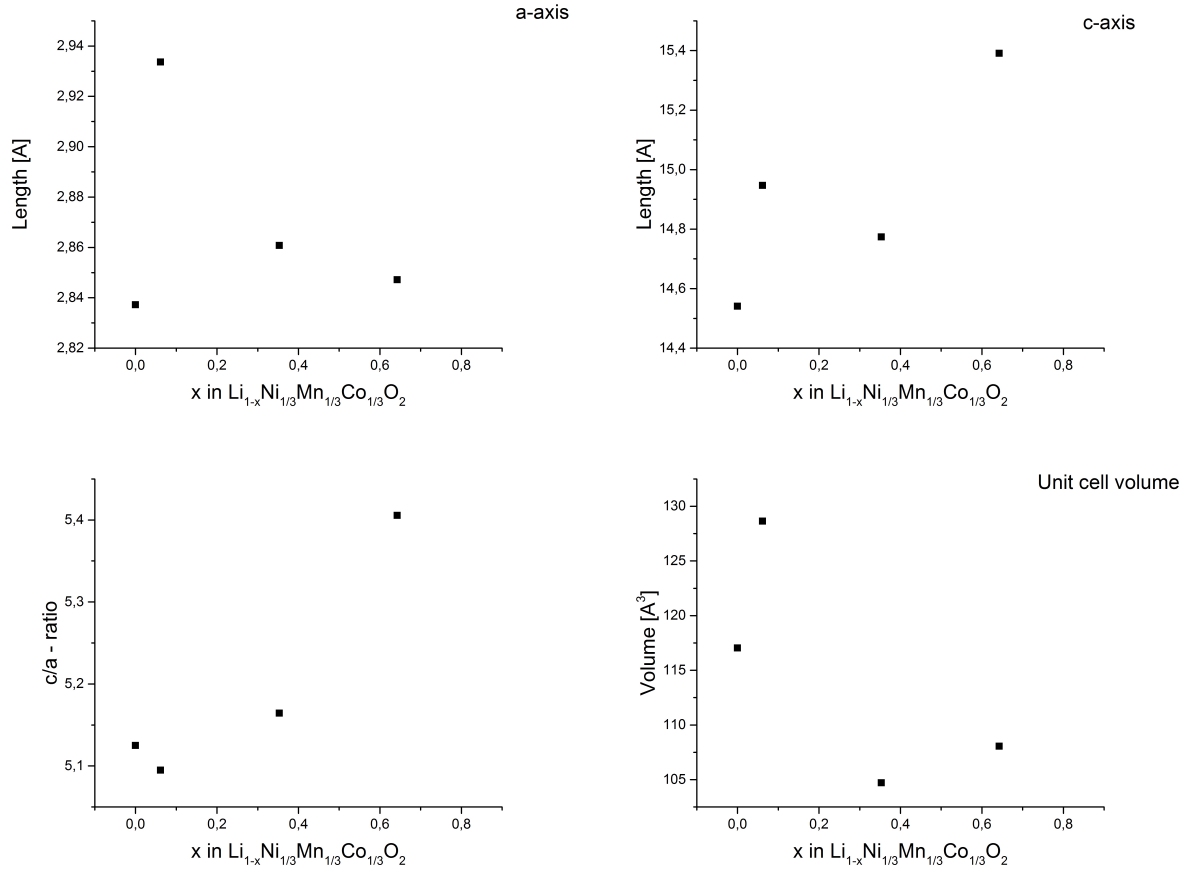


Figure 3.7: Calculated unit cell parameters trend during charging/discharging.

The observed trend showed reasonable behaviour. The increasing interslab distance with decreasing lithium content is explained well by electrical repulsion between the transition metal oxide layers; which is caused by deintercalation of lithium ions between them [29].

The decreasing intraslab distance with decreasing lithium content is linked to the ionic radii variation with oxidation state. The corresponding cation ionic radii are decreasing with increasing oxidation state, which correlates with electron loss for charge compensation during charging.

Obviously, the effect of electric repulsion between the transition metal oxide layers influences the unit cell parameters more than the oxidation state variation. Some irregularity was observed at $> 90\%$ of lithiation ($x = 0.07$) for the unit cell parameters.

All calculated optimized structures are displayed in Figure 3.8 using VESTA [83]. Depending on their lithiation state, their final optimized atomic positions (see 7.2) differed from the original ones.

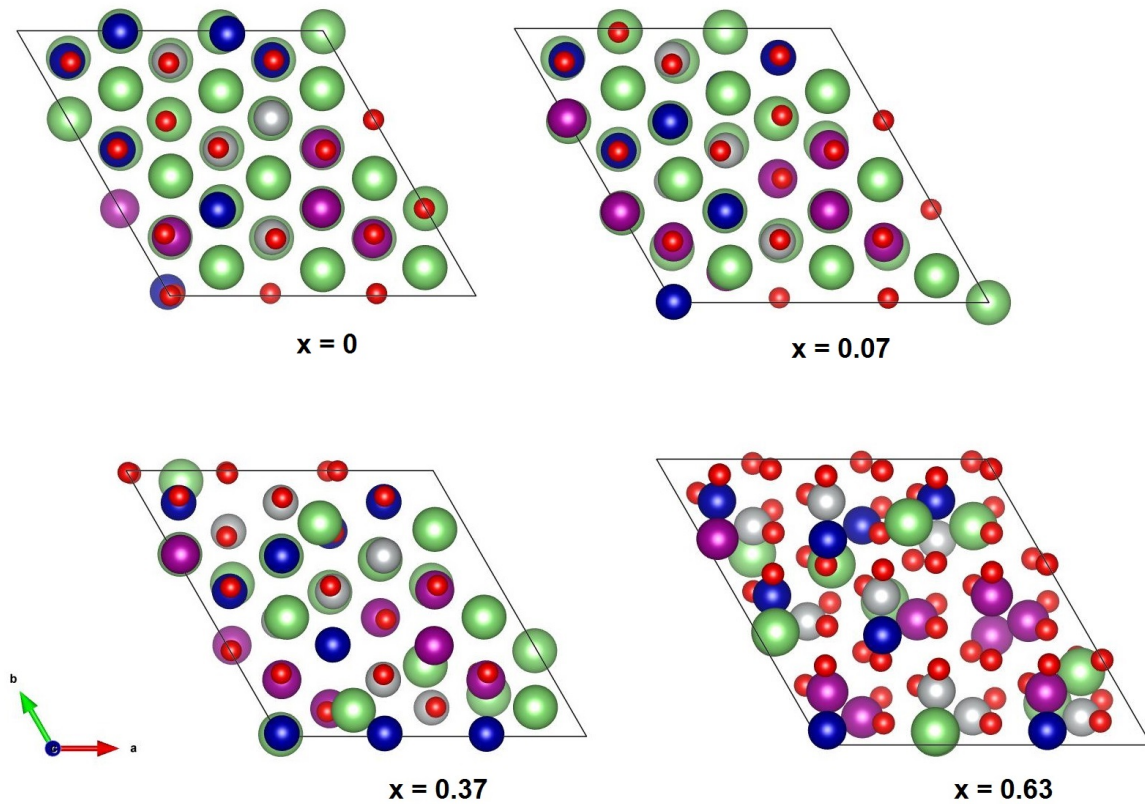


Figure 3.8: Optimized structural models at different states of lithiation for x in $\text{Li}_{1-x}\text{Ni}_{1/3}\text{Mn}_{1/3}\text{Co}_{1/3}\text{O}_2$.

It is shown how the deintercalation of lithium, as calculated, significantly affects the position of the surrounding transition metals. At first ($x = 0$), the atomic positions differ only slightly from their original ones. The observed differences arise from the random distribution of the transition metal ions in the layers.

With increasing delithiation (charging of the battery, $x = 0.07$); the positions start moving, where bigger differences to their initial atomic positions are observed at the positions next to those where lithium ions have been removed. Further removal of lithium ($x = 0.37$) from the host matrix leads to increasing structural disorder. At $x = 0.63$, corresponding to > 4.3 V, which is above the commercially applied upper cut-off voltage, the structure rearranges into another fairly well-ordered form.

The triangle-shape structural arrangement of the transition metal oxides can be associated with spinel structure formation, as experimentally observed at higher cut-off voltages for the familiar layered oxide cathode material Li_2MnO_3 by Shimoda et al. [84]. The formation of this new phase in the structure is irreversible and leads to continuous capacity loss during cycling at higher cut-off voltages.

Table 3.10 summarizes the calculated optimum lattice parameters as well as the average bond length distance between the transition metals and oxygen ions for all optimized super cell structures at different states of charge.

Table 3.10: Calculated structural data of optimized super cell structures.

No. of Li^+	a [\AA]	b [\AA]	c [\AA]	Volume [\AA^3]	TM-O [\AA]
27	2.837	2.837	14.507	101.368	1.969
25	2.934	2.934	14.947	111.393	1.972
17	2.861	2.861	14.774	104.709	1.927
10	2.847	2.847	15.391	108.051	1.912

For average bond length distance, there is a general decreasing trend with decreasing lithium content, even though at removal of the first two lithium ions, the distance is slightly increasing. The irregularity at $> 90\%$ lithiation was also observed by the unit cell parameter variation. The particular values for each transition metal are presented in the following section.

Bond lengths

Calculated bond length distances between the transition metal and oxygen ions (TM-O) at different states of charge (lithium content) are presented in Figure 3.9.

Mn-O bonds show the lowest variation compared to the other two transition metals, indicating no or only small changes in their oxidation states as we will also see later in DOS and magnetic moment variation. Meanwhile, the average bond lengths for Ni-O and Co-O are both decreasing with decreasing Li content, showing highest variation between 0.6 and 0.9 moles of Li in their structure.

Comparing those three transition metals, the maximum bond length changes were observed for Ni-O bonds; showing also largest variation for the same lithiation state. As we will see later, this is linked to oxidation state variation for charge compensation.

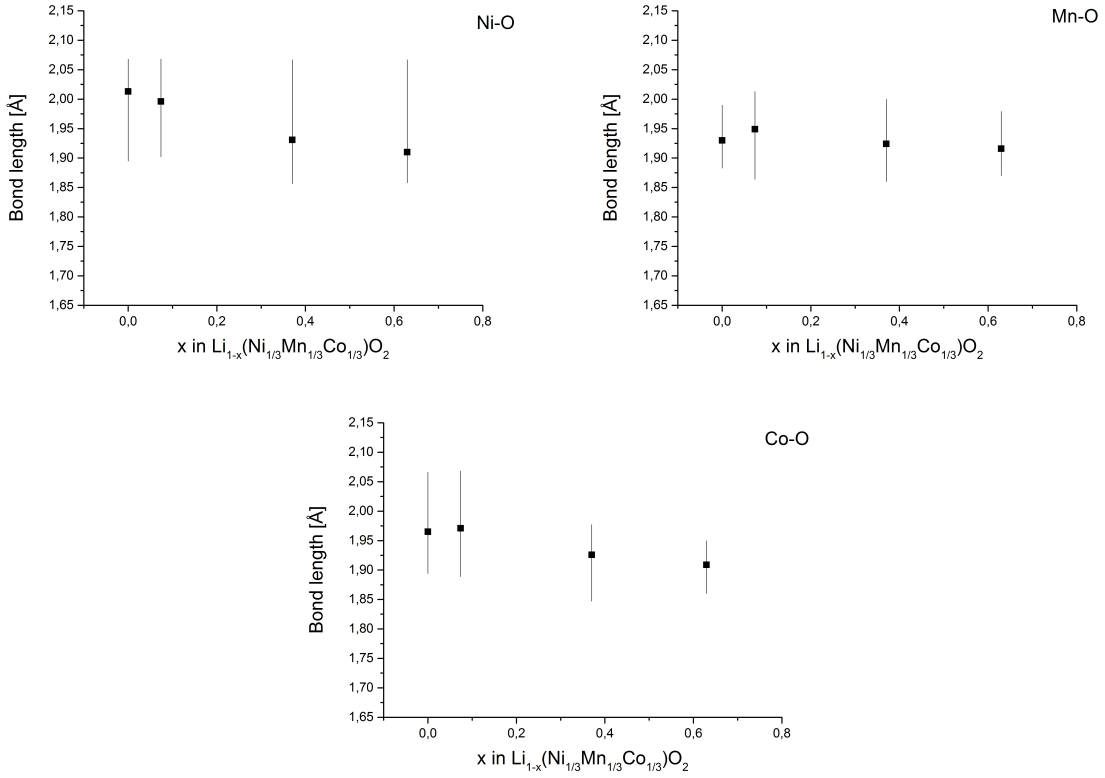


Figure 3.9: Calculated bond lengths changes with lithiation. The squares indicate the mean values while the lines represent the whole range of the bond lengths.

Synchrotron radiation-based spectroscopic studies indicated that at 50% SOC (state-of-charge), which were related to 0.677 moles of Li in NMC cathodes; half of the Ni-ions are in low spin Ni^{3+} configuration, which exhibit Jahn-teller distortion in octahedral arrangements, while others remain in Ni^{2+} state [85]. The observed variation of Ni-O bond lengths in these calculations can confirm this statement.

The overall trend correlates well with the calculated unit cell parameter variation, as the intraslab distance (a -axis) is increasing with increasing lithium content and reflects the oxidation of the transition metals for charge compensation during charging of the battery cell (cathode material).

Combining these results, the nickel and the cobalt bond length contribution to the unit cell parameter variation is higher than those of manganese ions. This statement will be additionally confirmed by the corresponding partial density of states and magnetic moment calculations in the following sections.

Intercalation voltage

The average voltage for different states of lithiation was calculated accordingly from the observed total energies as already described for NMC super structures.

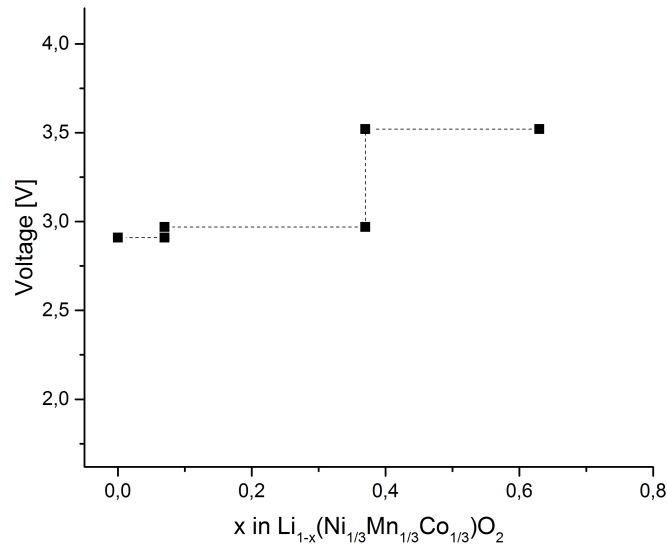


Figure 3.10: Calculated intercalation voltage of the super cell structures of NMC.

Figure 3.10 presents the calculated voltage curve in the specific state-of-charge of the NMC cathode material. The artificial stepwise character of the voltage arises from averaging over the calculated intervals and is smoother in real cell arrangements. Its increasing trend fits well the experimentally observed curve as presented before.

Average voltages are generally underestimated by *ab initio* methods based on GGA [33]. This is caused by electron self-interactions, which lead to errors for strongly correlated electronic systems such as transition metal oxides like NMC cathode materials.

The presented voltages are calculated for fully relaxed states (as in open-circuit case), which are usually not measured during routine cycling, when current is flowing through the battery cell. For charging case, as visualized in the methodology section for super cell setup; the open-circuit voltage (OCV) therefore must be lower than the measured voltage. An example for an experimentally obtained OCV curve of real NMC cathodes can be found in the electrochemical section (see 6.2.1).

Density of states

Li s-states showed low contribution for all calculated structures, and are therefore not shown explicitly. O p-states dominate at energies around 3 eV below the Fermi level (see Figure 3.11). Little variation was observed with state of lithiation for the O p-states. Still, some contribution was observed near E_F , moving upon further delithiation into higher lying, unoccupied states. This indicates some small extend of oxygen contribution to the overall charge compensation. As we will see later, the contribution of Ni and Co still dominates, reflecting the stability of the NMC cathode material.

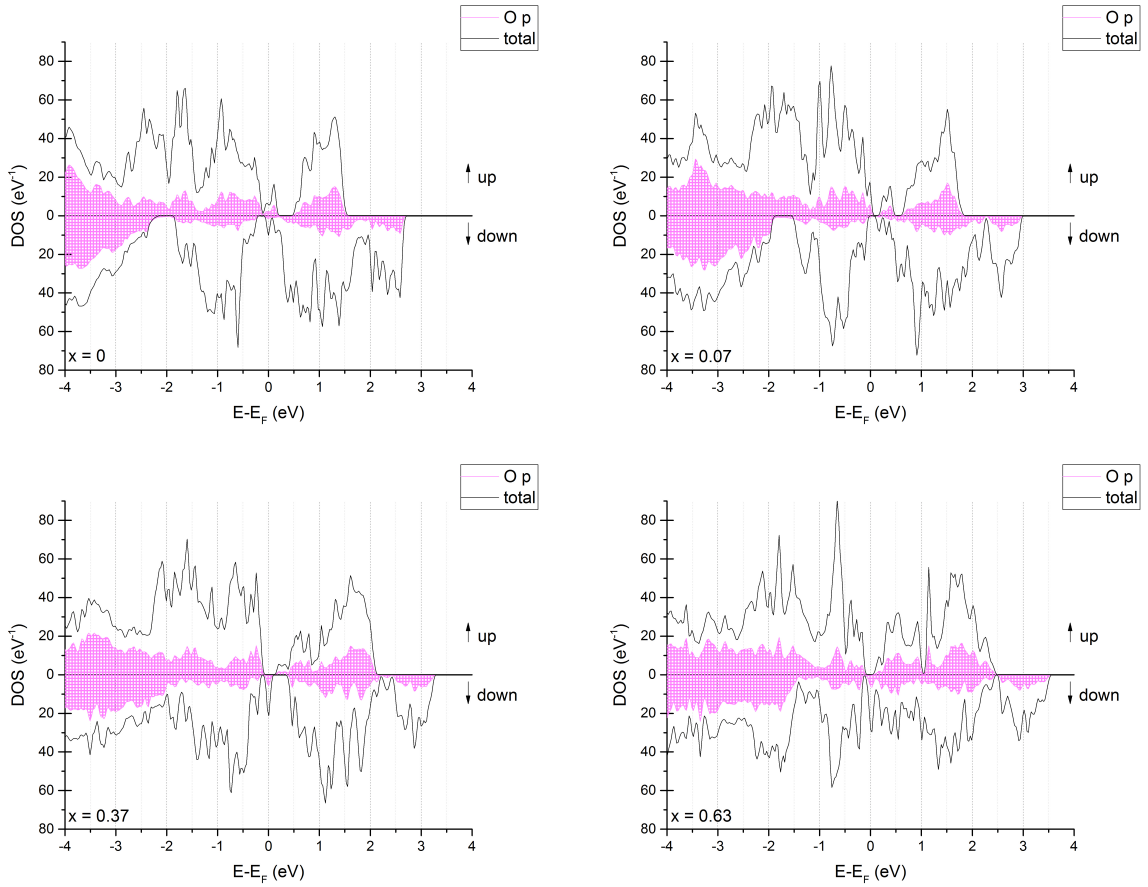


Figure 3.11: O p-states and total density of states for x in $\text{Li}_{1-x}\text{Ni}_{1/3}\text{Mn}_{1/3}\text{Co}_{1/3}\text{O}_2$.

There is a clear connection between partial density of states of oxygen and the stability (and further on safety) of cathode materials. If the filled states nearby the Fermi level are mainly dominated by oxygen; charging can lead to oxygen release and further reaction with the electrolyte and/or phase transition, meaning additional phase formation of the active material [86].

This is well-reflected by the calculated DOS of NMC with decreasing lithium content, showing reasonably stable behaviour. If the density of states at the Fermi level have more oxygen character, (e.g. for LiNiO_2 [87]), the missing charge is subtracted by oxygen, leading to oxygen evolution and consequently capacity losses. Usually, valence change of the transition metals contributes to the overall cell reaction, whereas oxygen should remain close to its preferred O^{2-} state.

Figure 3.12 presents the partial density of states of the transition metal d-states in comparison with the total density of states for fully lithiated state.

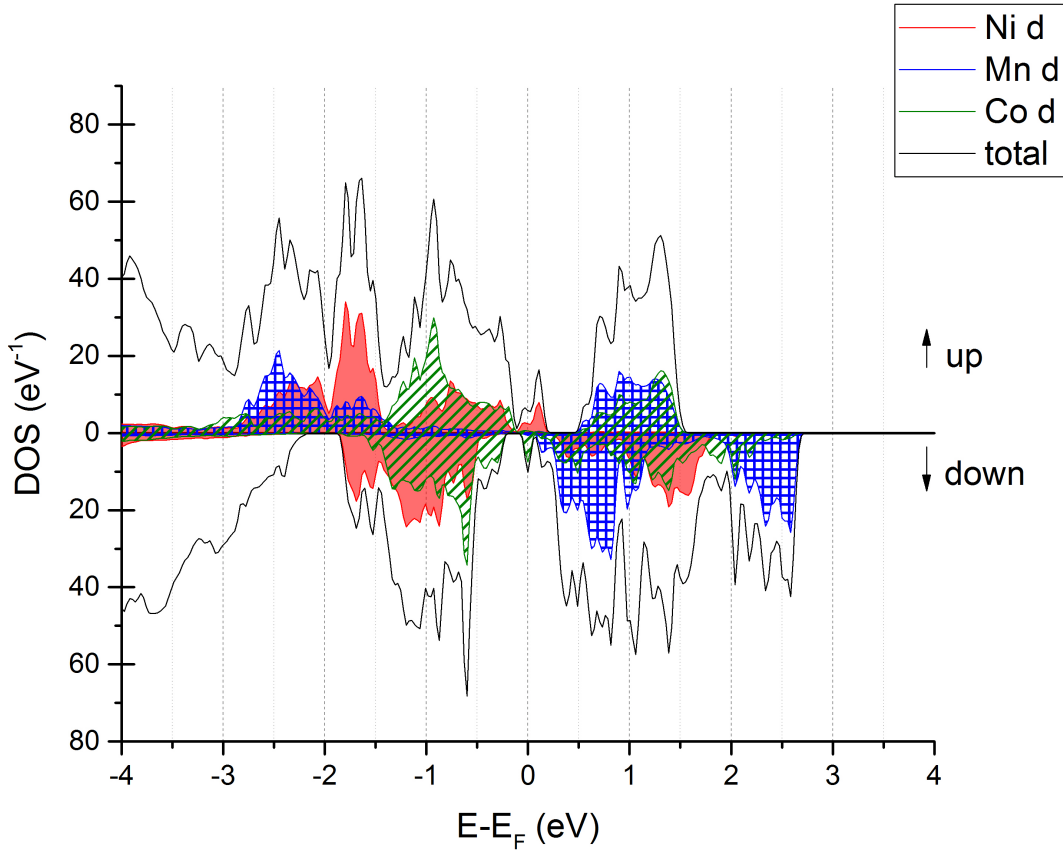


Figure 3.12: Total and partial density of states of the transition metals for $x = 0$ in $\text{Li}_{1-x}\text{Ni}_{1/3}\text{Mn}_{1/3}\text{Co}_{1/3}\text{O}_2$.

The 3d bands of the transition metals are usually split into t_{2g} and e_g bands in octahedral configuration, which was observed for Mn and Co d-states for all calculated structures. Near the Fermi energy, the highest contribution for spin-up was observed for nickel d-states, while cobalt states are dominating for spin-down case. No or little manganese contributions were observed for both cases.

In the fully lithiated NMC structure, in the spin-up case, all t_{2g} states of the transition metals are fully occupied, while in the spin-down case, Mn- t_{2g} states are unoccupied, whereas Ni and Co- t_{2g} states are occupied. For spin-up, Ni- e_g states are occupied while all other e_g states for spin-up and -down are unoccupied. The fully lithiated structure shows metallic character, in contrast to other calculated density of states, which show half-metallic character.

Figure 3.13 presents the calculated density of states after removal of two lithium ions from the host structure.

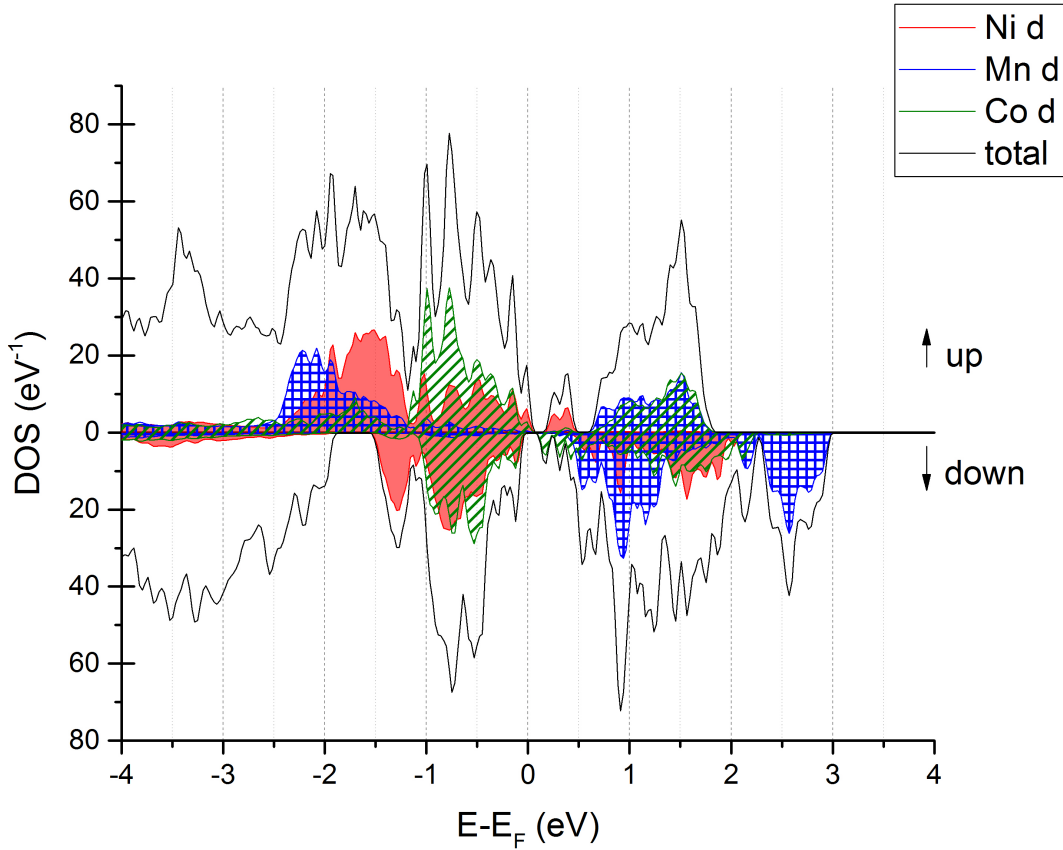


Figure 3.13: Total and partial density of states of the transition metals for $x = 0.07$ in $\text{Li}_{1-x}\text{Ni}_{1/3}\text{Mn}_{1/3}\text{Co}_{1/3}\text{O}_2$.

Still, nickel d-states are the dominant states near the Fermi level, indicating their contribution to the redox process for spin-up case, while spin-down case shows non-metallic character with both, nickel and cobalt contribution in the highest occupied bands.

The split into t_{2g} and e_g bands was not directly observed for Ni d-states, indicating some Ni^{3+} oxidation state, which shows Jahn-Teller distortion. Additionally, as the partial density of d-states were calculated via summation over all nickel ions, the mean values over all oxidation states for one type of transition metal are displayed here. Overall, the t_{2g} and e_g band occupation of the transition metals is similar to the fully lithiated state presented above, showing only slightly shifts towards higher energy levels with respect to the Fermi level.

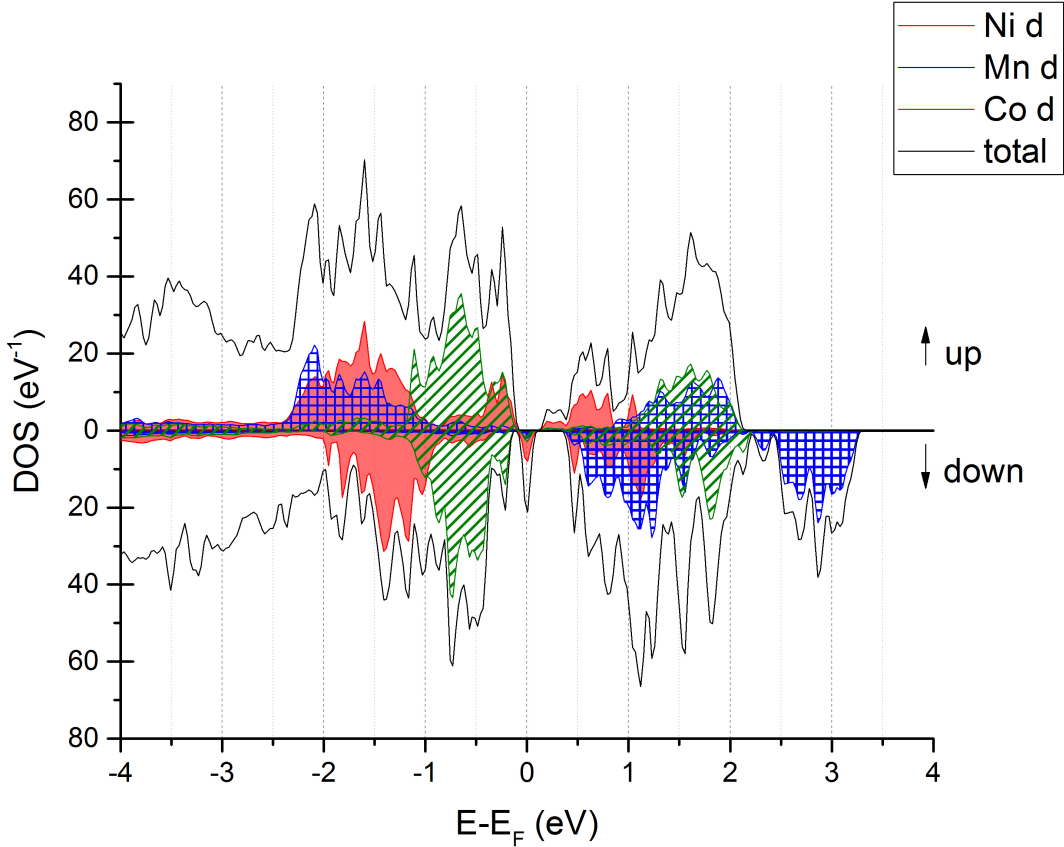


Figure 3.14: Total and partial density of states of the transition metals for $x = 0.37$ in $\text{Li}_{1-x}\text{Ni}_{1/3}\text{Mn}_{1/3}\text{Co}_{1/3}\text{O}_2$.

When delithiation continues and further lithium ions are removed from the host structure (see Figure 3.14), there are much more unoccupied Ni spin down states and the highest occupied bands near the Fermi level are dominated by nickel spin-down d-states, showing increasing contribution of cobalt states. Both, cobalt and nickel states are shifting with delithiation towards higher energies with respect to the Fermi level.

Figure 3.15 shows the density of states above the usually applied upper cut-off voltage of 4.2 V. At this state of delithiation, the states at Fermi energy are dominated by cobalt states for spin-down states, even though some nickel contribution remains. This is in contrast to the DOS calculations presented above, where the total density of states were mainly dominated by nickel states around the Fermi energy.

At this state, the split of the d-states into t_{2g} and e_g -states was observed for all transition metals, including Ni, indicating no Ni^{2+} oxidation state, which is supposed to be further oxidized to Ni^{3+} , as we will see later in the magnetic moments. The t_{2g} -states are fully occupied, indicating low spin configuration. Overall, manganese d-states were moving closer to the Fermi energy, even though they show only a very small contribution to the charge compensation.

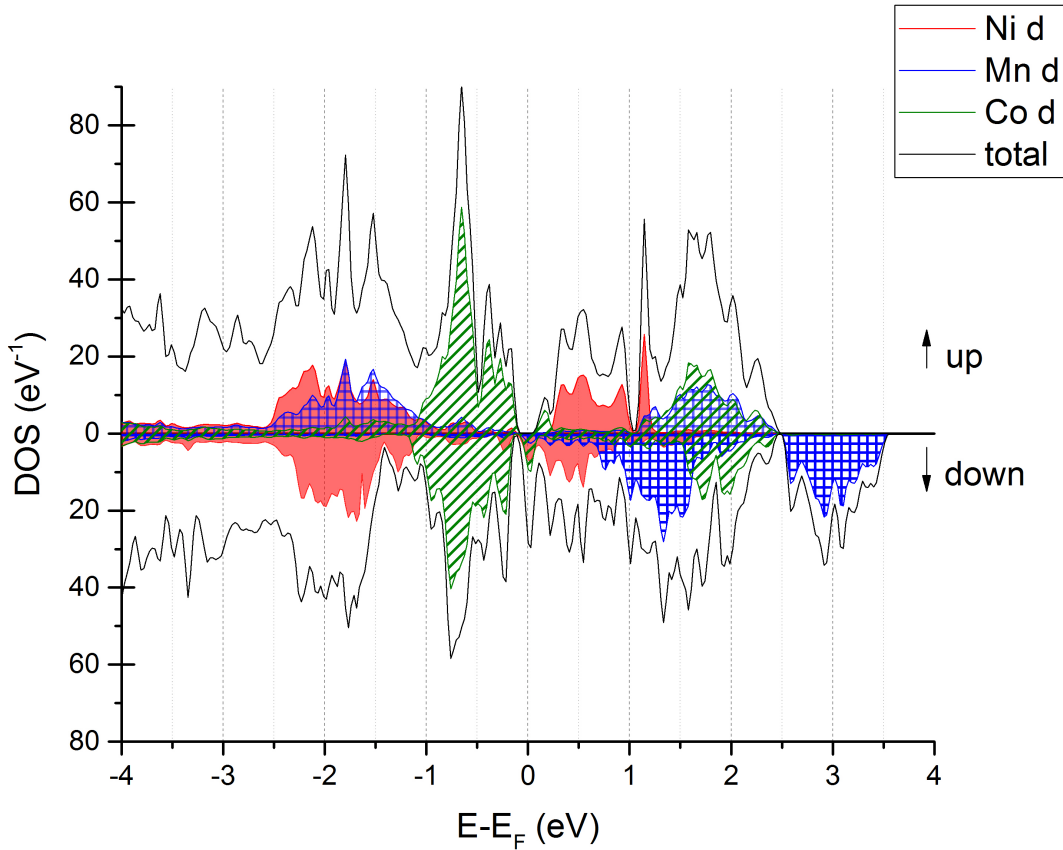


Figure 3.15: Total and partial density of states of the transition metals for $x = 0.63$ in $\text{Li}_{1-x}\text{Ni}_{1/3}\text{Mn}_{1/3}\text{Co}_{1/3}\text{O}_2$.

Magnetic moments

Magnetic moments of the transition metal ions arise from the difference of spin up and spin down d-states and usually characterize best the oxidation state of the transition metal ions. As some differences were observed for particular transition metals of the same type, Figure 3.16 illustrates the correct labels of the corresponding transition metal ions.

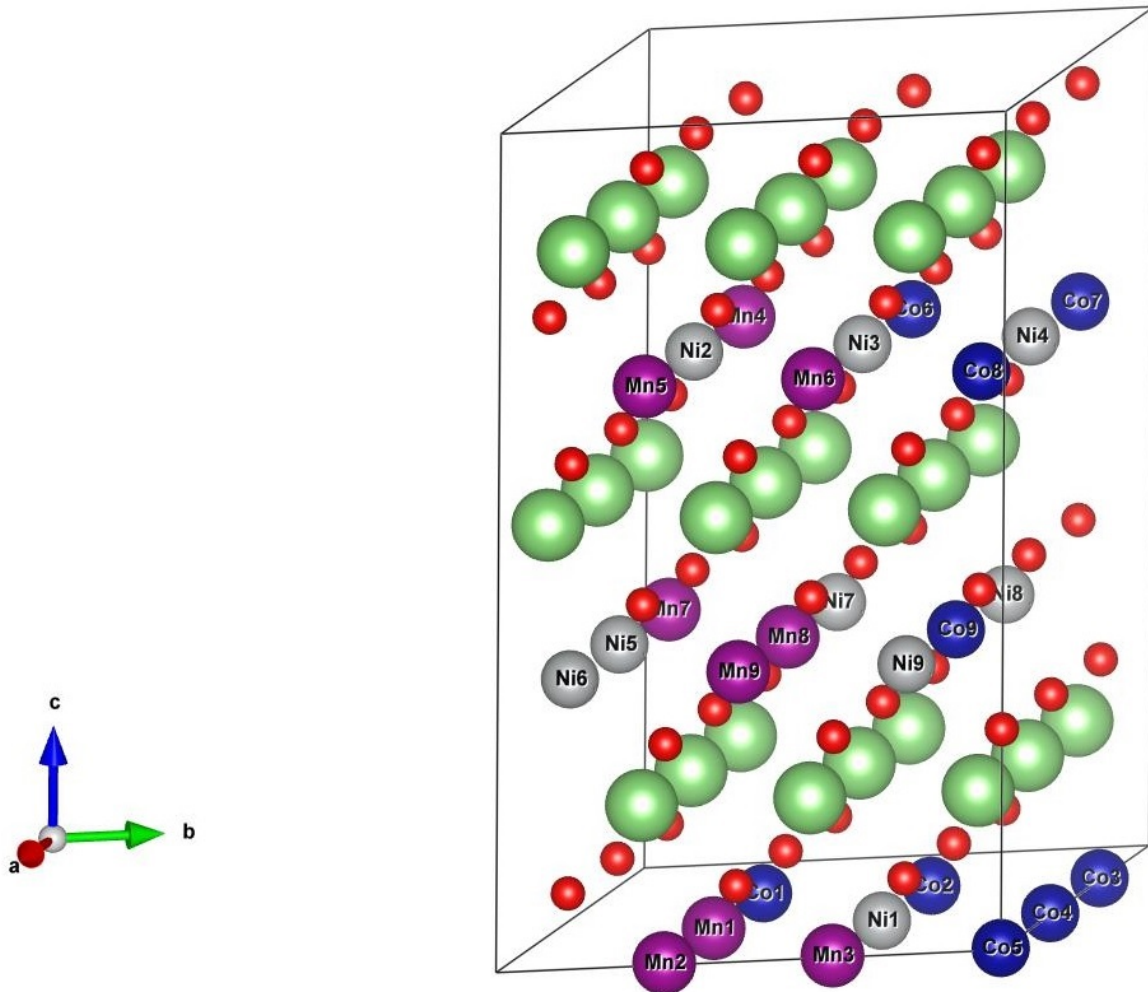


Figure 3.16: Super cell structure including numbering of particular transition metals. Green...Li, Red...O, Blue...Co, Grey...Ni, Purple...Mn.

The spin-only magnetic moments are directly obtained from the output files of the simulations. Figure 3.17 presents the calculated magnetic moments of the transition metal ions at different states of lithiation of the optimized super cell structures.

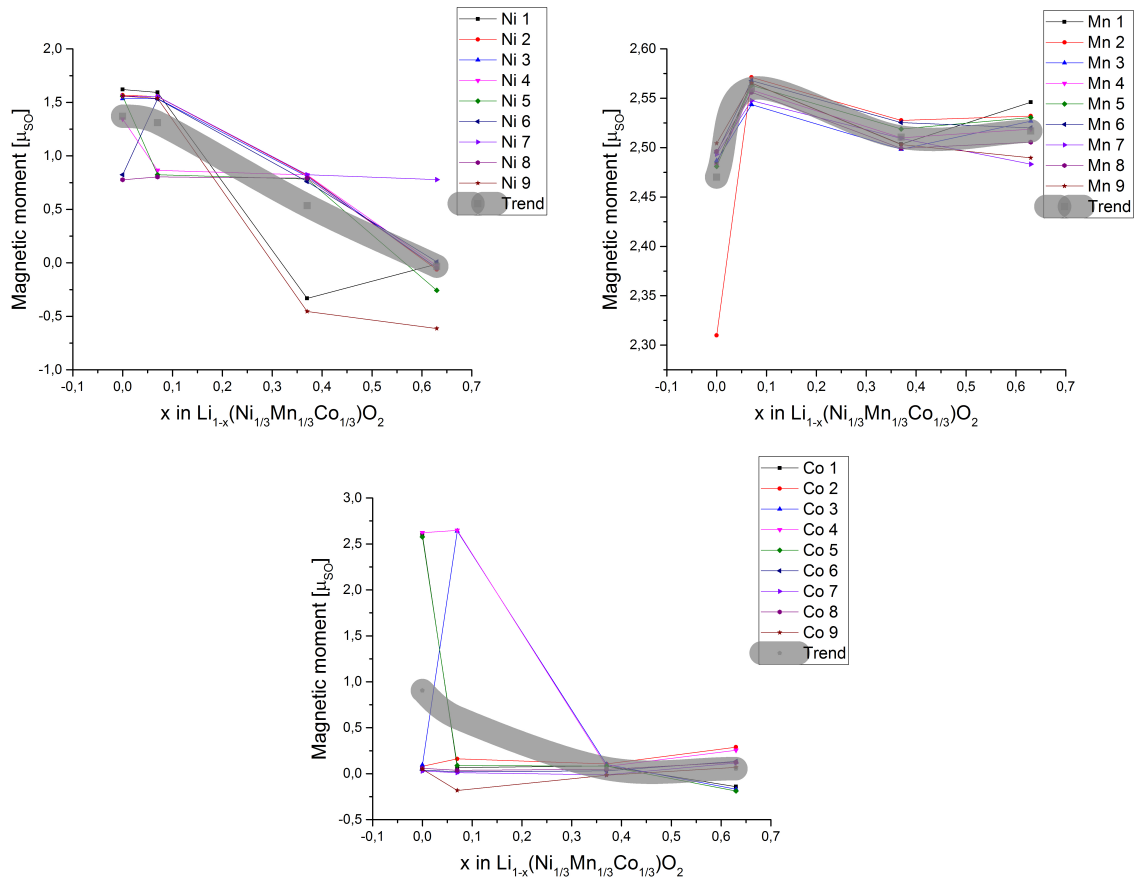


Figure 3.17: Calculated magnetic moments during charging, including mean values in grey.

Highest variation of the magnetic moments was observed for nickel ions. At fully lithiated state, all Ni show magnetic moments, which are decreasing in all cases with delithiation. At the cut-off voltage, $x = 0.63$, all nickel ions show no magnetic moment, except Ni5 and Ni9. In this state, all lithium ions surrounding Ni5 were already deintercalated. Ni9 even shows a negative magnetic moment. This nickel ion, in the calculated structure, is still completely surrounded by lithium ions.

Among all transition metals present in the structure, Ni has the highest contribution to the overall cell reaction for charge compensation. Ni^{2+} has d^8 configuration, having a magnetic moment of $2 \mu_B$. When Li^+ is removed from the structure, the oxidation state is increasing to Ni^{3+} , including decreasing magnetic moment in low spin configuration ($1 e^-$ in e_g , $1 \mu_B$).

Further removal of Li^+ leads to further oxidation to Ni^{4+} , where one e^- is removed from e_g , having no magnetic moment in low spin configuration ($0 \mu_B$). According to DOS calculations, as already presented, low spin configuration is realistic as the spin up and spin down t_{2g} states are fully occupied and show no exchange-splitting, whereas e_g states are unoccupied states above E_F .

Magnetic moments of manganese do not significantly change with lithium contents. At fully lithiated state, only one manganese ion (Mn2) shows different behaviour. This is the only manganese ion which is not surrounded by any nickel ion (neither along a- nor c-axis). When delithiation starts, Mn2 changes its oxidation state and the overall magnetic moments of the manganese ions remain fairly constant. Manganese is supposed to be in Mn^{4+} state, having 3 d-electrons, occupying the t_{2g} states, resulting in $3 \mu_B$.

Cobalt shows very low magnetic moments up to 90% lithiation, where two ions show a magnetic moment for the last two calculated structures. At fully lithiated state, three cobalt ions show magnetic moments: Co1, Co4 and Co5. Co1 and Co5 are the only cobalt ions which are not surrounded by nickel ions; while Co4 is the direct neighbour of Co5 and only surrounded by one nickel ion. Upon further delithiation, when two lithium ions were removed from the structure; still, Co4 shows a magnetic moment while Co5 and Co1 return to zero magnetism. In addition to Co4, Co3 shows a magnetic moment which was not observed in fully lithiated state. This cobalt ion is located next to the deintercalated lithium ion, which removal directly affects its magnetism. Upon further delithiation, all cobalt ions remain in non-magnetic state.

Co^{3+} exhibits 6 d-electrons, which in low spin configuration occupy all t_{2g} states ($0 \mu_B$). Upon removal of Li^+ , the tetravalent state, Co^{4+} , exhibits $1 \mu_B$ due to one unpaired electron, while in high spin configuration the magnetic moment increases to $5 \mu_B$.

Due to some extend of hybridization of O p- and TM d-states, the presented magnetic moments of the transition metals are reduced, resulting in small magnetic moments at oxygen sites and even magnetic moments below zero for low spin Ni^{4+} . The results correlate well with the calculated bond length variation with lithiation state, as well as the DOS and partial DOS of the corresponding transition metals.

3.3 Conclusion

It was shown that first principles calculation of the mixed transition metal oxides provide a great insight and reasonable results regarding corresponding oxidation states of the transition metal ions and structural changes during charging/discharging.

No clear evidence for transition metal ordering in the symmetric NMC cathode material was observed from preliminary studies. Therefore, random distribution of nickel, manganese and cobalt using a high number of atoms (108) in the unit cell was chosen for the electronic structure calculations.

It was shown that above the cut-off voltage of 4.3 V, the crystal structure of NMC rearranges for charge compensation of lithium ion deintercalation. The structural rearrangement can be associated to spinel formation, as observed for familiar layered transition metal oxide cathode materials at higher cut-off voltages [84]. This corresponds to the region, where cobalt density of states dominate the total density of electronic states of the calculated NMC super cell.

Electric repulsion between the mixed transition metal oxide layers when lithium is deintercalated leads to increasing interslab distance with decreasing lithium content. Meanwhile, the intraslab distance decreases due to oxidation of the transition metal ions, also reflected by the decreasing bond length distance between the transition metals and oxygen.

Both, bond length and magnetic moment changes with lithiation indicate that nickel and cobalt contribution to the redox processes for charge compensation during cycling is higher compared to manganese; which is supposed to be inactive and stabilize the structure. The nickel contribution is more pronounced compared to cobalt for all calculated parameters.

The following redox processes during cycling of $\text{Li}_x\text{Ni}_{1/3}\text{Mn}_{1/3}\text{Co}_{1/3}\text{O}_2$ are suggested:

$2/3 \leq x \leq 1$: Nickel oxidation from 2+ to 3+

$1/3 \leq x \leq 2/3$: Nickel oxidation from 3+ to 4+

$0 \leq x \leq 1/3$: Cobalt oxidation from 3+ to 4+

In conclusion, enhancing the nickel content is reasonable for optimization of the symmetric NMC cathode material in terms of stability at higher cut-off voltages, and was therefore experimentally exploited and the results will be presented in the following sections.

4 Syntheses

In order to synthesize the desired product, lithium nickel manganese cobalt oxide, with two different ratios between the transition metals (1:1:1 and 5:3:2), various syntheses were performed and the conditions were varied. Coprecipitation was chosen as the main synthesis route, where two types of precursors were applied: nitrates, which are quite commonly used; and chlorides, due to industrial interest. Additionally, the temperatures in the second oven step were varied and the atmosphere was changed. In total, differences were evaluated in terms of oxygen content, temperature, and type of precursor.

4.1 Coprecipitation method

The overview of the synthesis can be seen in Figure 4.1.

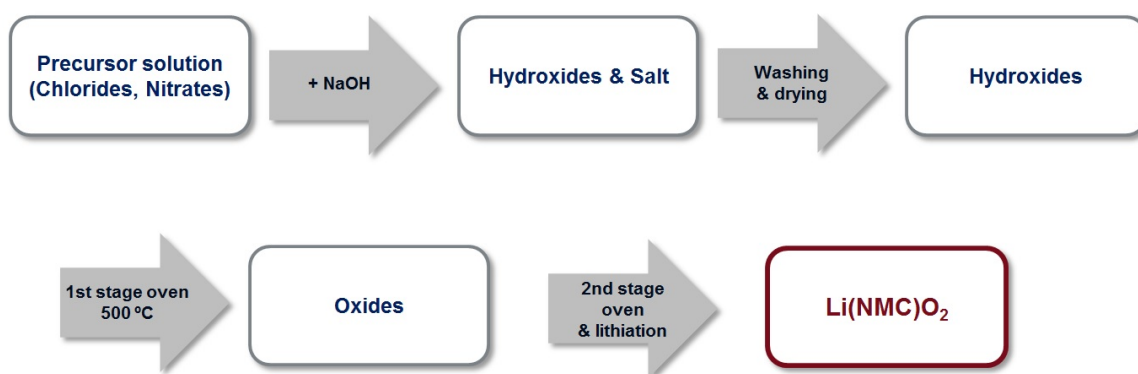


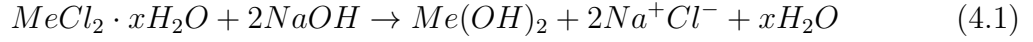
Figure 4.1: Synthesis steps for coprecipitation route to obtain NMC.

The concrete synthesis description is:

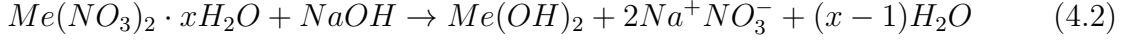
Aqueous solutions (0.2 mol dm^{-3}) of Mn^{2+} , Ni^{2+} and Co^{2+} were prepared from $\text{MnCl}_2 \cdot 4\text{H}_2\text{O}$ (Sigma Aldrich, 98%), $\text{NiCl}_2 \cdot 6\text{H}_2\text{O}$ (Sigma Aldrich, 98%) and CoCl_2 (Sigma Aldrich, 97%) or $\text{Mn}(\text{NO}_3)_2 \cdot 4\text{H}_2\text{O}$ (Merck, 98%), $\text{Ni}(\text{NO}_3)_2 \cdot 6\text{H}_2\text{O}$ (Merck, 99%) and $\text{Co}(\text{NO}_3)_2 \cdot 6\text{H}_2\text{O}$ (Alfa Aesar, 98%), respectively, to give the desired stoichiometry.

The solutions were then mixed and concentrated ammonia was added (6:1 ratio with total cation content). A calculated amount (2:1 ratio with total cation content) of NaOH solution ($2 \text{ mol} \cdot \text{dm}^{-3}$, from pellets by Sigma Aldrich, 98%) was then added dropwise.

The corresponding reaction formula for the precipitation step using chloride precursors is



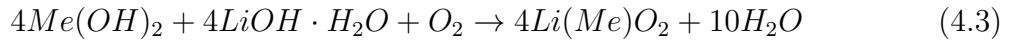
while for nitrate precursors the reaction formula it is



In these reaction formulas the intermediate products - the mixed transition metal hydroxides - are the same and therefore, differences in the final NMC powders of these syntheses are dominated by impurities or not reacted species remaining in the structures.

The resultant precipitate (mixed hydroxides) was then filtered and washed several times with deionized water, until the filtrate reached a pH value of 7.00. The precipitate was dried overnight at 120 °C for water removal. The dried powder was then milled with excessive (3 mol%) LiOH·H₂O (Alfa Aesar, 98%) in a planetary ball mill. The mixture was then heated to 500 °C in a zirconia boat for 5 h. Afterwards, the sample was cooled down, ground in an agate mortar and then placed in a zirconia boat at 800 °C to 950 °C, depending on the NMC, for 10 h. All heating was carried out at a rate of 5 °C min⁻¹, either in a turbe furnace (MTI) under flowing air or in a muffle furnace (Nabertherm) under atmospheric conditions.

The last reaction is oxidation reaction of the mixed hydroxides according to



5 Physico-chemical characterization

Physico-chemical characterization includes surface areas, porosity, microscopic methods and particle size distributions as well as crystal structure determination. The microstructure of electrode materials is very important for commercial applications and has a major influence on their performance and handling. The applied methods are explained and the results presented and discussed with respect to the corresponding synthesis conditions, especially for the unconventional chloride precursor and its influence on the particle and crystallographic characteristics.

5.1 Methods

5.1.1 Gas adsorption measurements

The amount of gas adsorbed at the surface of solid particles is directly related to the specific surface area of the material. Therefore, gas adsorption measurements are a standard method for physico-chemical characterization of powders and solids. To enhance the energy density of electrode active materials, a high specific surface area is favorable. As the surface area is directly related to the effective reaction area of electrodes, this analytical tool is usually applied for electrode active material characterization.

The theory behind these measurements was first introduced by Brunauer, Emmett and Teller [88] (therefore, BET method or BET surface area), and is basically an extension of the formerly known theory of molecular adsorption by Langmuir [89].

The amount of gas molecules adsorbed by a surface is directly connected to their surface area according to

$$S_{spec} = \frac{N_A \cdot A_m \cdot m_{mono}}{m_s \cdot M} \quad (5.1)$$

Here, S_{spec} refers to the specific surface area, N_A to the Avogadro constant, A_m to the area which the adsorbed gas covers at the surface of the sample, m to the masses of the monolayer (*mono*) and sample (*s*), respectively, and M to the molecular weight of the adsorbed gas. The volume of the monolayer and consequently the mass is derived by the linearized BET isotherm from measuring the volume of the adsorbed gas in correlation with the relative pressure (adsorption isothermal curve).

However, not only surface areas, but also pores and their volume and distribution are important for improvement of the porous electrodes as present in Li-ion batteries. The pore size distribution is derived by the subsequent reduction of the partial pressure, where the adsorbed gas is released in correlation to the size of the corresponding pores [90]. The analysis can be performed in a similar way, including the measurement of the desorption isothermal curve (see Figure 5.1). The plateau at the beginning and end of the measurement correlates to the monolayer coverage of the sample with the analysis gas.

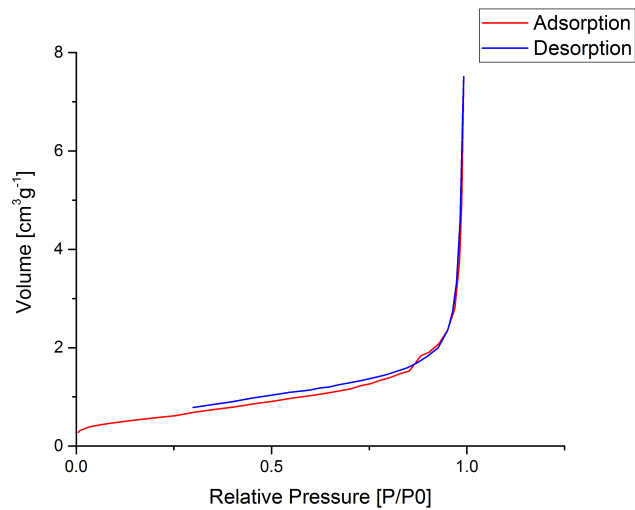


Figure 5.1: Representative adsorption and desorption isothermal curve.

To determine the specific surface area as well as the porosity of the synthesized NMC powders, gas adsorption measurements were performed using a Quantachrome iQ, and the data was analyzed using ASiQwin software. The samples were first dried at 120 °C (heating rate 5 °C min⁻¹) for three hours to remove residual water (outgas process) and then the nitrogen analysis gas adsorption as a function of relative pressure was measured. The specific surface area was determined by the BET-method out of 8 points of the adsorption curve, while the porosity was derived by the desorption curve using 26 points and the BJH-method, both implemented into the software.

5.1.2 Laser diffraction analysis

Particle size distribution is an important physico-chemical characteristic of electrode active materials. The particle size itself influences the reaction area between the electrode and the electrolyte and its distribution affects the hollow space and porosity inside the electrode. Additionally, it is crucial for industrial electrode formulation as for example coating, composition, and pressing of the materials. The synthesis of homogenous particles of defined size is therefore favorable.

For particle size and distribution measurements, laser diffraction analysis was performed. In these measurements, the active materials are dispersed in a liquid solution and pass through a measurement cell, where a laser beam is diffracted. The diffraction of the beam, due to the wave character of light, corresponds to the particle size and the incident wave length. The theory behind was developed by Mie in 1908 [91].

The particle size distribution was determined using a CILAS 1190 particle size analyzer. The cathode powders were dissolved in distilled water and Disperbyk-190 was used as dispergent for better dissolution. All measurements were performed at least twice and the average values are presented in this thesis. The data was analyzed using the integrated Particle Expert Software (CILAS).

5.1.3 Scanning electron microscopy (SEM)

Scanning electron microscopy is a very powerful tool for material characterization. It can visualize surfaces and textures and additionally gives information about chemical composition of the sample (in combination with electron dispersive X-ray spectroscopy - EDX). The basic principle is that if a high electron beam is decelerated by a sample, secondary electrons are generated. The detection of these secondary electrons, their energy and position leads to a two-dimensional picture of the measured sample surface. If the energy of the electrons is high enough, electrons from inner shells are excited. X-rays are emitted when these electrons return to their initial state, which corresponds directly to the difference in the energy of the states and is elemental specific.

Scanning electron microscopy was carried out using an FEI/Philips XL-30 Field Emission ESEM coupled with an EDAX CDU LEAP Detector. The samples were dried and sputtered with gold for conductivity enhancement prior to the analysis.

5.1.4 Transmission electron microscopy (TEM)

Transmission electron microscopy as the classical electron microscopic method works in a similar manner as light microscopes. The high energy electron beam passes through ultrahigh vacuum to the sample, and shows, due to the short wavelength of the electrons, a high resolution picture of the measured sample. The resolution can go down to nanometer scale and the gained information includes structural disorder/order, grain boundaries, and chemical identity (if electron energy loss is detected simultaneously). The samples have to be very thin to allow the electrons to pass through. The detector is located behind the sample.

TEM analysis for this work was carried out using a FEI Tecnai F20 TEM.

5.1.5 Inductively coupled plasma optical emission spectrometry (ICP-OES)

Inductively coupled optical emission spectroscopy is usually applied for trace elemental determination down to some nanograms per liter. The liquid sample is nebulized and excited through inductively coupled plasma. The emitted wavelength is elemental specific and detected via photomultiplier. The wavelengths are then counted and analyzed quantitatively and qualitatively such that nearly all elements can be detected.

In this work, the powders were chemically pulped using a nitric and chloric acid mixture under constant heating. Argon was used as analysis gas and the equipment was calibrated prior to the analysis. The equipment type was PerkinElmer OPTIMA 7300 DV and the data was analyzed using WinLab32 for ICP.

5.1.6 X-ray photoelectron spectroscopy (XPS)

X-ray photoelectron spectroscopy is an analysis tool for surface characterization based on the outer photoelectric effect. The sample interacts with an incident X-ray beam, so that electrons from inner orbitals at the surface of the sample are excited, emitted, and their energy detected. The detected energy is characteristic for the element and orbital where it is emitted and therefore the chemical identity and oxidation state are measured. Due to the low mean free path of the electrons, the technique is surface sensitive. The binding energy of the emitted photoelectron is detected and the results can be analyzed quantitatively and qualitatively.

For comparison between the oxidation states of symmetric NMC (commercial & non-commercial) and non-symmetric NMC as well as for visualization of surface oxidation of the powders, survey spectra were collected on the samples to detect all elements present at the surface. These elements have been evaluated quantitatively. However, this method only enables imprecise quantification of the Li content (due to the overlap with other components). Thus, for a quantitative analysis of the relative O, Li, Ni, Mn and Co content, detailed spectra of the respective regions were recorded. The samples were prepared by deposition of the powder onto conducting carbon tape. The X-ray source was Al-K α at 88 W using a SPECS u-Focus XPS system. Survey spectra were collected on all samples to detect all elements present at the surface. These elements were evaluated quantitatively. All data was processed with CASA-XPS software.

5.1.7 X-ray diffraction (XRD)

X-ray diffraction is used for analysis of crystal structures. Different phases present in the sample can be detected and quantitatively evaluated. Therefore, an incident X-ray beam is diffracted by a flat sample and detected. The wavelength of the X-rays are related to the diffraction angle and the lattice spacing of the crystal according to Bragg's law [92]:

$$2d\sin\theta = n\lambda \quad (5.2)$$

where d is the interplanar distance, θ is the scattering angle, n is a positive integer, and λ is the wavelength of the incident beam (see figure 5.2).

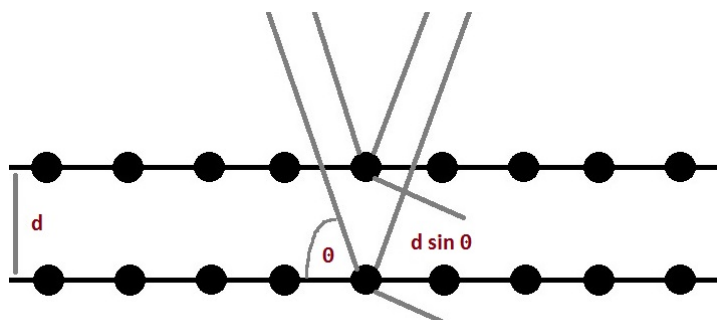


Figure 5.2: X-ray diffraction on a crystal.

X-ray diffraction patterns were recorded using a PANalytical X'Pert Pro Diffractometer with an X-Celerator Detector in the range 5-120° 2θ in steps of 0.0033422 ° 2θ and a count time of 400 seconds per step. A nickel filtered Cu-K α ($\lambda = 1.5418 \text{ \AA}$) radiation was used with the sample in flat plate θ/θ geometry.

As the diffraction peaks correlate to the crystal structure, a derived pattern can be fitted to expected phases with respect to peak position, width and shape so that the difference between the observed and expected profile derives a minima. The method is called Rietveld fit and can be applied to nuclear and X-ray diffraction patterns [93].

Structural analysis was carried out using a GSAS (General Structure Analysis System) package [94] with the EXPGUI interface [95]. In each case a polynomial background, scale factor, zero point, absorption correction, preferred orientation, coefficients for the peak shape function and cell parameters were refined. The structure of LiNi $_{1/3}$ Mn $_{1/3}$ Co $_{1/3}$ O $_2$ presented by Nazar et al. [96] was used as initial model (see table 5.1).

Table 5.1: Crystallographic parameters of NMC111.

Parameter	Value
Crystal system	Hexagonal
Space group	R -3 m
a (\AA)	2.86
b (\AA)	2.86
c (\AA)	14.227
α ($^\circ$)	90.00000
β ($^\circ$)	90.00000
γ ($^\circ$)	120.00000

For the non-symmetric composition, the fractions of the transition metals were altered accordingly. In this starting model, 2.5 % of cation mixing between Ni and Li was assumed (which is likely to occur due to their similar ionic radii of 0.69 and 0.76 \AA , respectively [97]).

5.2 Results and Discussion

5.2.1 Symmetric NMC

Chemical composition and impurities

Chloride precursors are usually not applied for the synthesis of NMC. Here, chloride precursor was chosen due to easy accessibility and interest from the industry to determine the impact of possible chloride impurities which might arise during the production process.

The results of the ICP-OES analysis and the anions determination in the powders using chloride precursors at different synthesis temperatures are presented in Table 5.2.

Table 5.2: Results of ICP-OES analysis and anion determination using chloride precursor.

Sample	Temperature [°C]	Real composition	Chlorides [mg kg ⁻¹]
C β	500	Li _{1.04} Ni _{0.33} Mn _{0.33} Co _{0.32} O _{1.98}	260
C 1	900	Li _{0.99} Ni _{0.34} Mn _{0.33} Co _{0.33} O _{2.00}	28.5
C 2	920	Li _{0.99} Ni _{0.32} Mn _{0.32} Co _{0.31} O _{2.06}	35.5

The same measurements were performed for nitrate precursor (see Table 5.3).

Table 5.3: Results of ICP-OES analysis and anion determination using nitrate precursor.

Sample	Temperature [°C]	Real composition	Nitrates [mg kg ⁻¹]
N β	500	Li _{1.00} Ni _{0.31} Mn _{0.32} Co _{0.31} O _{2.06}	2900
N 1	900	Li _{0.95} Ni _{0.33} Mn _{0.34} Co _{0.33} O _{2.05}	92
N 2	920	Li _{0.95} Ni _{0.33} Mn _{0.34} Co _{0.33} O _{2.06}	<10

For both precursors, nitrates and chlorides, the amount of lithium decreases with increasing temperature. Lithium is therefore usually added in slight excess of the amount stoichiometrically required [98] [97]. This tendency is less for the chloride prepared samples compared to the nitrate ones. The transition metals show no obvious temperature-dependent trend in composition variation with temperature for both precursors.

The amount of anion impurities for nitrate precursors decreased with temperature so, that at 920 °C it was below the detection limit of 10 ppm. For chloride prepared samples, the amount of chloride anions present in the powders calcined at higher temperatures was around 30 ppm, which is lower at 900 °C compared to the nitrate synthesis but higher for 920 °C. The increased amount of chlorides at the highest temperature is not significant as the samples were separated after the washing step, and no other chloride source was present afterwards.

Overall the results prove that the amount of lithium source for the synthesis must be increased with increasing synthesis temperature due to lithium losses. Additionally, the washing step during the synthesis is crucial regarding the anion impurities remaining in the powders, especially for chloride precursors, which show no decreasing trend with increasing temperature around 900 °C. In contrast, the nitrates remaining in the structure after the washing step are more sensitive to temperature and can therefore be totally removed at 920 °C.

Powder morphology

Scanning electron microscopy was performed for visualization of the powders and their particle size and morphology. The images show homogenous spherically shaped particles on the nanometer-scale for all samples (example see Figure 5.3).

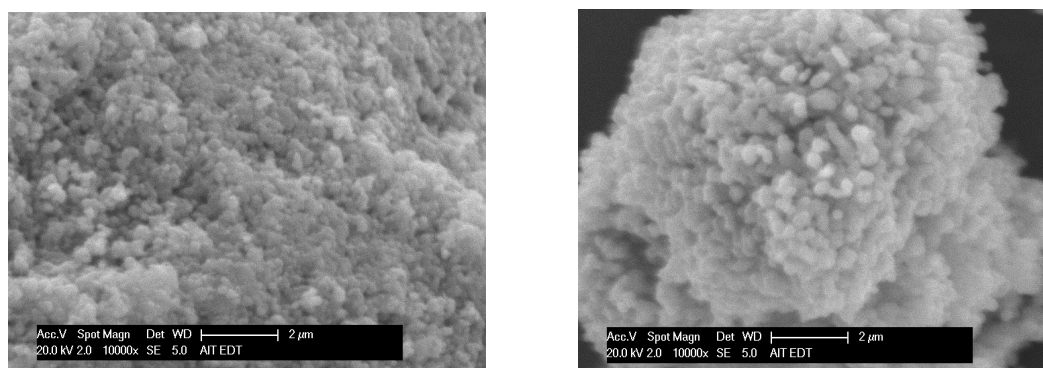


Figure 5.3: SEM image of NMC synthesized using nitrate (left) and chloride (right) precursors.

There are no obvious differences between the powders synthesized with nitrate or chloride precursors in the SEM images, despite larger primary particles for chloride-prepared samples. The different temperatures at the second stage produce no evident differences in size and shape and are therefore not presented here.

The primary nanometer particles tend to agglomerate into larger secondary particles, which have diameters around 5-10 μm as shown in the SEM image of the chloride synthesis on the right side.

Laser diffraction measurements prove this behaviour. The particle size distributions of all synthesized materials show a bimodal curve, where the main peaks correspond to the larger secondary particles at around 10 μm and to the smaller primary particles below 1 μm (example see Figure 5.4).

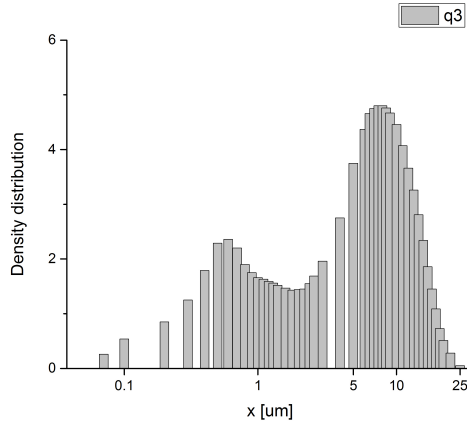


Figure 5.4: Example for particle size distribution of NMC.

Taking into account that in these experiments additives were applied for better dispersion and the solution was homogenized in an ultrasonic bath, the secondary particles don't seem to break up into their primary particles easily. To achieve high tap density and energy density of the active materials, the formation of secondary particles is favorable [98].

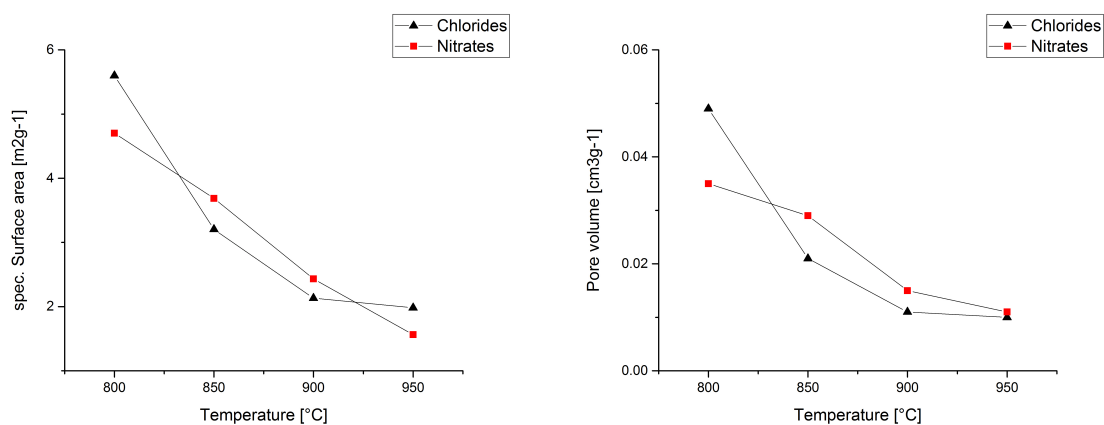
The particle sizes of the individual syntheses as derived by laser diffraction are presented in Table 5.4. The particle size increases with temperature for both chloride and nitrate precursors. The particle size is smaller when using chlorides; additionally, the particle size distribution is more narrow compared to nitrates. This means more homogeneity in terms of particle size which is more favorable for electrode preparation as a substantial difference leads to larger lithium concentration gradients during cycling [99].

In contrast, comparison of the SEM images of both precursors showed larger primary particles after chloride synthesis than with nitrate. This is an indication that even though the primary particles are larger in chloride-prepared samples, they seem to agglomerate into smaller secondary particles, as measured in the laser diffraction experiments.

Table 5.4: Particle size distribution of symmetric NMC.

Precursor	Temperature [°C]	D10	D50	D90
Chlorides	800	0.14	0.79	11.58
Chlorides	850	0.15	0.87	13.75
Chlorides	900	0.13	0.61	13.79
Chlorides	950	0.22	2.47	23.20
Nitrates	800	0.18	3.51	37.53
Nitrates	850	0.16	1.44	37.21
Nitrates	900	0.40	15.44	45.13
Nitrates	950	0.33	9.88	46.40

The specific surface areas of the corresponding materials was determined via gas adsorption measurements (see Figure 5.5).

**Figure 5.5: Specific surface areas and pore volumes for different synthesis conditions (temperatures and precursors).**

The trend is similar for both chloride and nitrate precursors. The pore volumes as well as the specific surface areas of the active materials decrease with increasing synthesis temperatures. The specific surface areas as well as the pore volumes are higher using nitrates for the intermediate temperatures (850 °C and 900 °C), but smaller for lower or higher temperatures.

The correlation between the observed parameters is clear: a higher amount of smaller particles lead to a higher specific surface area and therefore also to smaller pore volumes.

The previously discussed effect of agglomeration is not reflected in the gas adsorption measurements since nitrogen penetrates the secondary particles and can also be adsorbed at the inner surfaces of the primary particles.

The effect of particle size on cathode performance is twofold: Larger particles (especially at higher currents) lead to increasing lithium concentration gradients; the solid-state diffusion of lithium can be limited, and high stresses can arise inside the particles. Smaller particles have high surface areas, which are favorable in that they lead to larger reaction area as well as better lithium ion kinetics.

On the other hand, for industrial applications, too small particles on the nanometer scale are difficult to handle in terms of safety, packaging density, and processability [99] [100]. The presented NMC powders consist of small nanosized particles, with decreased diffusion paths of charged species which are agglomerated into larger spherical secondary particles to achieve both high tap and high energy density, and are therefore optimized active materials in terms of powder morphology.

Crystal structure

X-ray diffraction patterns were recorded at different temperature stages for comparison of the crystallinity and possible phase changes during synthesis. Figure 5.6 shows the X-ray diffraction pattern at different stages of the synthesis.

The first stage at 120 °C, is the washed and dried precipitate, the intermediate product, which is composed of mixed transition metal hydroxides. Low crystallinity is achieved already at this stage of synthesis. The second pattern corresponds to the first oven step at 500 °C, at which lithium was already added, ball-milled with the precursor, and heated for several hours. The main peaks are visible already, but still the crystallinity of the sample is low and the peaks are broad compared to the final product. The peak splitting of the (108)/(110) hkl lines as well as sharp (003) and (104) peaks are obtained for the last sample, which was further heated to 900 °C. All diffraction peaks at the last stage can be indexed on the hexagonal R-3m model, the typical α -NaFeO₂ structure.

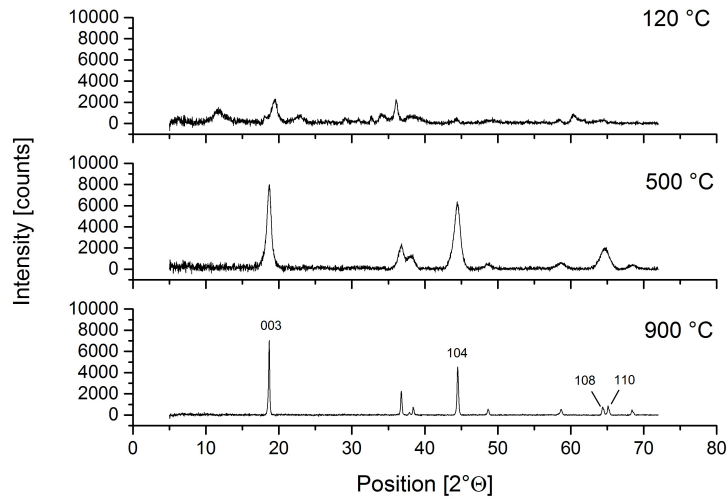


Figure 5.6: X-ray diffraction pattern at different stages of the synthesis.

Transmission electron microscopy revealed the two main lattice planes (see Figure 5.7).

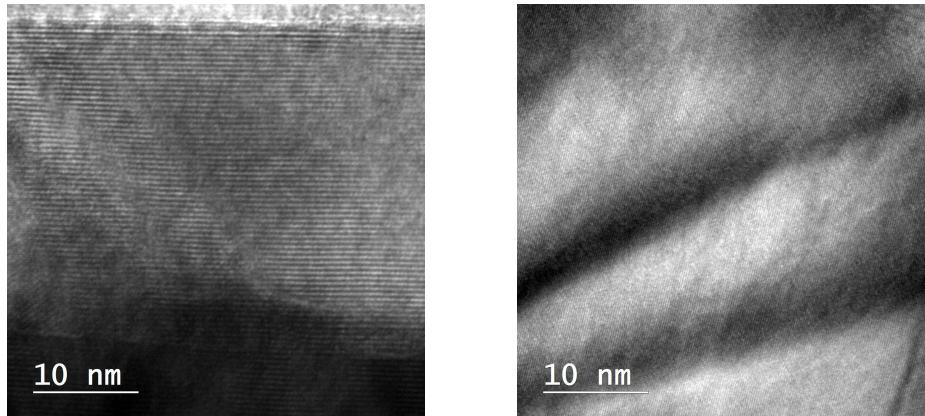


Figure 5.7: TEM images of NMC using chloride (left) and nitrate (right) precursors.

The lattice plane distances d observed were 0.21 nm and 0.50 nm, averaged from 5 interplanar distances. They correspond to the lattice planes (104) and (003), respectively, as calculated from the corresponding real unit cell parameters obtained by Rietveld fit of X-ray diffraction patterns (as presented later) and the following equation for hexagonal lattices:

$$d_{hkl} = \frac{a}{\frac{4}{3}(h^2 + hk + k^2) + \frac{a^2}{c^2} \cdot l^2} \quad (5.3)$$

The unit cell parameters for each synthesis were determined using Rietveld fit of the recorded X-ray diffraction patterns for all samples (see Figure 5.8).

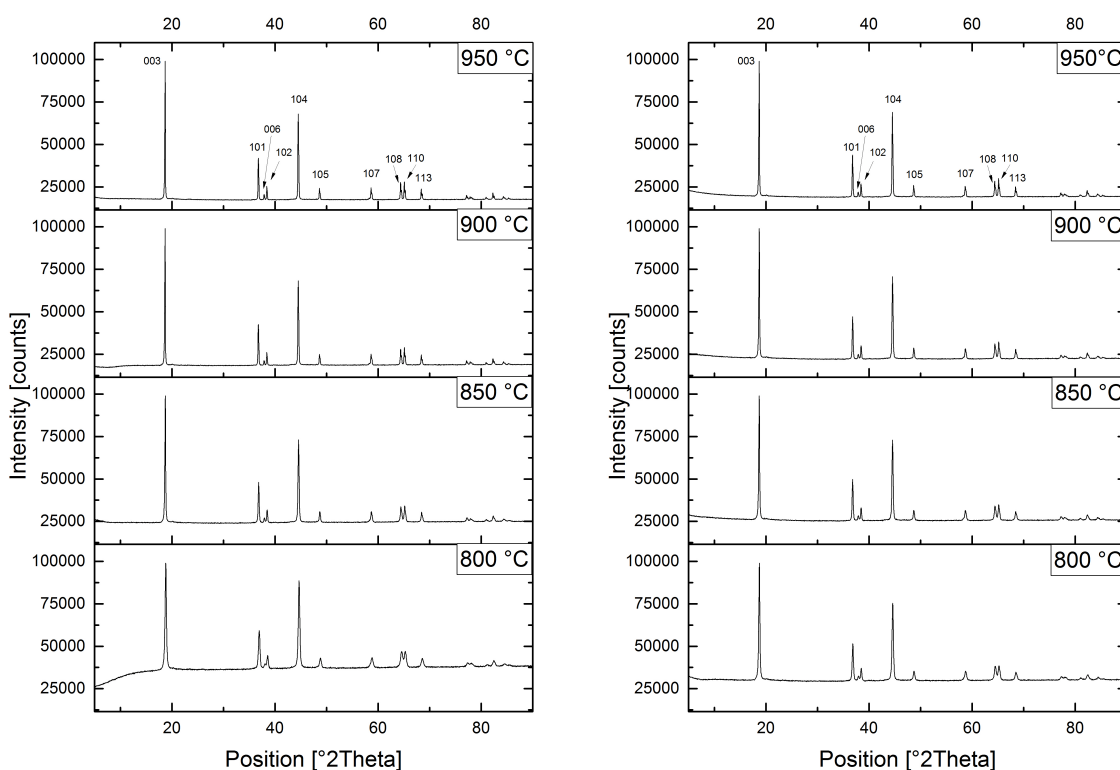


Figure 5.8: XRD pattern of NMC using chloride (left) and nitrate (right) precursors.

There is little obvious difference between the samples prepared using the two types of precursor. Figure 5.9 presents the refined unit cell parameter variation as well as the lithium-nickel cation mixing for different precursors and calcination temperatures.

The results from using nitrate or chloride precursors are similar: Both axes, a and c , corresponding to interslab and intraslab distances of the transition metal oxide layers, decrease with increasing temperatures up to 900 °C and slightly increase again at 950 °C. These trends are reflected in the volume expansion. The increase in volume with increased synthesis temperature is associated with loss of lithia at higher temperatures and a degree of reduction of the transition metal cations occurring at 950 °C.

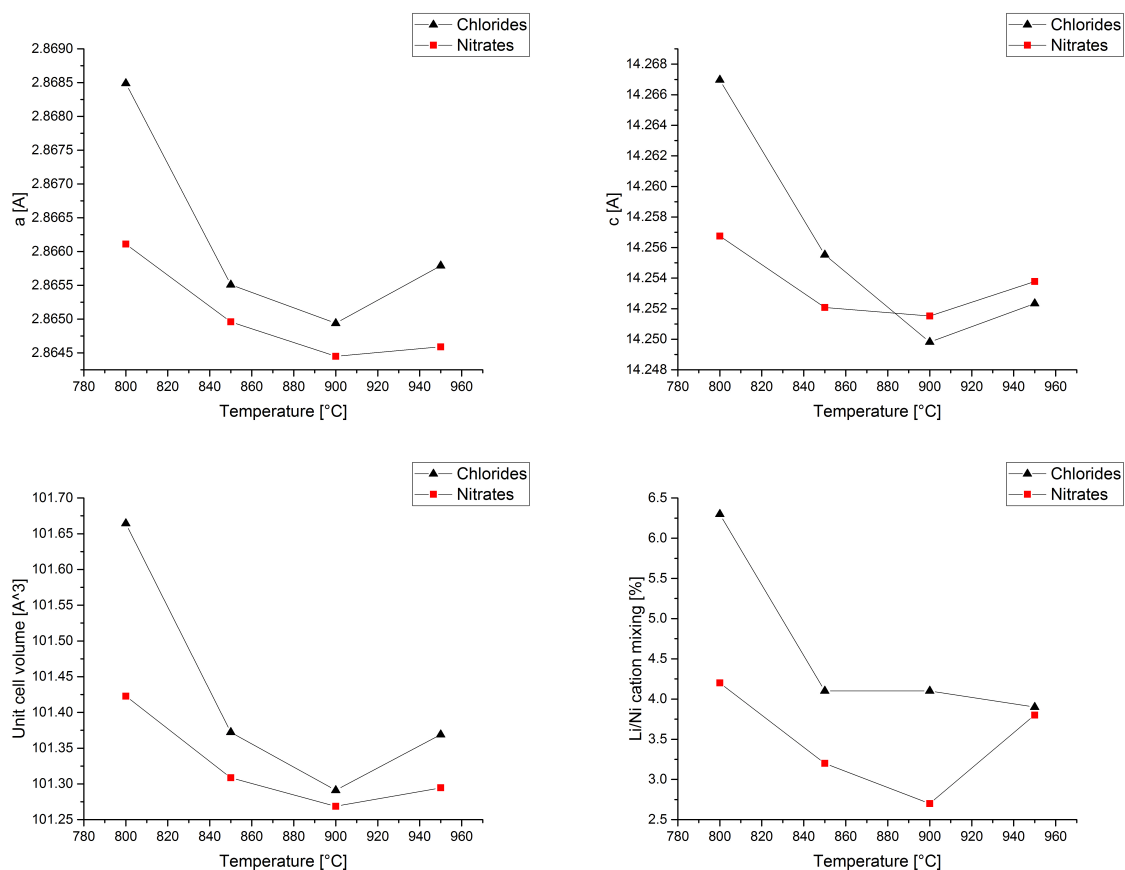


Figure 5.9: Unit cell parameters and amount of lithium/nickel cation mixing derived by Rietveld fit.

The amount of lithium-nickel cation mixing shows also a decreasing trend with increasing synthesis temperature and minima at 900 °C for both precursors. When chloride precursors are used, the amount of cation mixing in the structure is significantly higher than in the synthesis from nitrate precursors. The difference decreases with rising temperature, and at 950 °C the values are nearly the same. This is caused by the fact that, except for the lowest temperature stage, the cation mixing is nearly constant for chloride precursors (even though it shows a slightly decreasing trend). The crystallinity and ordering of the samples increases with increasing synthesis temperature; consequently, temperatures of 800 °C or below are not beneficial for calcination in synthesis of symmetric NMC via coprecipitation.

Influence of oxygen content in the atmosphere during calcination

In contrast to other physico-chemical data presented above, unit cell parameters, the amount of cation mixing, and ion distribution as derived by energy dispersive X-ray spectroscopy (EDX) was significantly different between samples prepared under constant flow of synthetic air and those calcined in the muffle oven.

Table 5.5 presents the results obtained from EDX measurements of the corresponding samples, all prepared at 900 °C. N refers to nitrate precursors while C refers to chloride ones; SA indicates synthetic air flow while MO stands for samples prepared in the muffle oven.

Table 5.5: Distribution of the transition metals and oxygen in NMC111 synthesized under different atmospheric conditions.

Sample	Ni [At%]	Mn [At%]	Co [At%]	O [At%]	O/TM
111 N SA	10.76	10.78	11.17	67.29	2.06
111 C SA	10.94	9.50	10.26	69.41	2.26
111 N MO	12.19	11.65	11.85	64.30	1.80
111 C MO	14.66	13.70	13.92	57.73	1.37

These results are normalized to 100%, the ratio between oxygen and the sum of the transition metals (TM) should be 1 to 2. EDX measurements were performed at different spots of the sample powders and average values are presented in the table. One can see that under constant air flow and oxygen-rich atmosphere the ratio between the oxygen and the transition metals is much higher than in NMC samples prepared in the muffle oven. The influence of the amount of oxygen in the calcination atmosphere is higher when chloride precursors are used for synthesis of NMC111. The final composition varies more in comparison with nitrate prepared samples.

Lithium is not detectable with this method, but as already presented, the possibility of lithia loss in these structures, which would also explain oxygen deficiency within the structure, and unit cell parameter changes. Overall, there is evidence to suggest lithia loss for layered oxide samples calcined in atmospheres which contain less oxygen.

Table 5.6 presents the unit cell parameters as well as the amount of lithium-nickel cation mixing, as derived by Rietveld fit of the corresponding XRD pattern.

Table 5.6: Unit cell parameters and cation mixing for NMC111 derived by Rietveld fit.

Sample	a [\AA]	c [\AA]	Volume [\AA^3]	Cation mixing [%]
111 N SA	2.8675	14.2777	101.674	2.0
111 C SA	2.8672	14.2639	101.549	3.2
111 N MO	2.8645	14.2515	101.269	2.7
111 C MO	2.8652	14.2554	101.347	5.9

The amount of cation mixing at 900 °C is generally lower for nitrate-prepared NMC samples than for chloride ones, as already discussed for different calcination temperatures and types of precursors.

Additionally, in oxygen-rich atmosphere, the amount of lithium-nickel cation mixing is significantly lower for both precursors, showing a stronger characteristic for chloride prepared samples, which have more than 5% when prepared in the muffle oven. This can lead to significant decrease in terms of capacity of the cathode material due to blocking of lithium diffusion pathways during cycling.

The influence of oxygen deficiency as well as cation mixing on the electrochemical performance in symmetric NMC samples will be discussed below.

5.2.2 Non-symmetric NMC

Chemical composition

The chemical composition for all syntheses of non-symmetric NMC (in this case with 5:3:2 ratio of Ni:Mn:Co) in terms of using two different precursors (nitrates and chlorides) and four different calcination temperatures was determined.

Table 5.7: Results of ICP-OES analysis of NMC532 using nitrate (N) and chloride (C) precursors.

Sample	Temperature [°C]	Real composition	Li/M ratio
532 N 1	800	$\text{Li}_{0.95}\text{Ni}_{0.50}\text{Mn}_{0.30}\text{Co}_{0.20}\text{O}_{2.03}$	0.95
532 N 2	850	$\text{Li}_{0.95}\text{Ni}_{0.49}\text{Mn}_{0.29}\text{Co}_{0.20}\text{O}_{2.07}$	0.96
532 N 3	900	$\text{Li}_{0.96}\text{Ni}_{0.51}\text{Mn}_{0.30}\text{Co}_{0.20}\text{O}_{2.03}$	0.95
532 N 4	950	$\text{Li}_{0.95}\text{Ni}_{0.51}\text{Mn}_{0.30}\text{Co}_{0.20}\text{O}_{2.04}$	0.93
532 C 1	800	$\text{Li}_{0.99}\text{Ni}_{0.51}\text{Mn}_{0.29}\text{Co}_{0.20}\text{O}_{2.01}$	0.99
532 C 2	850	$\text{Li}_{0.96}\text{Ni}_{0.52}\text{Mn}_{0.29}\text{Co}_{0.20}\text{O}_{2.04}$	0.96
532 C 3	900	$\text{Li}_{0.97}\text{Ni}_{0.53}\text{Mn}_{0.29}\text{Co}_{0.20}\text{O}_{2.01}$	0.95
532 C 4	950	$\text{Li}_{0.96}\text{Ni}_{0.53}\text{Mn}_{0.29}\text{Co}_{0.20}\text{O}_{2.02}$	0.94

Similar to the symmetric composition of NMC, the trend regarding the amount of lithium in the structure decreases with increasing temperature. Another reason for the lithium deficiency in the samples, besides lithium loss at higher temperatures, might be caused by the washing step. During repeated rising of the samples with deionized water in order to remove Na^+ and Cl^- or NO_3^- completely, Li^+ ion exchange with H^+ occurs as already reported [101] [102].

Nickel, Manganese, and Cobalt show no obvious trend tied to calcination temperature. Therefore, the ratio between lithium and the sum of the transition metals in the chemical formula was calculated. Figure 5.10 shows the variation of Li/M mol% ratios with calcination temperature ($M=\text{Ni}+\text{Mn}+\text{Co}$).

A general decreasing trend in Li/M is observed with increasing temperatures for both nitrate and chloride precursor samples. This trend is stronger for chloride-prepared samples, while using nitrate precursors leads to the highest Li/M-ratio at 850 °C. This behaviour again reveals the loss of lithium at higher temperatures for both syntheses.

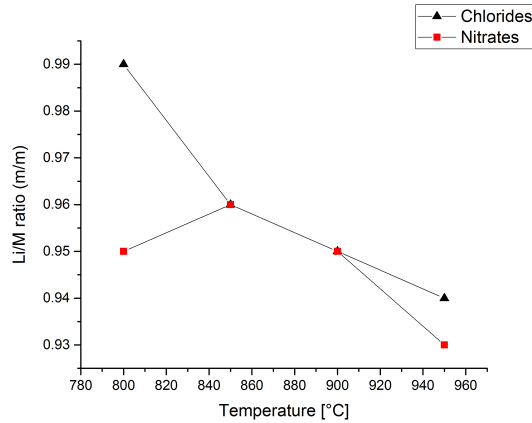


Figure 5.10: Variation of the Li/M-ratio of NMC532 with synthesis temperature.

Powder morphology

In order to visualize the morphology and particle size and shape, SEM images were recorded from all samples. They all show analogous particle shapes and morphologies and therefore, as an example of the trend for different synthesis temperatures, the chloride syntheses are presented here (see Figure 5.11).

Smaller, nano-sized particles seem to agglomerate into larger secondary particles in a similar manner as NMC synthesized in symmetric composition. The particle size seem to increase with increasing calcination temperature. To prove this, laser diffraction measurements were performed (see Table 5.8).

Table 5.8: Particle size distribution of non-symmetric NMC.

Precursor	Temperature [°C]	D10	D50	D90
Chlorides	800	0.12	0.57	2.90
Chlorides	850	0.15	0.85	3.95
Chlorides	900	0.41	3.21	34.66
Chlorides	950	1.03	12.38	74.74
Nitrates	800	0.24	2.37	21.59
Nitrates	850	0.36	3.42	22.77
Nitrates	900	0.20	1.43	15.37
Nitrates	800	0.66	3.95	25.70

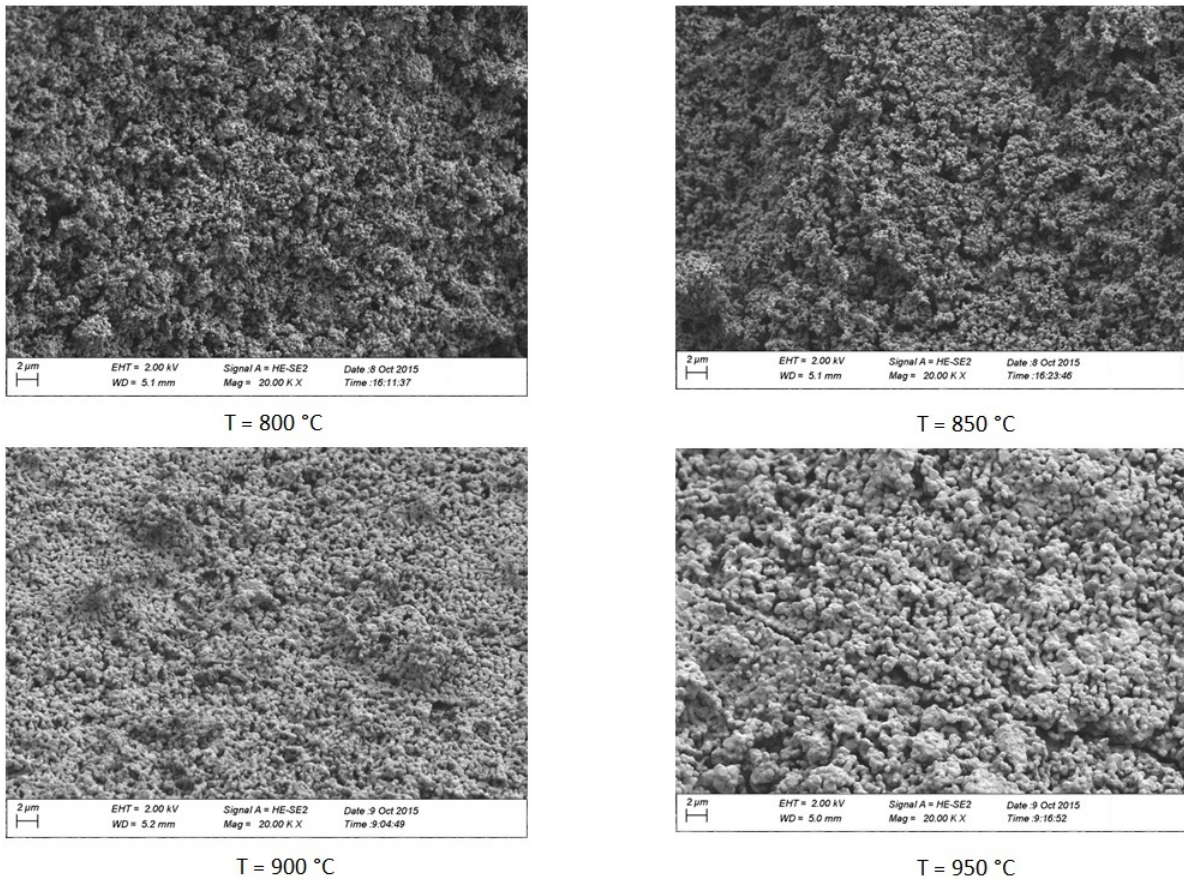


Figure 5.11: SEM images of NMC532 synthesized at different temperatures.

The results show the same behaviour as in NMC111: an increasing particle size with increasing temperature for both precursors used. Again, chloride-prepared samples have smaller particle sizes with a more narrow distribution over the whole range. To evaluate the differences between symmetric and non-symmetric compositions, their corresponding D50 parameters were plotted against calcination temperature (see Figure 5.12).

Again, one can see the tendency of particle sizes increase with calcination temperature for the chloride synthesis on the left side for both compositions. Interestingly, the differences with increasing temperature are higher for NMC532, which again could indicate reduction of the transition metals at higher temperatures, especially nickel ions. For nitrate-prepared samples, the differences between NMC532 samples are quite low, while the increasing trend is visible again for NMC111, which shows largest particle sizes at 900 °C, which is also the highest obtained particle size for all syntheses.

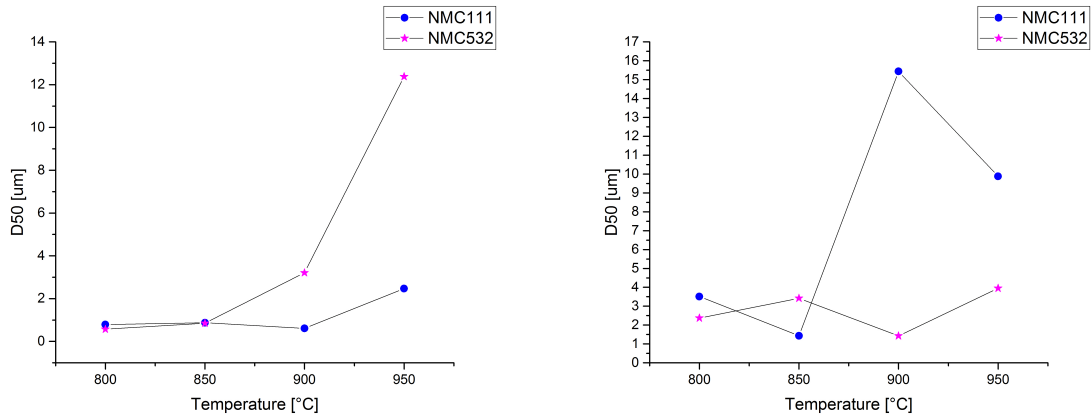


Figure 5.12: D50 parameter using chloride (left) and nitrate (right) precursors for different synthesis temperatures.

Gas adsorption measurements were performed to obtain the specific surface areas and porosity of the synthesized NMC532 powders. The results are presented in Table 5.9.

Table 5.9: Results from gas adsorption measurements of NMC532 using nitrate (N) and chloride (C) precursors.

Sample	Temperature [°C]	Specific surface area [m ² g ⁻¹]	Average pore diameter [nm]	Average pore volume [cm ³ g ⁻¹]
532 N 1	800	4.125	2.720	0.060
532 N 2	850	3.371	2.717	0.019
532 N 3	900	3.334	3.031	0.022
532 N 4	950	2.160	2.714	0.014
532 C 1	800	2.877	3.035	0.040
532 C 2	850	1.728	2.716	0.025
532 C 3	900	3.834	3.794	0.009
532 C 4	950	0.925	3.797	0.003

For NMC532 synthesized with nitrate precursors, the specific surface area decreases with increasing calcination temperature. This corresponds to the increasing pore volume similar to that revealed through characterization of NMC111 syntheses. On the other hand, when chloride precursors are used, there is no visible correlation between the measured specific surface area and the synthesis temperature. The pore volume shows similar behaviour to the specific area.

Crystal structure

X-ray diffraction patterns were recorded similar to those of symmetric NMC111. The observed pattern showed the same peaks and positions for symmetric and non-symmetric composition and no obvious differences between them (see Figure 5.13).

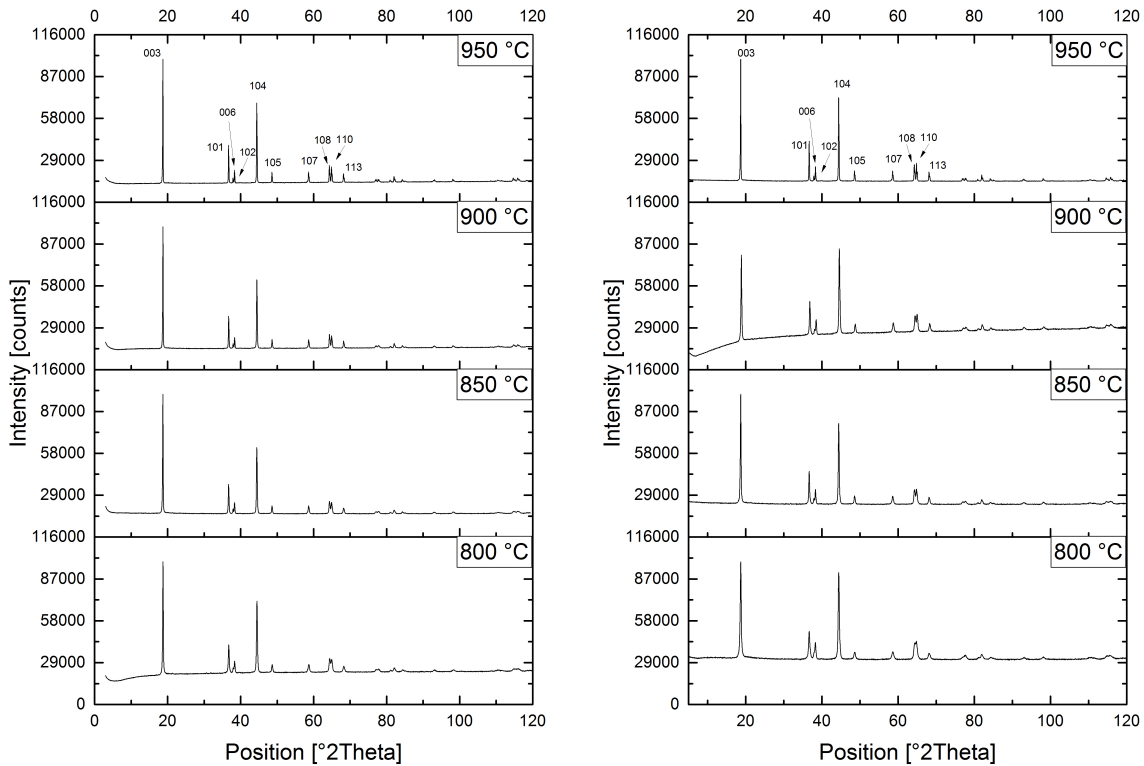


Figure 5.13: XRD pattern of NMC532 using chloride (left) and nitrate (right) precursors.

These X-ray diffraction patterns were refined accordingly, changing the mole fraction of the transition metals according to the synthesized product NMC532. Figure 5.14 shows the refined unit cell parameters for each calcination temperature.

NMC532 shows a slightly decreasing trend in the a-axis dimension with increasing calcination temperature for the nitrate precursor synthesis, but a general increasing trend in this parameter for chloride precursor synthesis. The c-axis parameter for NMC532 shows an increasing trend with increasing temperature. These trends are reflected in the plots of volume, with that for the nitrate synthesis showing little change with calcination temperature, but that for the chloride synthesis showing an increasing trend.

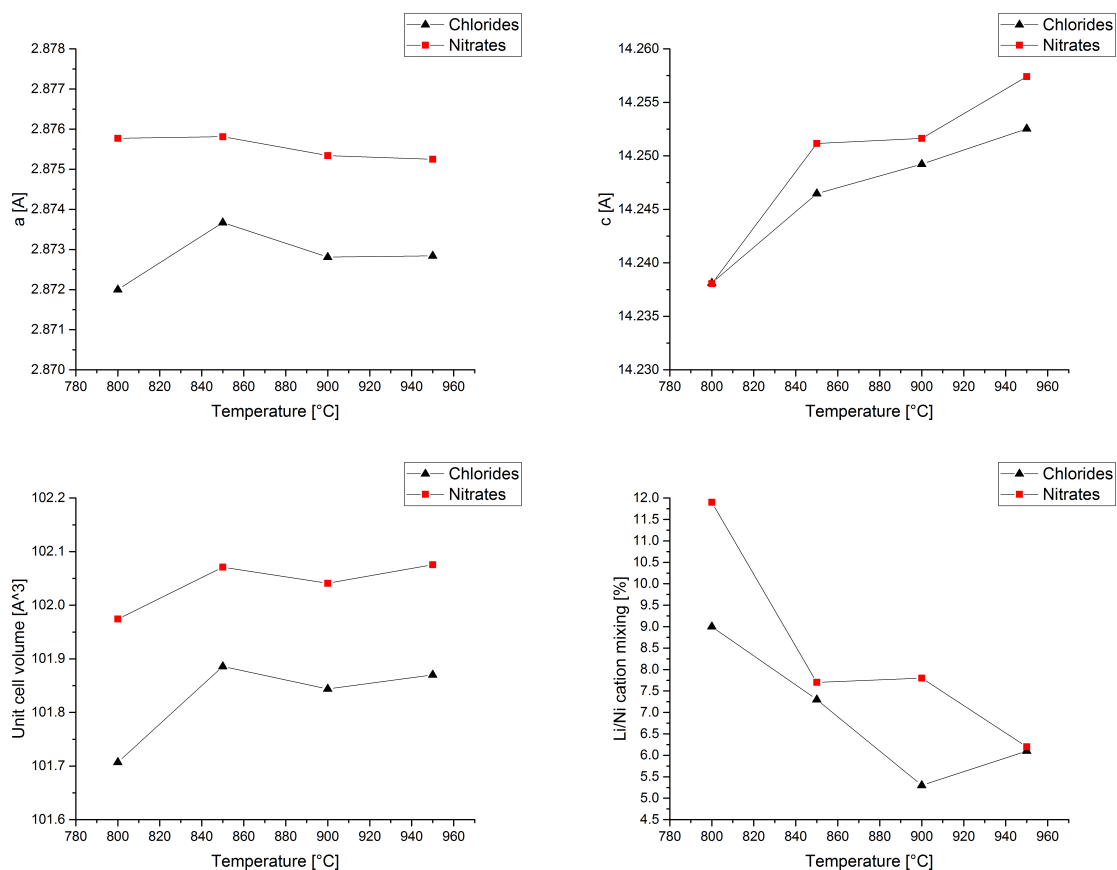


Figure 5.14: Unit cell parameters and amount of lithium/nickel cation mixing of NMC532 derived by Rietveld fit.

The amount of cation mixing generally decreases with temperature for both chloride and nitrate precursors, but slightly increases at 950 °C when using chloride precursor. Lithium/nickel cation mixing is higher for the nitrate precursor and generally, due to the higher amount of nickel, higher than for NMC111.

The unit cell volume variation can be correlated to the lithium/transition metals-ratio for chloride-synthesized samples. Due to the near constant unit cell volume of nitrate-prepared samples, there is poor correlation with temperature for this synthesis.

For evaluation of the differences between the symmetric and non-symmetric compositions, two selected self-synthesized samples were analyzed with X-ray photoelectron spectroscopy and compared to commercial symmetric NMC, as delivered by BASF and Sigma Aldrich (see Figure 5.15).

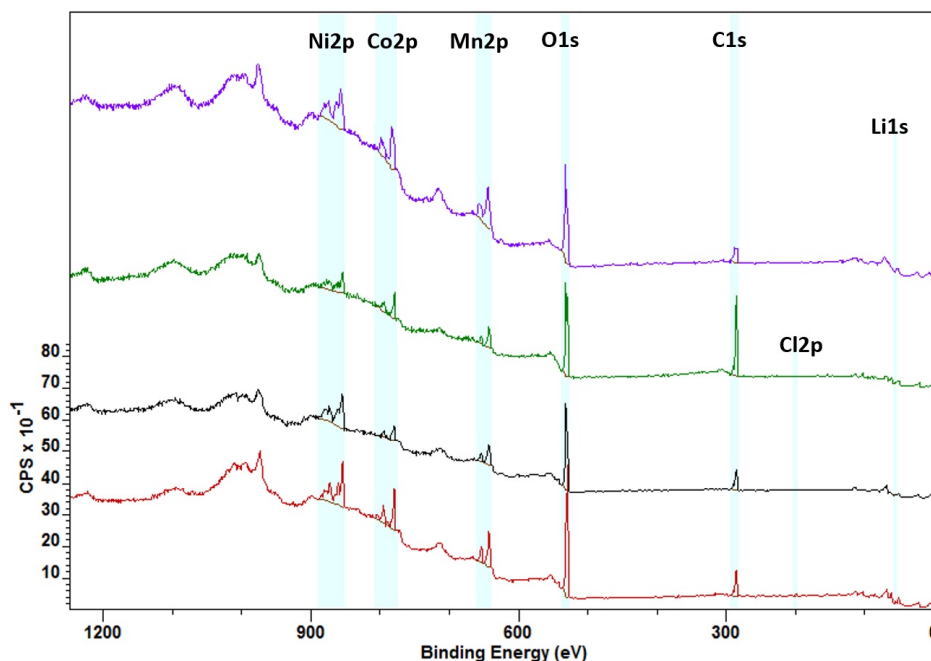


Figure 5.15: XPS survey spectra of self-synthesized samples NMC111 (red), NMC532 (black) and commercial NMC111 samples from BASF (green) and Sigma Aldrich (purple).

Table 5.10 shows the relative contents of the samples.

Table 5.10: Relative O, Mn, Ni and Li contents for NMC111, NMC532 and two commercial samples.

Sample	O [at%]	Co [at%]	Mn [at%]	Ni [at%]	Li [at%]
NMC111	40.0	2.9	4.6	4.8	31.0
BASF	37.2	1.5	2.1	2.3	26.5
Sigma Aldrich	59.6	6.2	8.3	6.5	-
NMC532	38.8	1.4	3.6	5.3	30.7

All components of the NMC111 delivered by Sigma Aldrich show a shift towards higher binding energies and broadening of the peaks towards lower binding energies, which makes the determination of the Li content in this sample practically impossible. This effect is usually seen in samples which are not sufficiently conductive and therefore charging effects occur when exposed to x-ray radiation.

The excessive amount of nickel in the NMC532 is revealed as well, while all other samples show similar ratios between their transition metals, as expected. The amount of lithium detected in the powders seems higher than expected; this could be due to aggregation of lithium compounds on the powder particle surfaces.

Additionally, detailed spectra of the respective regions have been recorded for the investigation of the oxidation states of the transition metal components (see Table 5.11).

Table 5.11: Determined oxidation states of the transition metals for symmetric and non-symmetric NMC.

Sample	Ni ²⁺ [at%]	Ni ³⁺ [at%]	Mn ³⁺ [at%]	Mn ⁴⁺ [at%]	Mn ⁶⁺ [at%]	Mn ⁷⁺ [at%]	Co ²⁺ [at%]	Co ³⁺ [at%]
NMC111	76.76	23.24	21.1	47.5	15.0	16.4	12.3	87.7
BASF	73.47	26.53	20.9	49.7	11.6	17.8	21.2	78.8
NMC532	58.03	41.97	14.1	43.3	15.8	26.7	32.8	67.1

Extracting information about the valency of metal oxides/hydroxides is not straightforward. All spectra have been corrected in binding energy according to the oxygen and carbon signals. On each of these spectra, line fits have been carried out, using multiple peaks corresponding to components of different oxidation states.

As to the author’s knowledge, this method has not been used before for oxidation state estimation in mixed transition metal oxides; the results should be regarded as best estimates.

For all measured samples, the ratio between Ni²⁺ and Ni³⁺ is 3:1 with the exception of the non-symmetric NMC532, which shows a larger content of trivalent nickel. Only half of the manganese seem to be in the expected Mn⁴⁺ state; suprisingly, only 3+ and 4+ states did not add up to the obtained spectra, while the addition of higher valencies led to satisfactory results (see Figure 5.16).

Regarding the cobalt valencies, for all compositions, the main species is Co³⁺, as expected, and varies between 67 and 87 at%.

All samples showed clear oxygen signals at binding energies where metal oxides are typically found (around 529 eV).

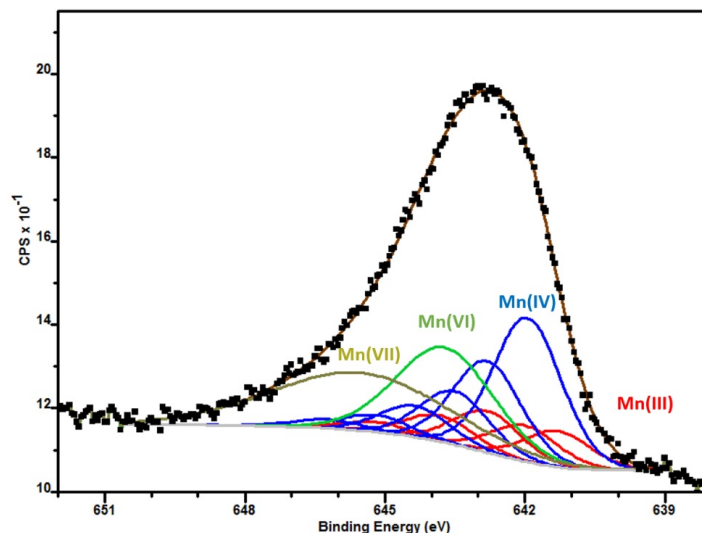


Figure 5.16: XPS detail spectra of the Mn $2p_{3/2}$ region of NMC111.

Overall, the XPS analysis revealed the dominant oxidation states in NMC111 of Ni, Mn and Co to be 2+, 4+ and 3+, as expected. The non-symmetric composition NMC532 showed higher amount of nickel in 3+ state. The reduction of nickel is caused by the higher amount of nickel present in the powder and reduction of the other transition metals, mostly cobalt, which have higher oxidation states, to provide electroneutrality within the structure.

The detailed spectrum of the Mn $2p_{3/2}$ region of NMC111 supports the statement at the beginning of this chapter, that the oxidation states are difficult to determine for mixed oxide structures and should therefore be accepted with caution, especially regarding absolute values [103] [104].

These findings disagree with the results of the electronic structure calculations, as presented in the previous section. The interpreted oxidation numbers up to 7+ of manganese are not reasonable and therefore questioned by the author. It could be related to the shift of the core states, as also observed by calculated density of states (DOS).

5.3 Conclusion

Physico-chemical characterization for both symmetric and non-symmetric compositions of synthesized NMC was performed and evaluated with respect to two different types of precursors: nitrates, which are commonly used, and chlorides due to industrial interest for possibly large-scale application in well-known spray roasting techniques for production of metal oxides [105]. The evaluation included microscopic observation, crystal structure determination, particle size measurements, and surface area determination.

It was shown that coprecipitation is a good method and easy to apply for synthesis of single-phase NMC with high crystallinity and homogeneous particle morphology, size and shape. The bottleneck in the synthesis process is the washing step, which influences not only the amount of remaining impurities from the precursors but can also, if taken to excess, lead to lithium ion exchange with hydrogen ions and further lithium deficiency in the final structure.

The amount of residual impurities for the samples prepared from nitrate precursors was higher after the washing step but more sensitive to temperature and therefore could be removed with the final heat treatment step. If chloride precursors are used, impurities are simply removed through deionized water, but about 30 ppm remained in the final structure and did not change with temperature. The industrially acceptable amounts of impurities from sodium or chloride are $< 0.01\%$, which is far from the derived values for the final products.

The amount of lithium decreases with increasing synthesis temperature, as observed from ICP-OES analysis for both compositions (NMC111 and NMC532). Meanwhile, the transition metals showed no clear trend. This effect is present for both precursors, but stronger when nitrates are used.

SEM analysis of the powder morphology shows that the mixed transition metal oxides consist of spherical particles on a nanometer scale which tend to agglomerate into closely packed secondary particles of some micrometers of size (up to about $10\ \mu\text{m}$). This characteristic is beneficial in two ways: first, the small nanosized particles provide short lithium diffusion pathways, low mechanical stresses and a high reaction area. Second, the agglomeration into larger secondary particles increases the tap and energy density of the active material and enhances safety and industrial processability.

Crystal structure determination from X-ray diffraction of all synthesized samples (NMC111 and NMC532) showed single-phase α -NaFeO₂ structure. The main peaks are indexed as (104) and (003), which were also calculated from the lattice plane distances derived by TEM analysis.

Temperatures below 850 °C are not beneficial for both used precursors due to lower crystallinity and a high amount of cation mixing. To decrease the amount of trapped lithium in the structure and ensure cycleability, cation mixing should not exceed 5%. Cation mixing is more prevalent in the chloride-prepared samples for NMC111, but for non-symmetric composition, it shows opposite trend. As more nickel is present in the NMC532, this effect is even stronger compared to the symmetric NMC, but decreases with temperature and reaches acceptable values at 900 °C calcination temperature.

Obviously, for symmetric NMC using nitrates at 900 °C, there is some different behaviour which is reflected in all physico-chemical parameters (e.g. particle size, unit cell parameters) and should be additionally reviewed, also regarding electrochemical characteristics in the next section.

From XPS analysis results it seems that lithium agglomerates at the surface of the particles. Additionally, the main oxidation states from the transition metals were determined as 2+, 4+ and 3+ for nickel, manganese and cobalt, respectively. Comparing NMC111 to NMC532, the amount of Ni²⁺ is lower for the non-symmetric composition. This can be linked to the lower amount of Mn⁴⁺, which has to be compensated to achieve electroneutrality within the structure.

The oxygen content of the atmosphere during the calcination process influences significantly the lithium-nickel cation mixing and the oxygen-transition metal ratio for characterized symmetric NMC samples. This can be correlated to lithia loss as observed from unit cell parameter changes derived by Rietveld fit.

Overall, the synthesized materials show good physico-chemical characteristics such as nanosized primary particles agglomerated into larger spheres to ensure high tap density. The synthesis temperature, according to crystallographic data, should not be set below 850 °C due to increased cation mixing. The amount of impurities remained in the corresponding structures is below industrial limit and therefore, chosen materials are to be characterized and evaluated electrochemically in the next section.

6 Electrochemical characterization

Electrochemical characterization was performed for selected materials to obtain their practical specific capacities, cycleability, performance, and lithium diffusion coefficients over the whole cycling range. Therefore, different methods such as cyclic voltammetry (CV), galvanostatic intermittent titration (GITT), cycling at different C-rates, and *ex situ* measurements were applied. The corresponding active materials were characterized with respect to their differences in terms of precursor, synthesis temperature and composition, and the results were evaluated and compared.

6.1 Methods

6.1.1 General concepts

As discussed earlier, an electrochemical cell consists of an anode and a cathode, which are both placed into an electrolyte solution. During discharging, the electrochemically active material is oxidized at the anode, while the cathode active material is reduced. The electrode naming convention is defined for the discharge case, disregarding the actual flow of the current, meaning the anode is the negative electrode while the cathode is the positive electrode.

Electrical charge Q is defined by the area under the current-time curve:

$$Q = \int_0^t i \, d\tau \quad (6.1)$$

Where i is the current and t the time the current is flowing.

If the current remains constant over time, the equation simplifies to

$$Q = I \cdot t \quad (6.2)$$

The relation between electrical charge and the amount of electrochemically active substance is described by Faraday's law via [106]:

$$Q = n \cdot z \cdot F \quad (6.3)$$

where n is the amount of substance in moles, z the number of electrons participating in the reaction, and F the Faraday's constant, which corresponds to the amount of charge for one mole of electrons (96485.33 As mol⁻¹).

The equilibrium potential of a lithium-ion battery cell is defined by the chemical potential difference for lithium in the anode and cathode:

$$V = -\frac{\mu_{Li}^c - \mu_{Li}^a}{z \cdot F} \quad (6.4)$$

Here μ_{Li} represents the chemical potential of lithium in the anode/cathode respectively. In this work, half cell measurements were performed, where lithium metal was used as anode material. In this case, the anode potential is taken as standard chemical potential for metallic lithium and all potentials can be referenced against this.

The equation therefore simplifies to

$$V = -\frac{\mu_{Li}^c}{z} \quad [in \text{ eV}] \quad (6.5)$$

as the Faraday's constant equals 1 ($F = 1$) if the electrochemical potential is expressed in eV [107]. The number of electrons, z , is related to the amount of lithium, x , deintercalated from the cathode as in $\text{Li}_{1-x}\text{Ni}_{1/3}\text{Mn}_{1/3}\text{Co}_{1/3}\text{O}_2$.

The voltage therefore depends on the state of charge (SOC) of the electrodes or, in this particular case, when lithium metal acts as anode material, solely on the lithiation stage of the cathode.

6.1.2 Slurry and half cell preparation

Slurries were prepared from the corresponding active material (NMC), carbon black as conductive agent (Super P, Timcal) and polyvinylidene fluoride (PVDF, MTI) as binder in a ratio of 80:10:10 (NMC:CB:PVDF).

PVDF was first dissolved in N-Methyl-2pyrrolidone (NMP, Sigma Aldrich, >99.5%) using a magnetic stirrer for a minimum of 2 h. Meanwhile, NMC and carbon black were mixed in a zirconia planetary ball mill at 250 rpm for 3 h. The mixture was added to the PVDF solution and the slurry was further stirred at 600 rpm for 6 h. After that, the slurry was cast using the Doctor-Blade method onto an aluminium foil (15 μm , MTI) with a wet thickness of 120 μm . The coated electrode sheets were first dried at room temperature for 2 h and then heated at 120 $^{\circ}\text{C}$ overnight to remove any residual solvent.

The sheets were further hot-pressed until a final thickness of 40 μm , including the current collector, was achieved. Round electrodes of different diameters between 15 and 18 mm diameter, depending on the performed measurements, were cut from the sheets and transferred into a vacuum oven (Büchi, Glass Oven B-585), where they were again heated at 120 $^{\circ}\text{C}$ under vacuum over night before being transferred into the glovebox.

Test cells of different types (coin cell type 2032 and El Cell test cells) were assembled in the argon-filled glovebox (MBraun, oxygen and water content <0.1 ppm). In all cases, a 1:1 (w/w) mixture of ethylene carbonate:dimethyl carbonate solvents using 1 M LiPF_6 as conducting salt (referred to as LP30, BASF, battery grade) was used as electrolyte.

All electrochemical measurements were performed versus lithium metal as counter electrode (MTI, battery grade) at room temperature (25 $^{\circ}\text{C}$). The cells were allowed to rest for 6 h before the start of the measurement. At this point it has to be mentioned that no slurry or electrode preparation or formulation adjustment or improvement was performed. The procedure of electrode preparation was chosen as standard procedure for screening between the corresponding synthesized materials and not varied for different NMC samples.

6.1.3 Cyclic voltammetry (CV)

CV measurements were performed in El cell [108] test cells (see Figure 6.1), using a Biologic SP-300 potentiostat between 3 and 4.2 V.

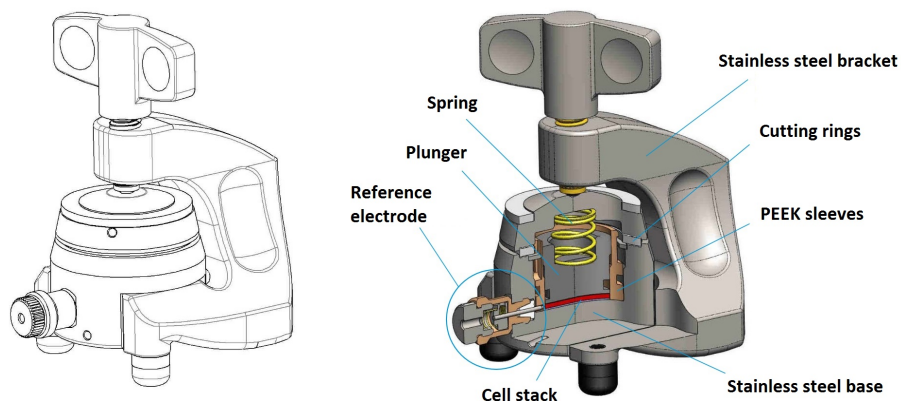


Figure 6.1: Illustration of the test cells for CV measurements, El Cell GmbH.

The real specific capacities of the active materials were derived by Faraday's law [106] via integration of the corresponding charge/discharge curve (in mAmps) over time (in hours), divided by the active mass as presented in Figure 6.2.

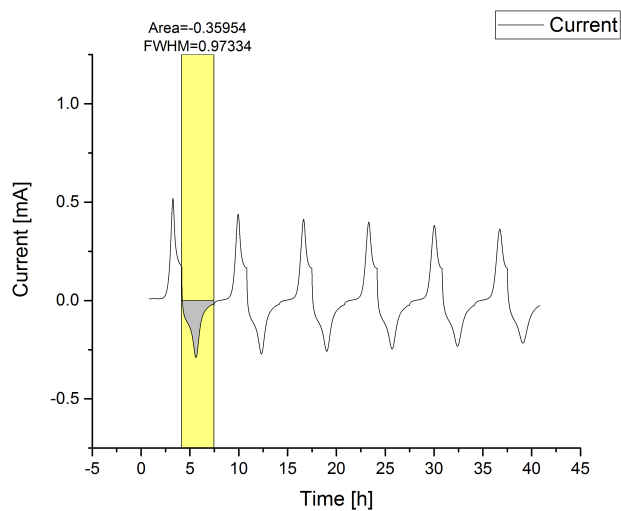


Figure 6.2: Example for determination of real specific discharge capacity of NMC.

6.1.4 Cycling tests

Long term cycling in the potential range of 3 - 4.2 V was performed at different C-rates (0.1 C and 0.2 C) as well as rate capability tests. For rate capability tests, the C-Rate was increased every 20th cycle from 0.1 C up to 5 C in four steps and for the last 20 cycles the C-rate was reduced back to 0.1 C to evaluate the rate capability between the cycles before and after cycling at higher currents.

The theoretical capacity of NMC as derived by Faraday's Law is:

$$C_T = \frac{F \cdot z}{M} = \frac{96485.3399[A \cdot s \cdot mol^{-1}] \cdot 1}{96.40290[g \cdot mol^{-1}] \cdot 3.6} = 278.01532[mAh \cdot g^{-1}] \quad (6.6)$$

For better comparison between different materials, the term C-rate, which is independent of the amount of active material and applied current, is introduced. The C-Rate is defined as the quotient between the charge/discharge current and the capacity of the cell:

$$C = \frac{1}{C_T} [h^{-1}] \quad (6.7)$$

The applied current can therefore be calculated from the mass of the active material in the electrode and the desired C-rate, which implies the duration of the charge/discharge case.

Different parameters can be calculated from the derived capacities of the cycling tests for evaluation of the cells' performance. One key factor is the quotient between charge and discharge capacity, which gives the Coulombic efficiency:

$$C_{eff} = \frac{C_{charge}}{C_{discharge}} [\%] \quad (6.8)$$

Another important factor is the capacity retention, in this work defined as the difference between the corresponding and the mean value of the discharge capacities of the first five cycles:

$$C_{ret} = \frac{5 \cdot C_{discharge_n}}{\sum_{i=1}^5 C_{discharge_i}} [\%] \quad (6.9)$$

6.1.5 Galvanostatic Intermittent Titration Technique (GITT)

The galvanostatic intermittent titration technique (GITT) was first developed and applied by Weppner and Huggins in 1977 to determine the chemical diffusion coefficient in Li_3Sb [109]. It is based on the fact that lithium diffusion inside the electrode obeys Fick's second law and can therefore be obtained by the following equation:

$$D = \frac{4}{\pi} \left(\frac{m_B V_m}{M_B S} \right)^2 \left[\frac{\Delta U_{OCP}}{\tau \left(\frac{dU}{d\sqrt{t}} \right)} \right]^2 \quad \text{for } (t \ll \frac{L^2}{D}) \quad (6.10)$$

Here, τ represents the duration of the pulse, m_B the active mass of the electrode, V_M the molar volume of the active material, M_B the molecular weight, and S the active specific surface area of the electrode. ΔU_{OCP} represents the change of the open cell potential before and after the pulse, while dU is the actual change of the voltage during the pulse, neglecting the IR-drop. The equation is only valid if the time scale is considerably smaller than the length of the electrode L^2 divided by the Diffusion coefficient itself, D .

In GITT measurements, a constant current is applied for a specified time (see Figure 6.3), changing the amount of lithium, x , in the structure from $\text{Li}_x\text{Ni}_{1/3}\text{Mn}_{1/3}\text{Co}_{1/3}\text{O}_2$ to $x \pm \Delta x$, depending on the actual case - charging or discharging of the cell.

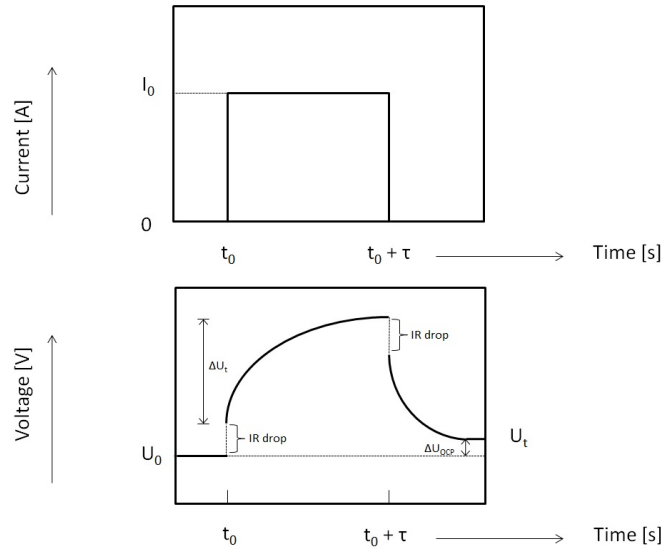


Figure 6.3: Scheme of voltage and current trend during one pulse of the GITT measurement.

It should be pointed out once again that when a positive current is applied as in the charging case, the cathode material is oxidized while lithium ions are deintercalated from the structure. The amount of lithium in the cathode therefore decreases during the pulse in the charging case; and for discharging vice versa. Lithium ions are intercalated into the cathode during the negative current pulse, which refers to the discharging case.

The cell is allowed to relax before and after each pulse for a certain time or until the voltage change is sufficiently small. This way, the open-circuit potential for the actual level of lithiation is recorded and the chemical diffusion coefficient over the whole cycling range can be calculated using the formula presented above.

In this work, GITT measurements were performed to obtain the diffusion coefficient in NMC cathodes over the whole cycling range from 3 to 4.2 V. After two cycles formation in the same range at 0.1 C, current pulses for 600 s at 0.1 C were performed and the relaxation time of the cell after each pulse was set to 2400 s.

If the voltage change during the pulse $\frac{dU}{d\sqrt{t}}$ shows expected linear slope behaviour, the above equation simplifies to:

$$D = \frac{4}{\pi \cdot \tau} \left(\frac{m_B V_m}{M_B S} \right)^2 \left(\frac{\Delta U_{OCP}}{\Delta U_t} \right)^2 \quad (6.11)$$

The chemical diffusion coefficient over the whole cycling range as well as the open-circuit potential were obtained and calculated accordingly.

6.1.6 *Ex Situ* X-Ray Diffraction Analysis

Ex situ XRD patterns were recorded at different stages of lithiation to evaluate structural changes during cycling. Therefore, CV measurements were performed using El Cell test cells and a Maccor Series 4000 with a scan rate of 0.1 mV s^{-1} up to 4.5 V. The measurements were stopped at different stages of lithiation and then the cell was allowed to relax for 30 minutes before continuing the scan at $50 \mu\text{V s}^{-1}$.

Cells were assembled and disassembled under inert atmosphere in an argon-filled glovebox (MBraun, oxygen and water content $<0.1 \text{ ppm}$). After disassembly, cathodes were washed with dimethyl carbonate (BASF, battery grade) to remove residual lithium salts. The dried cathodes were sealed in a specially adapted coin cell covered with Mylar film to prevent air exposure during x-ray measurements (see Figure 6.4).



Figure 6.4: Specially adapted coin cells; the top was covered with Mylar foil.

X-ray diffraction patterns were recorded as already described and Rietveld refinement was performed accordingly, using GSAS with the EXPGUI interface. Due to the complexity of the refinement of cathodes, reference patterns of the different included materials were recorded.

The structure of the corresponding NMC powder was used as a starting model for further refinement. The lithium content in the cathodes was calculated from the derived capacity during charging/discharging of the cell and included into the model.

6.2 Results and Discussion

6.2.1 Symmetric NMC

Synthesized NMC samples were characterized electrochemically to determine their stability, cycleability and structural changes during cycling. Symmetric NMC samples calcined at lower temperatures showed no or little electrochemical activity and are therefore not presented here.

Reversibility of redox reactions

Figure 6.5 shows the typical shape of cyclic voltammograms of NMC cathodes as observed for all presented samples.

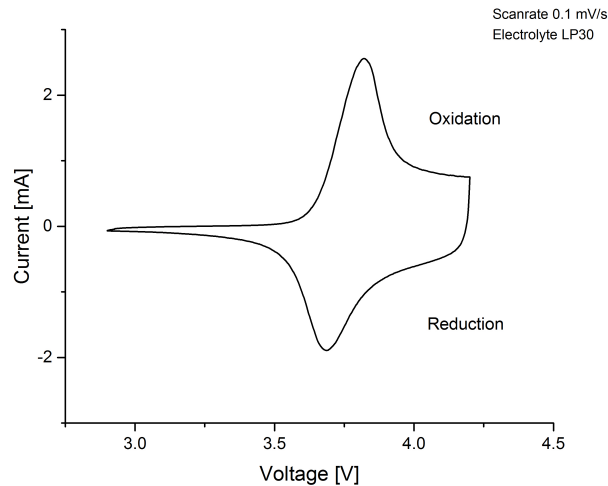


Figure 6.5: Cyclic voltammogram of NMC.

Cyclic voltammetric (CV) measurements of the presented NMC cathodes showed a reversible reaction with an oxidation peak at around 3.8 V and a reduction peak at round 3.6 V for all samples, which correspond to $\text{Ni}^{2+/4+}$ redox reactions. The small potential difference (polarization) of 200 mV between the anodic and cathodic peak indicates good reversibility of lithium intercalation into the structure. The absence of a peak at 3 V reveals that little or no trivalent manganese is present in the cathode active material [110]. As already mentioned, manganese is supposed to be electrochemically inactive in Mn^{4+} oxidation state within the structure for stabilization [111].

Open-circuit voltage over state of charge (OCV over SOC)

Figure 6.6 shows the open-circuit voltage as well as the calculated incremental capacity evolution over state of charge during delithiation. The open-circuit voltage shows the typical plateau region of NMC cathodes in low characteristic between 3.7 and 4.0 V. There is no phase transition or transformation to be expected in this region, which is the cycling range usually applied for commercial lithium-ion batteries. To determine little changes which are not observed straight-forward from the OCV curve, incremental capacity analysis was performed by visualization of identifiable $\Delta Q/\Delta V$ peaks. There is one main peak present at 3.8 V which is used as a reference for state-of-health (SOH) determination in corresponding battery management systems. This peak is characteristic for layered oxide cathode materials and broadens after several cycles due to active material losses [112].

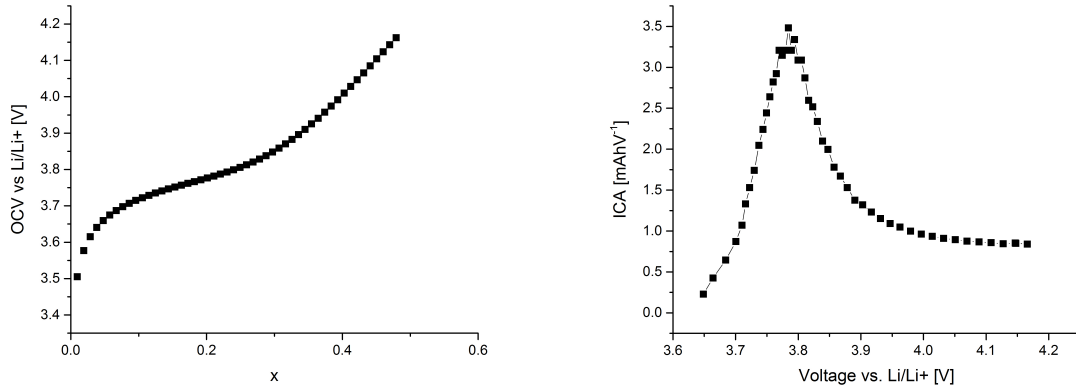


Figure 6.6: Open-circuit voltage and incremental capacity evolution of $\text{Li}_{1-x}\text{Ni}_{1/3}\text{Mn}_{1/3}\text{Co}_{1/3}\text{O}_2$ during delithiation (charging).

One can see that only about half of the lithium is extracted during the GITT experiment. This indicates that the relaxation time, which was fixed to 2400 s, was too low at the lower voltage region after the titration steps. Therefore, also the plateau region shows less specificity than usually observed. One may conclude that GITT measurements generally should not be performed below the open-circuit voltage of the corresponding electrode materials. During relaxation of the battery cell after each titration step, some lithium ions diffuse back into the host structure - especially at the edges of the applied voltage window. Overall, the measured OCV curve shows the typical plateau shape as expected, which was also obtained in a similar manner during cycling experiments.

Diffusion coefficient

The diffusion coefficients, as determined from galvanostatic intermittent titration technique (GITT) are presented in logarithmic scale in Figure 6.7.

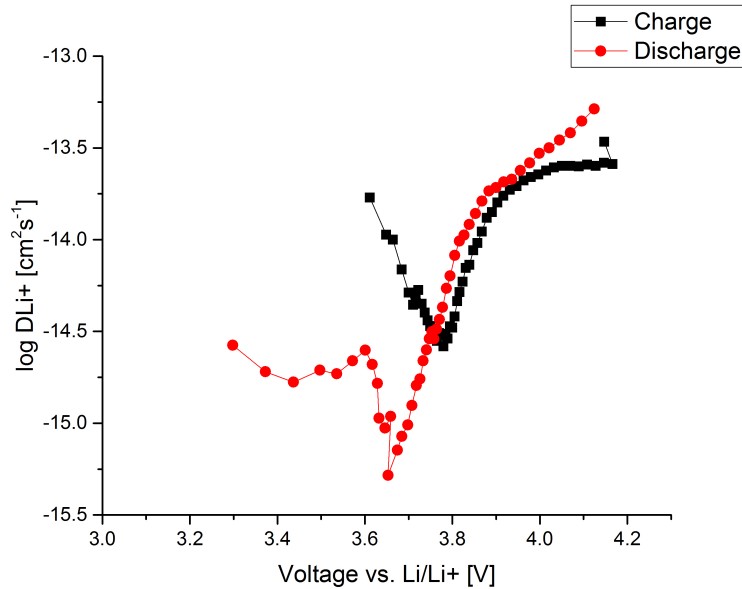


Figure 6.7: Diffusion coefficient of lithium ions in NMC111 for charging/discharging from 3.2 V to 4.2 V.

There are obviously significant differences between the charging and discharging case of the half cell measurements. As already mentioned, the lithium is deintercalated during the charging process and intercalated during discharging. In this case, the charging process, meaning the deintercalation of lithium ions from the cathode host structure, is the favored process up to 3.8 V, where it has its minimum.

At higher voltages, the values for lithium diffusion are closer to each other, but generally lithium ion diffusion is favored for intercalation rather than deintercalation. The plateau region of NMC at around 3.8 V is well-reflected by the data of the OCV over stage of lithiation. The overall trend shows commercial limitations, where NMC battery cells are usually cycled around the 80% state-of-charge region, which corresponds to the maximum operation voltage window of 3.6 - 4.0 V.

Absolute values for lithium diffusion coefficients are always questionable and should be taken with a grain of salt.

A reason for this is the influence of one parameter, more precisely the reaction surface area of the electrode, which is incorporated into the calculation (see Equation 6.11). This value is not directly accessible for porous electrodes and therefore must be estimated and forms an unknown scaling factor. In this work, the active reaction surface area is assumed to be 80% of the incorporated NMC material as determined from gas adsorption measurements.

In literature, one can find huge differences in absolute values for diffusion coefficients of NMC, ranging from around $10^{-10}\text{cm}^2\text{s}^{-1}$ as derived from CV measurements (for example [113] or [114]), EIS (for example [111]) to as from GITT measurements in a similar way as presented with a range of $10^{-19}\text{cm}^2\text{s}^{-1}$ [115]. This is caused by the estimation of the surface area in these calculations as already discussed.

Nevertheless, the overall tendencies of the diffusion coefficients for intercalation and deintercalation case are not influenced as the reaction area is solely incorporated as a linear parameter.

Structural changes during cycling

Figure 6.8 shows recorded XRD reference patterns of the incorporated materials compared to an uncycled cathode pattern at the bottom.

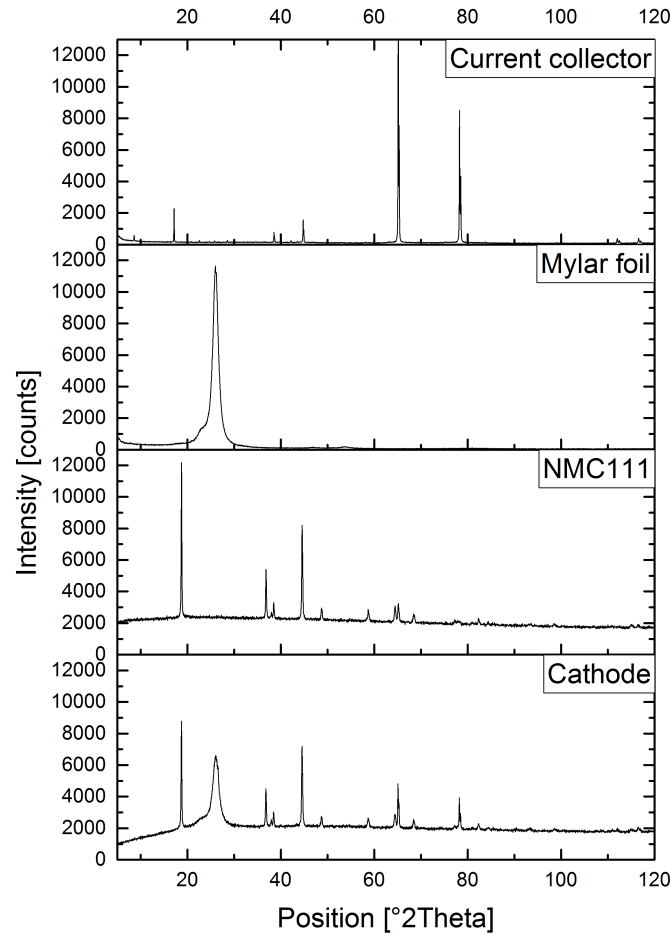


Figure 6.8: Reference pattern of different cathode and sealing compounds.

It can be clearly seen that the aluminum current collector peaks are strongly overlapping with those from the NMC phase, especially at around 65° and 78°. The Mylar foil shows one main peak between 20-30°, which was subtracted prior to the Rietveld refinement. The XRD pattern of an uncycled cathode before and after the Mylar subtraction is presented in Figure 6.9.

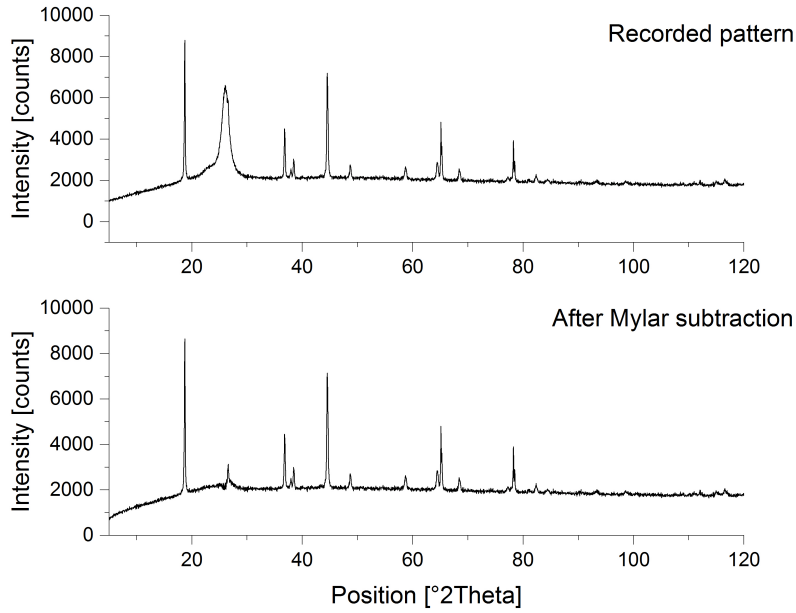


Figure 6.9: XRD pattern of an uncycled cathode before (above) and after (below) the Mylar subtraction.

After the subtraction, a sharp peak, identified as belonging to an additional graphite phase, was observed. Graphite 2H was therefore additionally refined as a second phase for the NMC111 cathodes. The reference pattern of the aluminum current collector was not subtracted (due to strong overlap and sharp peaks as well as height differences), but refined first as single aluminum phase using spherical harmonics and preferred orientation.

The fitted data was included into the model as a third phase, but the parameters were fixed during the refinement (except for height shift) due to the strong overlapping regions with the NMC phase.

The multiphase refinement including all three phases (aluminum current collector, graphite 2H and NMC) showed good reliability although it did not converged in every case. Due to relaxation of the battery cell shortly after stopping the measurement and during disassembly, the calculated lithium content value might differ slightly from reality.

Figure 6.10 shows the unit cell parameter variation with the calculated lithium content.

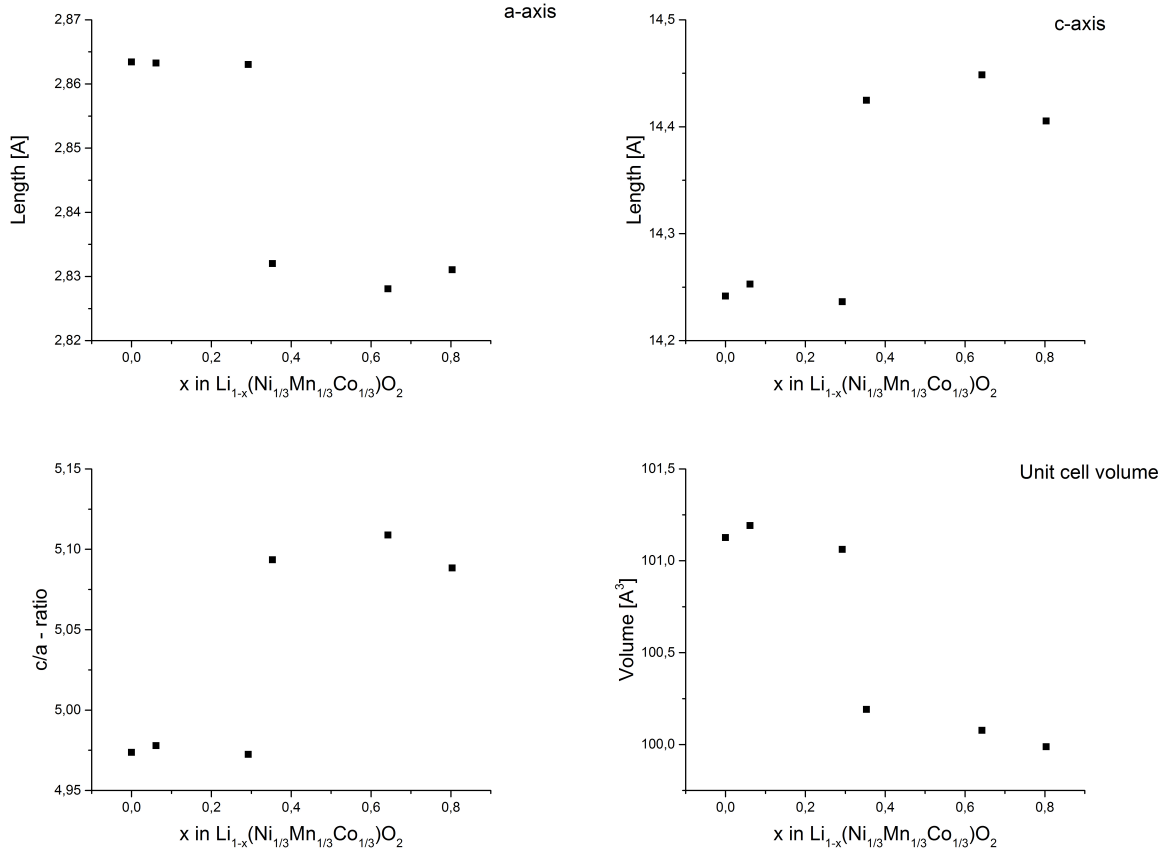


Figure 6.10: Unit cell parameters trend during charging/discharging.

It can be seen that the a-axis (representing the intraslab distance) decreases with decreasing lithium content. This behaviour can be related to the oxidation of nickel from 2+ to 4+, especially for a lithium content of ≥ 0.4 moles. Showing an opposite trend, the c-axis (representing the interslab distance) increases with increasing lithium content, which can be explained by electrical repulsion between transition metal oxide layers [29]. The unit cell volume is dominated by the a-axis, showing a decreasing trend with lower lithium content. The overall unit cell volume changes only slightly by around 1.2 %.

At $x \leq 0.4$ in the formula $\text{Li}_x\text{Ni}_{1/3}\text{Mn}_{1/3}\text{Co}_{1/3}\text{O}_2$, all nickel ions are in 4+ oxidation state and the oxidation of cobalt from 3+ to 4+ is taking place. The minor changes of the unit cell in this region might be explained by the minor differences of the ionic radii of the cobalt ions compared to the nickel ions. The average ionic radius of the transition metals was calculated, assuming nickel oxidation from 2+ to 3+ at $2/3 \leq x \leq 1$; further nickel oxidation from 3+ to 4+ at $1/3 \leq x \leq 2/3$ and cobalt oxidation from 3+ to 4+ at $0 \leq x \leq 1/3$. Manganese was assumed in 4+ oxidation state in all regions.

Table 6.1 shows the ionic radii from the nickel, manganese and cobalt ions in their possible oxidation states during cycling (taken from[116]).

Table 6.1: Ionic radii of the corresponding transition metal ions.

Ion	Radius [\AA]
Ni(II)	0.69
Ni(III)	0.56
Ni(IV)	0.48
Co(III)	0.55
Co(IV)	0.53
Mn(IV)	0.53

The average ionic radius was calculated regarding the composition of the transition metals and NMC and the corresponding oxidation state of the ions. The variation of this value with lithium content is presented in Figure 6.11.

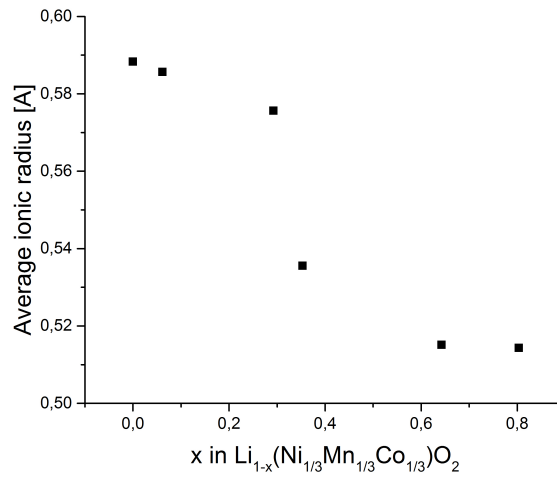


Figure 6.11: Calculated average ionic radius with lithium content assuming nickel oxidation followed by cobalt oxidation.

The trend of the calculated average ionic radius is similar to the intraslab distance variation by lithium content.

There is obviously a good correlation between the unit cell parameter a and the average ionic radius, confirming the explanation above regarding the redox reactions which are supposed to contribute to the overall cell reaction.

Real specific capacities

The specific discharge capacities, as calculated from the third cycles of the corresponding CVs, are presented in Figure 6.12.

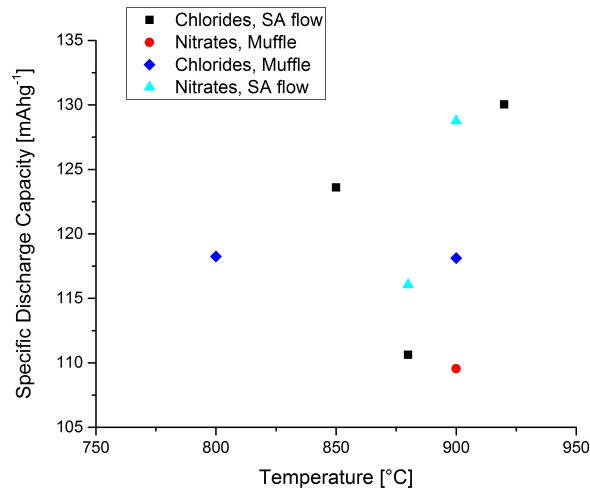


Figure 6.12: Specific discharge capacities as derived from CV measurements for different synthesis of NMC111.

The overall trend of the specific capacities of the materials reflects the unit cell parameter changes as determined from Rietveld fit of recorded XRD patterns (see Section 5). There is a slight tendency of increasing specific discharge capacities with increasing synthesis temperature for syntheses from the same precursors prepared under the same calcination conditions.

Obviously some structural change or different behaviour occurs at 900 °C, which was also reflected by the crystal structure determination and particle size distribution of these NMC samples. One explanation is the serious issue of lithia loss, as already mentioned in the prior section.

Idris et al. reported that non-symmetric NMC samples calcined under absence of oxygen at higher temperatures (950 °C) showed Li₂O impurity phases [117]. For all samples which were prepared under nitrogen atmosphere they concluded that they tend to lose oxygen, which was reflected by the unit cell parameter variation in a similar characteristic as in the NMC samples presented in this work.

There is no correlation between the specific discharge capacities and the amount of cation mixing in the presented symmetric NMC samples. This can be explained by two causes.

First, the amount of cation mixing as determined by Rietveld fit in the presented materials does not exceed 6%, which is an acceptable value. Sun et al. recently even published that cathodes with a certain amount of cation mixing showed better performance compared to those with a lower cation mixing of nickel occupying lithium sites [118]. It was assumed that some cation mixing of cation mixing contributes well to structural stability of NMC.

Second, the specific discharge capacities are determined from the third cycles of fresh electrodes and the influence of cation mixing becomes manifest only later within long term cycling, which will be evaluated in the next section.

Chloride-prepared samples without synthetic air flow during calcination show straight line behaviour regarding synthesis temperature. This correlates well with the amount of impurities in the structures, which remains constant with increasing calcination temperature as determined from ICP analysis. In contrast, when synthetic air flow is applied during the calcination process, the specific capacities show a minima at around 900 °C for both chloride and nitrate prepared NMC samples. This again is reflected by the unit cell parameter variation, which again can be related to a cation mixing of loss of lithia at higher temperatures and a cation mixing of reduction of the transition metal cations at 950 °C.

NMC samples prepared in the muffle oven under ambient conditions show lower specific capacities compared to those prepared under constant flow of synthetic air. The amount of oxygen present during the calcination step seems crucial for the electrochemical performance of synthesized NMC samples. To prove that this assumption is correct, samples prepared at higher temperatures (900 °C) for both precursors, nitrates and chlorides, are compared in the next section regarding their calcination atmospheric conditions.

Cycling performance

Figure 6.13 shows the specific capacities, efficiency and capacity retention of NMC111 at 0.1C, prepared under constant synthetic air flow.

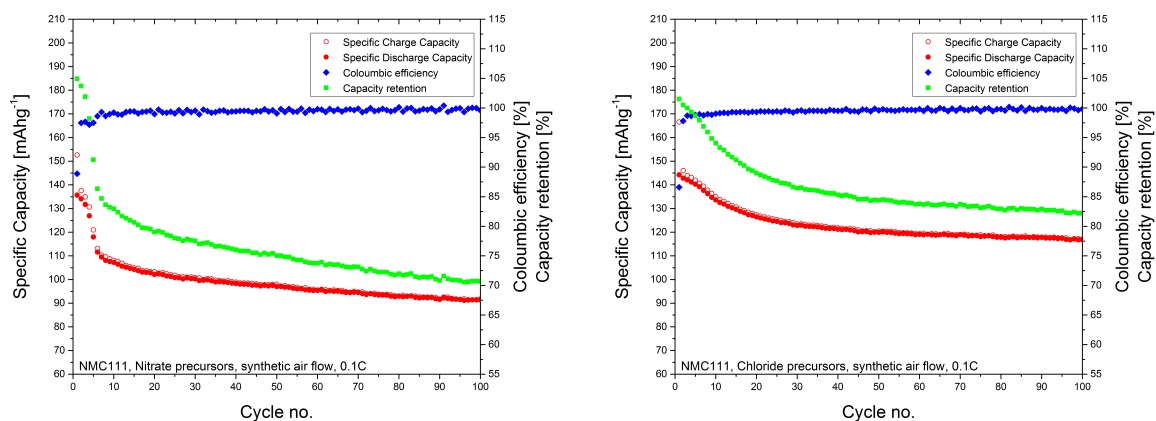


Figure 6.13: Cycling behaviour at 0.1C of symmetric NMC using nitrates (111 N SA, left) and chlorides (111 C SA, right) calcined under synthetic air flow.

The same parameters of NMC electrodes prepared in the muffle oven are presented in Figure 6.14.

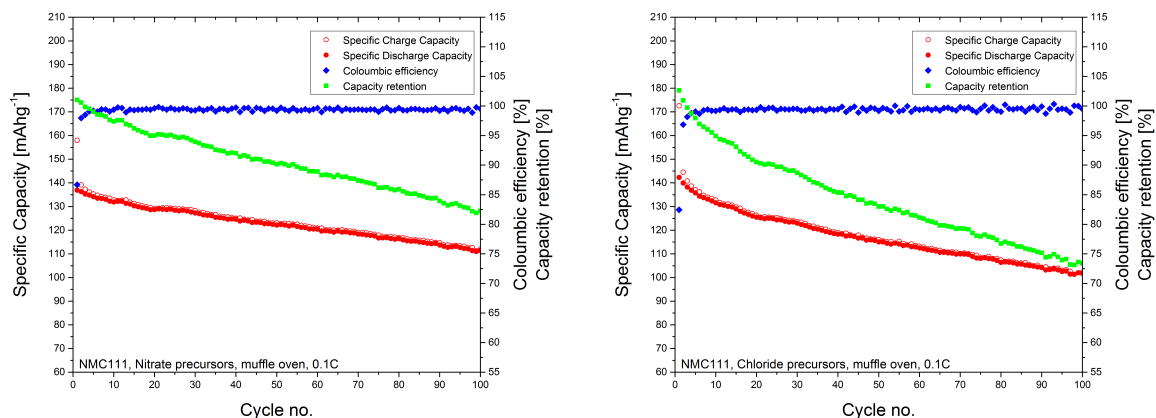


Figure 6.14: Cycling behaviour at 0.1C of symmetric NMC using nitrates (111 N MO, left) and chlorides (111 C MO, right), calcined in the muffle oven.

The specific capacities of chloride-prepared samples under constant air flow are significantly higher than of nitrate-prepared NMC cathodes. The Coloumbic efficiency as well as the capacity retention from the corresponding first cycles show more stable behaviour compared to those synthesized from nitrate precursors.

In contrast, the nitrate-prepared samples calcined in the muffle oven show slightly higher specific capacities compared to chloride ones. However, the differences between the chloride and nitrate precursors seem to be less pronounced under these experimental conditions. The availability of oxygen during the synthesis of NMC is obviously more important when nitrate precursors are used, while in the case of chloride it is less significant.

Both chloride and nitrate-prepared symmetric NMC cathode materials showed better stability over the cycling range when constant air flow was applied during synthesis. On contrary, samples prepared in the muffle oven show monotonic decreasing capacities with an increasing number of cycles for both types of precursors.

Little work has been published to evaluate the importance of the atmospheric synthesis conditions (in particular the effect of oxygen content) during the heating process of NMC cathode active materials. Some work has been performed for non-symmetric NMC compounds which were synthesized using sol-gel [119], mixed-acetate [117] and coprecipitation routes [120] under different atmospheres. They revealed that controlling the oxygen content during synthesis is very important for optimizing electrochemical performance. Additionally to this, the cation mixing of cation mixing in their samples was significantly reduced in oxygen-rich atmospheres.

This is in agreement with the presented results obtained on symmetric NMC synthesized via coprecipitation route. When samples are prepared in the muffle oven, even though in air atmosphere, the amount of oxygen is much less compared to NMC prepared under synthetic air flow in the tube furnace. This can be found especially in the case of using nitrate precursors, which tend to lead to a higher cation mixing of impurities in the intermediate NMC product before the calcination process. They also tend to form non-volatile lithia which remains in the structure and leads to capacity decrease, which was not reported for syntheses under oxygen-rich atmosphere.

Samples obtained from chloride precursors seem to exhibit slightly higher discharge capacities in the first few cycles. They suffer however from a more pronounced capacity fading, in comparison to the nitrate ones.

The latter have therefore a better capacity retention. The highest specific capacities at 0.1C after 100 cycles were obtained for chloride-prepared samples calcined under synthetic air flow. The NMC cathode exhibits a specific discharge capacity of 116.80 mAhg^{-1} and a Coloumbic efficiency of 99.83 % after 100 cycles at 0.1 C rate.

Figure 6.15 and Figure 6.16 present the cycling behaviour of the NMC111 samples at 0.2 C rate.

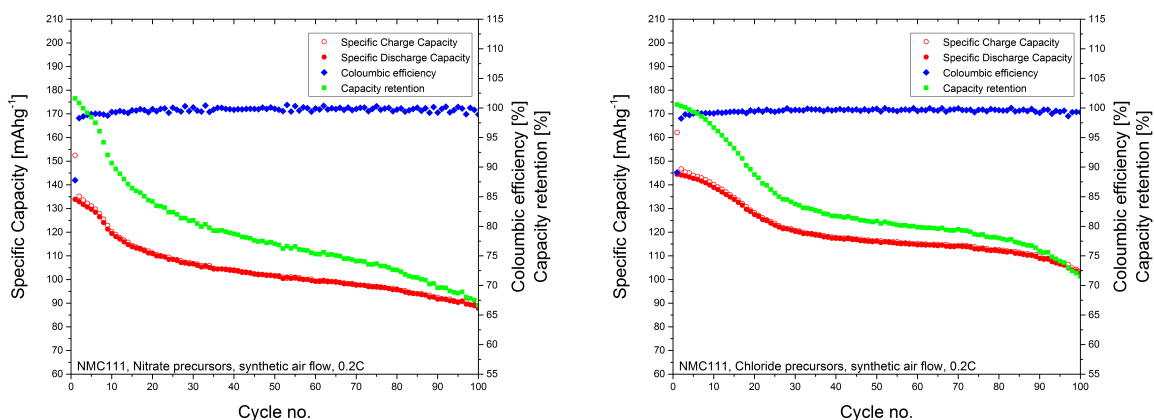


Figure 6.15: Cycling behaviour at 0.2C of symmetric NMC using nitrates (111 N SA, left) and chlorides (111 C SA, right) calcined under synthetic air flow.

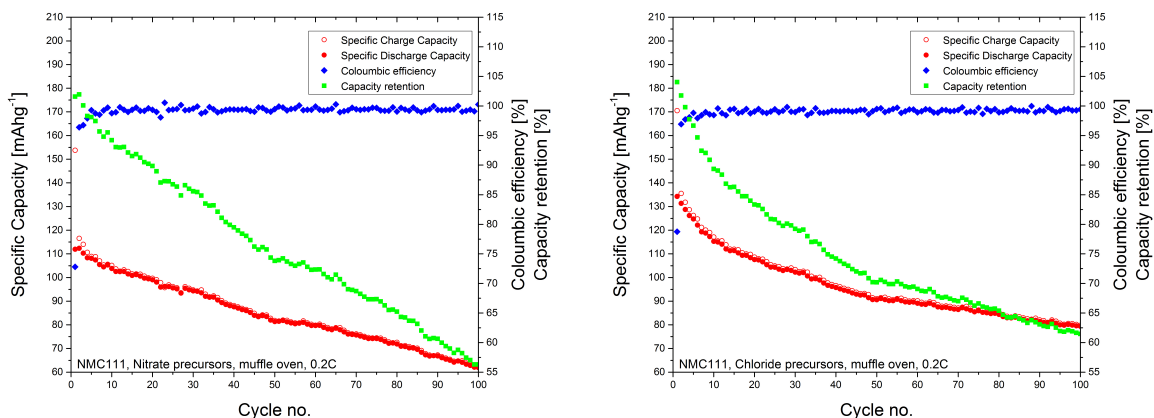


Figure 6.16: Cycling behaviour at 0.2C of symmetric NMC using nitrates (111 N MO, left) and chlorides (111 C MO, right) calcined in the muffle oven.

For all presented NMC111 samples, the cycling behaviour show similar trends for both applied C-rates but more pronounced at 0.2 C. The only difference was obtained regarding nitrate-prepared samples in the muffle oven, which show higher specific capacities than chloride ones at 0.1 C and vice versa at 0.2 C. Nevertheless, the differences between the two types of precursor prepared in the muffle oven are not significant at the lower C-rate and become manifest at 0.2 C.

Nitrate-prepared samples under synthetic air flow show similar behaviour for both applied C-rates. The specific capacity is not significantly lower at 0.2 C compared to 0.1 C up to 100 cycles. However, the fading in the discharge capacity at 0.2 C seems to be more pronounced in comparison to 0.1 C.

All samples prepared under constant air flow exhibited a steep capacity decrease in the first 20 to 25 cycles. In the following cycles, the materials seem to stabilize and thus the capacity fading becomes less significant. This corresponds to the formation of a surface film at the cathode, due to reactions of the layered oxide with the electrolyte components - both salt and solvents [121] [122] [123].

Qian et al. showed in symmetric NMC half and full cells that strong capacity decays within the first cycles can be directly linked to CEI (cathode electrolyte interphase) or SEI formation. After the first cycles, the cells stabilize and show, due to the protective layer at the interphases, more stable behaviour [124]. According to the presented data, best visible for those samples prepared under synthetic air flow, the side film formation lasts for about 10 to 20 cycles.

The monotonic decreasing tendency of symmetric NMC cathodes prepared in the muffle oven can be well explained by formation of non-volatile lithia in case of oxygen deficiency and therefore, some cation mixing or reduction of the transition metals. Manganese, as already discussed, is supposed to be inactive in 4+ oxidation state. The reduced 3+ species disproportionates into 2+ and 4+. In a full cell, the Mn^{2+} ions can migrate through the separator to the anode side and "poison" the SEI layer. In this case, the bivalent Manganese ion is dissolved in the electrolyte which leads to irreversible loss of electrode active material and constant capacity decrease. This statement is supported well by the monotonic decreasing specific capacities with cycle number for those samples prepared in the muffle oven.

As expected, all measured NMC samples exhibited lower capacity values when increasing the C-rate. Lower capacity values at higher C-rates are usually observed as a consequence of limiting transport and kinetic processes, as studied for example by Wu et al. [125]. Rate capability tests are performed to check how significant the ageing is by cycling back at lower C-rates, which will be presented in the following section.

The highest specific capacities at 0.2 C for 100 cycles were obtained for chloride-prepared samples calcined under synthetic air flow. The NMC cathode exhibits specific discharge capacity of 102.76 mAhg^{-1} and Coloumbic efficiency of 99.28 % in the 100th cycle at 0.2 C rate.

Rate capability

The results of the rate capability tests of symmetric NMC from 0.1 C up to 5 C and back are presented in Table 6.2. The average discharge capacity refers to the mean value of the first 20 cycles at 0.1 C.

Table 6.2: Results from rate capability tests of NMC111 using nitrate (N) and chloride (C) precursors.

Sample	Precursor	Calcination condition	Average discharge capacity [mAhg^{-1}]	Discharge capacity last cycle [mAhg^{-1}]
111 C SA	Chlorides	Air flow	132.86	120.87
111 N SA	Nitrates	Air flow	125.87	99.29
111 C MO	Chlorides	Muffle oven	130.78	117.99
111 N MO	Nitrates	Muffle oven	125.03	109.51

All presented samples showed high specific discharge capacities, even when cycling at higher C-rates. Therefore it is assumed that no relevant structural defects or changes occurred during the process.

It must be pointed out here that the presented NMC cathodes are not supposed to be applied for high currents and are no high-power electrode materials. The application of higher currents calls for different electrode design and preparation (smaller particles and thinner electrodes) than applied in this work.

Rate capability tests were performed for evaluation of the cathodes' behaviour after high stresses. Nevertheless, the capacities obtained from cycling tests, as presented earlier, are reflected well by the rate capability tests.

Table 6.3 presents the parameters of the best symmetric NMC cathode material regarding electrochemistry and synthesis conditions.

Table 6.3: Parameters of the best NMC111 samples.

Parameter	Value
Sample Name	111 C SA
Precursor	Chlorides
Calcination Condition	Synthetic air flow
Temperature	900 °C
Discharge Capacity at 0.1 C 1 st Cycle	144.24 mAhg ⁻¹
Discharge Capacity at 0.1 C 100 th Cycle	116.80 mAhg ⁻¹
Coloumbic Efficiency at 0.1 C 100 th Cycle	99.83 %
Discharge Capacity at 0.2 C 1 st Cycle	144.47 mAhg ⁻¹
Discharge Capacity at 0.2 C 100 th Cycle	102.76 mAhg ⁻¹
Coloumbic Efficiency at 0.2 C 100 th Cycle	99.28 %

The Coloumbic efficiency for all presented NMC cathodes was very high, even though the first cycles showed slightly lower values, well-explained by the formation of side films at both electrodes, the lithium metal anode and NMC cathode.

6.2.2 Non-symmetric NMC

As the results of symmetric NMC samples (NMC111) revealed that synthetic air flow increases the electrochemical performance and efficiency, all presented NMC532 samples were prepared under these conditions in the tube furnace. The type of the precursor as well as the calcination temperatures were still varied for evaluation.

Real specific capacities

The real specific discharge capacities of NMC532, as determined from the corresponding third cycle of cyclic voltammetric measurements, are presented in Figure 6.17.

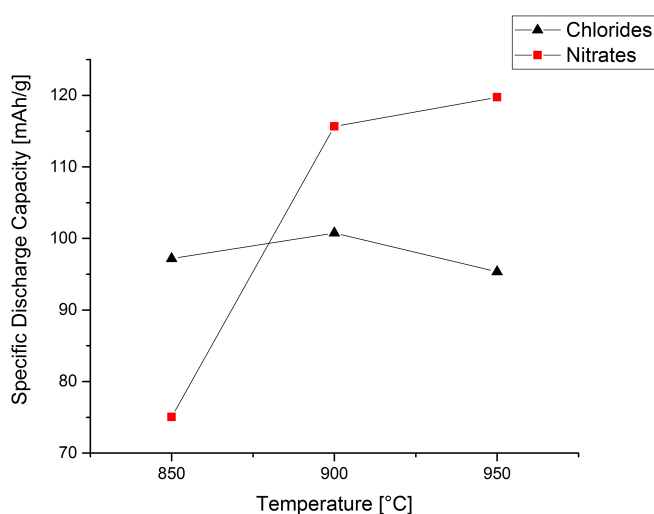


Figure 6.17: Specific discharge capacities of non-symmetric NMC using different precursors and different calcination temperatures.

There is an increasing trend for the specific discharge capacity with increasing synthesis temperature when using nitrate precursors. No obvious tendency can be discerned when chloride precursors are used. This behaviour reflects the amount of impurities, which remains constant for chlorides but, as presented in the physico-chemical section, decreases with calcination temperature if nitrate precursors are used. As already mentioned, the amount of lithium decreases with increasing temperature, which is unfavorable due to the need of using an excess of precursors. At 800 °C, for both precursors, the prepared samples were not electrochemically active, which is caused by their low crystallinity. The highest specific capacity from CV measurements up to 4.2 V was obtained for nitrate-prepared NMC532 at 950 °C, exhibiting 119.74 mAhg⁻¹.

One of the reasons for increasing the amount of nickel in symmetric NMC active material is to enlarge the potential operation window of the cathode, which would lead to a reduction in the number of battery cells needed for automotive applications. Theoretically, the specific capacity is not significantly decreased for this non-symmetric composition and additionally the reduction of cobalt, which is toxic and expensive, is favorable for future compositions.

To evaluate the stability and electrochemical performance at higher cut-off voltages, CV measurements of NMC532 were also performed up to 4.5 V (see Figure 6.18). In this case only nitrate-prepared samples were used, as these showed better electrochemical performance compared to chloride ones.

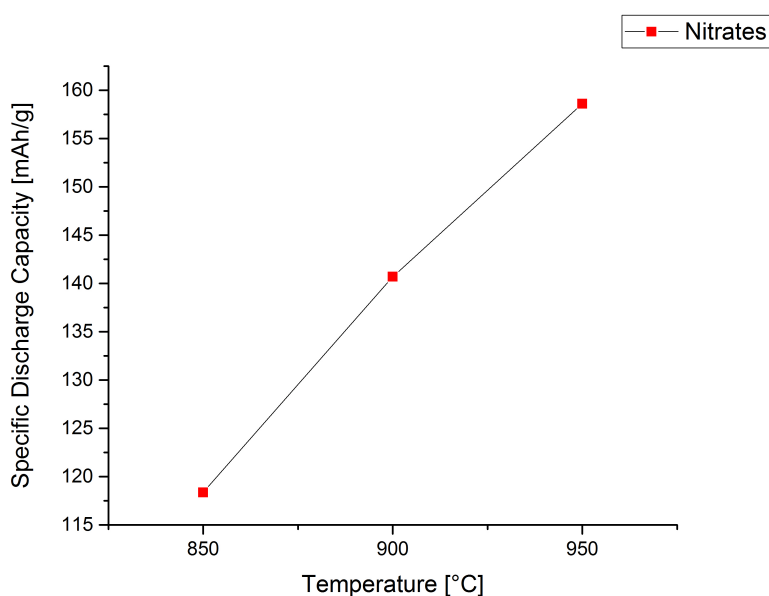


Figure 6.18: Specific discharge capacities of NMC532 using nitrate precursors and different calcination temperatures when cycled to 4.5 V.

The real specific discharge capacity is significantly higher when a higher cut-off voltage of 4.5 V is applied. Similar to those samples cycled up to 4.2 V, the capacities are monotonic increasing with increasing calcination temperature. The highest specific discharge capacity from cyclic voltammetry was obtained at 950 °C, exhibiting 158.62 mAhg^{-1} in the third cycle.

Possible side effects and stability over longer cycling at higher cut-off voltage will be discussed in the next section.

Cycling performance

Cycling tests were performed for all samples, but due to the low electrochemical activity of the other materials only the two higher calcination temperatures for both precursors are presented here. The chloride-prepared samples, which showed lower specific capacities, were additionally tested for comparison with nitrate-prepared samples.

Figure 6.19 and Figure 6.20 present the results of the cycling tests at 0.1 C for both chloride and nitrate-prepared samples at two different temperatures.

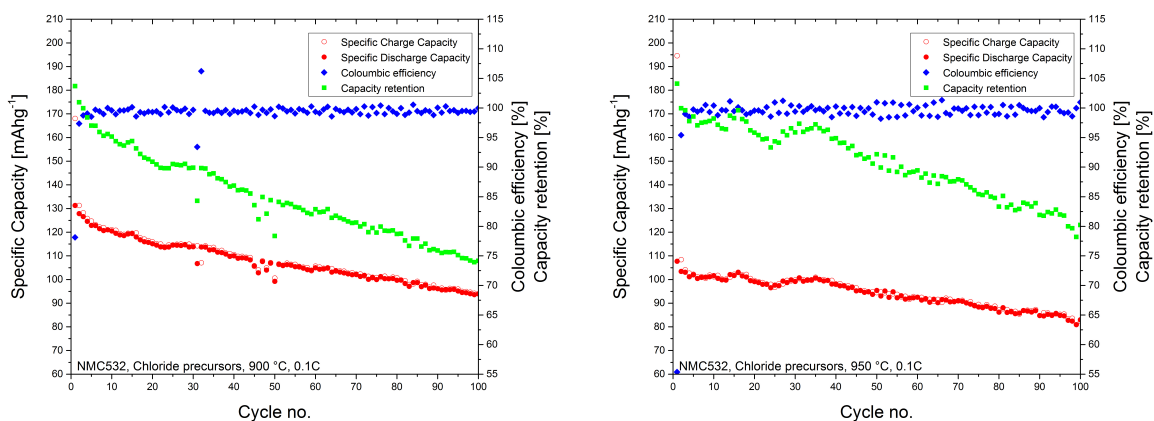


Figure 6.19: Cycling behaviour at 0.1C of NMC532 using chloride precursors at 900 °C (532 C 3, left) and 950 °C (532 C 4, right).

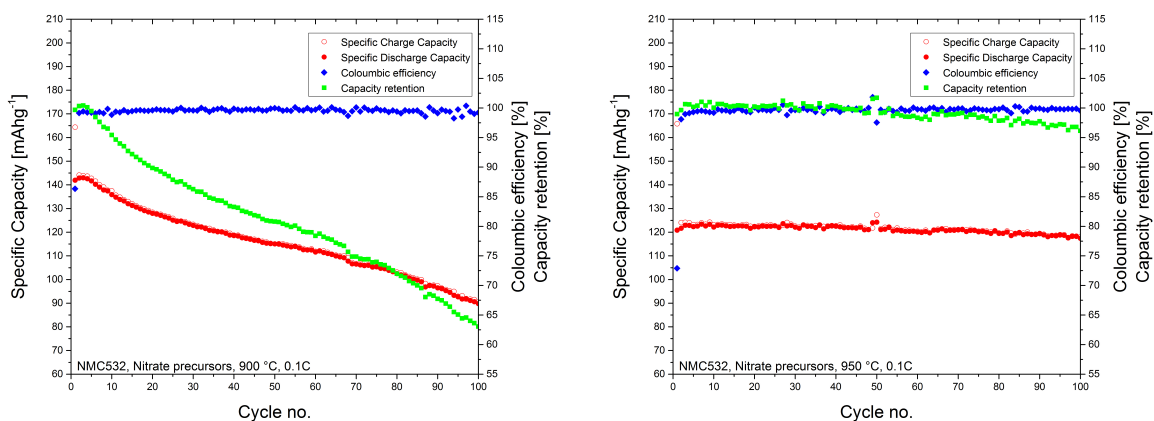


Figure 6.20: Cycling behaviour at 0.1C of NMC532 using nitrate precursors at 900 °C (532 N 3, left) and 950 °C (532 N 4, right).

Figure 6.21 and Figure 6.22 present results of the same samples cycled at 0.2 C rate.

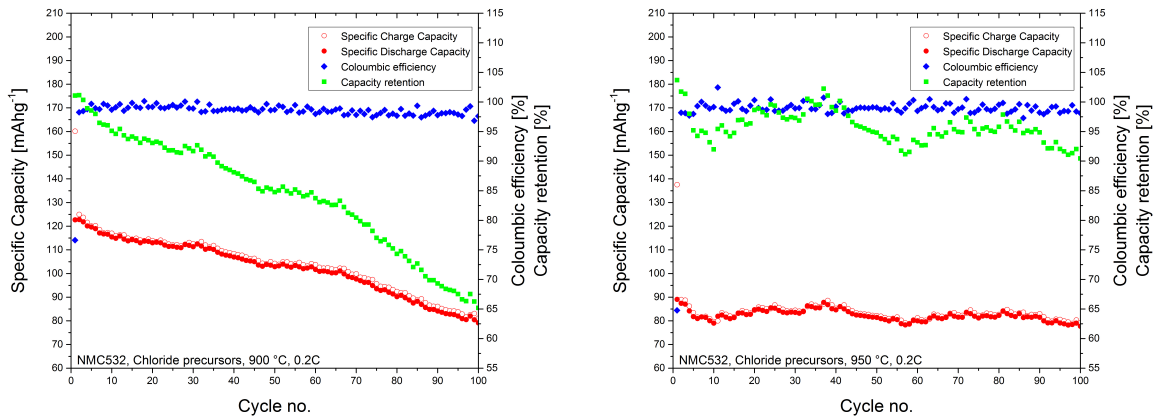


Figure 6.21: Cycling behaviour at 0.2C of NMC532 using chloride precursors at 900 °C (532 C 3, left) and 950 °C (532 C 4, right).

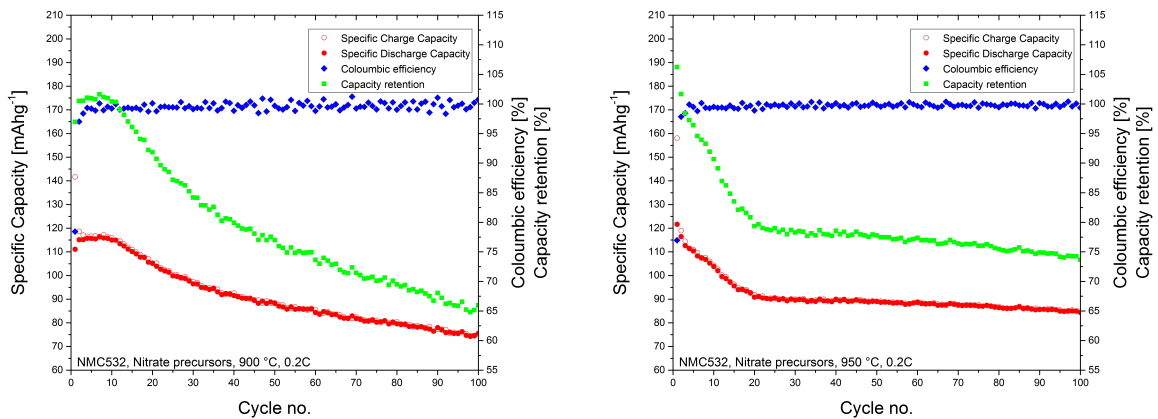


Figure 6.22: Cycling behaviour at 0.2C of NMC532 using nitrate precursors at 900 °C (532 N 3, left) and 950 °C (532 N 4, right).

In contrast to symmetric NMC cathodes, the non-symmetric composition nitrate-prepared samples showed slightly higher specific capacities and significantly higher efficiency than the chloride ones at both applied C-rates, especially those samples prepared at 950 °C. At 0.2 C rate, the monotonic decreasing trend up to the 20th cycle, followed by stabilization of the capacities during the subsequent cycles, is shown with strong characteristic for nitrate-prepared NMC cathodes in a similar manner as observed for NMC111.

Again, the reason for that might be some side reaction with the electrolyte and further cathode-electrolyte interface formation. Another reason for initial capacity loss is the SEI film formation at the anode (lithium metal in this half cell configuration). This causes some irreversible capacity loss, especially at the first cycles, after stabilization of the interface layer. Therefore, the first cycles are usually called “formation cycles” as the capacity is influenced by this side film formation. In commercial applications, additives decompose and form a stable film at the surface of the anode.

All non-symmetric NMC cathodes prepared at 950 °C showed more stable behaviour during cycling than those samples calcined at 900 °C, which showed a monotonic decreasing trend of their specific capacities over all cycles.

For chloride-prepared samples, the specific capacities were significantly lower for NMC532 calcined at 900 °C than for those which were synthesized at 950 °C. As revealed by ICP analysis, the amount of lithium within the structure decreases with increasing synthesis temperature, as already presented in the physico-chemical characterization section (see 5). This correlates well with the decrease in terms of capacity at higher temperatures and was not observed for nitrate-prepared NMC532 samples. Therefore, nitrate-prepared samples showed more stable behaviour and the highest specific capacity was obtained for those NMC samples calcined at 950 °C.

The lower cycle stability of chloride-prepared samples is explained well by the formation of oxy- or hydroxychlorides, which are insoluble and could not be removed during the washing step of the synthesis. As this behaviour was not observed for symmetric NMC, it would appear possible that the increasing amount of nickel in this composition is responsible.

Thermal decomposition experiments of nickel chlorides revealed that insoluble intermediate products are formed, especially at lower temperatures, identified as Ni(OH)Cl and Ni₂Cl(OH)₃ at around 600 °C [126]. These phases present in the powders, lead to lower capacities and poor cycleability for high-nickel NMC compounds prepared from chloride precursors.

To substantiate this, thermogravimetric analysis of the nickel chloride precursor was performed (see Figure 6.23).

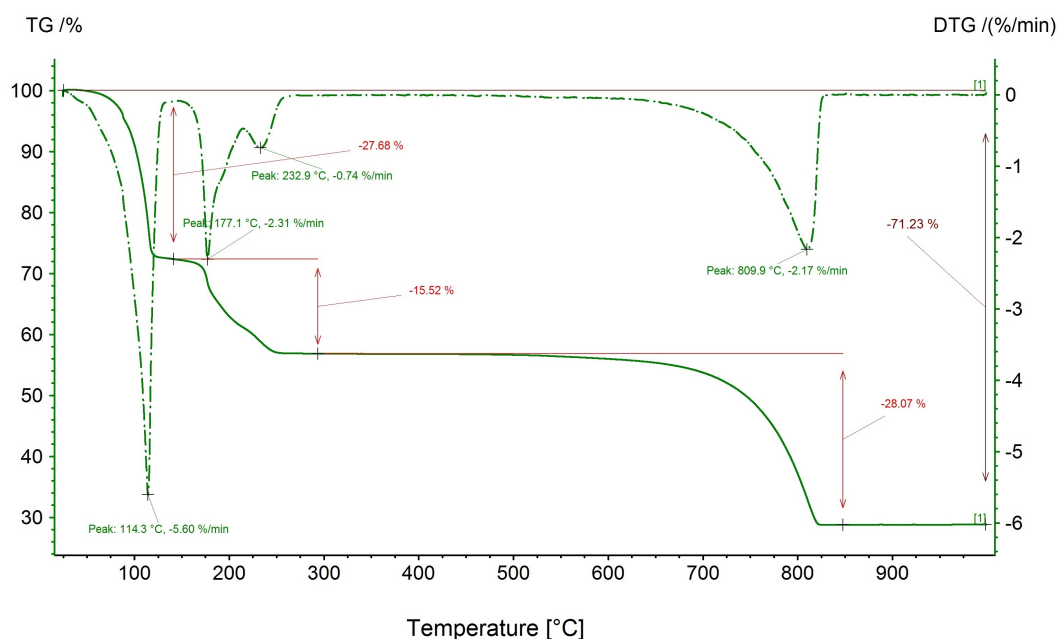


Figure 6.23: Results of the thermogravimetric analysis of $\text{NiCl}_2 \cdot 6 \text{H}_2\text{O}$ under air atmosphere.

The first peaks up to 250 °C belong to the loss of crystal water and formation of anhydrous NiCl_2 . After that, no decomposition took place up to 820 °C. Nickel chloride precursor which was not converted during the synthesis and remains in the structure will therefore not decompose below this temperature.

After this stage, nickel oxides are formed in addition to hydrochloric acid. It is therefore important to control the synthesis conditions, making sure that all precursors were converted and impurities were removed during the washing step, prior to the oven step. Higher temperatures during calcination can thereafter remove residual impurities or unconverted precursors.

Rate capability

Table 6.4 shows the evaluation of the rate capability tests from 0.1 C to 5 C after the 20th cycle in four stages and back to 0.1 C in a similar way as described for NMC111.

Table 6.4: Results from rate capability tests of NMC532 using nitrate (N) and chloride (C) precursors.

Sample	Precursor	Calcination temperature [°C]	Average discharge capacity [mAhg ⁻¹]	Discharge capacity last cycle [mAhg ⁻¹]
532 N 3	Nitrates	900	125.41	106.65
532 N 4	Nitrates	950	125.87	100.74
532 C 3	Chlorides	900	124.33	76.62
532 C 4	Chlorides	950	96.72	88.62

Overall, for non-symmetric NMC compounds, nitrate-prepared samples show significantly higher specific capacities as well as better capacity retention before and after the rate capability tests. One has to point out again: this NMC cathode material is not intended for high-power applications. However, a proper tailoring of the electrodes could enable higher cycling currents.

Both chloride-prepared samples have a specific discharge capacity of less than 100 mAhg⁻¹ after the tests, which makes them unattractive candidates for commercial applications, which can be explained by formation of insoluble intermediate nickel oxy- and hydroxy-chlorides as revealed by the thermogravimetric analysis shown above (see Figure 6.23).

The results reflect the data obtained from the cycling tests and underline the conclusions which were drawn in the earlier section.

Table 6.5 presents the parameters of the best non-symmetric NMC cathode material regarding both synthesis conditions and electrochemical performance.

Table 6.5: Parameters of the best NMC532 samples.

Parameter	Value
Sample	532 N 4
Precursor	Nitrates
Calcination Condition	Synthetic air flow
Temperature	950 °C
Discharge Capacity at 0.1 C 1 st Cycle	120.85 mAhg ⁻¹
Discharge Capacity at 0.1 C 100 th Cycle	117.40 mAhg ⁻¹
Coloumbic Efficiency at 0.1 C 100 th Cycle	99.54 %
Discharge Capacity at 0.2 C 1 st Cycle	121.63 mAhg ⁻¹
Discharge Capacity at 0.2 C 100 th Cycle	84.35 mAhg ⁻¹
Coloumbic Efficiency at 0.2 C 100 th Cycle	99.35 %

Cycling behaviour at higher cut-off voltages

Decreasing the amount of cobalt in the favour of nickel in NMC layered oxides seems to be a promising way in terms of cost reduction, better safety performance, and lower toxicity. Additionally, this could enable a wider voltage operating window for Li-ion battery cells.

Therefore, the best non-symmetric NMC material synthesized in this work (532 N 4, samples prepared using nitrate precursors at 950 °C) was tested with regard to its cycling behaviour at more positive potentials - i.e. up to 4.5 V (see Figure 6.24). Since state-of-the-art electrolytes based on LiPF₆ and alkyl carbonates tend to be oxidized at about 4.5 V (depending on the electrolyte composition, and on the cathode material), the upper cut-off voltage was set to this value (4.5 V vs Li/Li⁺).

The results show that, indeed, higher specific capacities were obtained, as expected. Increasing the upper cut-off voltage by 0.3 V leads to more than 33% higher capacity values. This makes this material one of the promising candidates for future applications. On the other hand it must be pointed out here that the specific capacity decay is more drastically compared to those samples cycled up to 4.2 V. This behaviour must be monitored in long term cycling to gain more information about capacity decay over several hundred cycles.

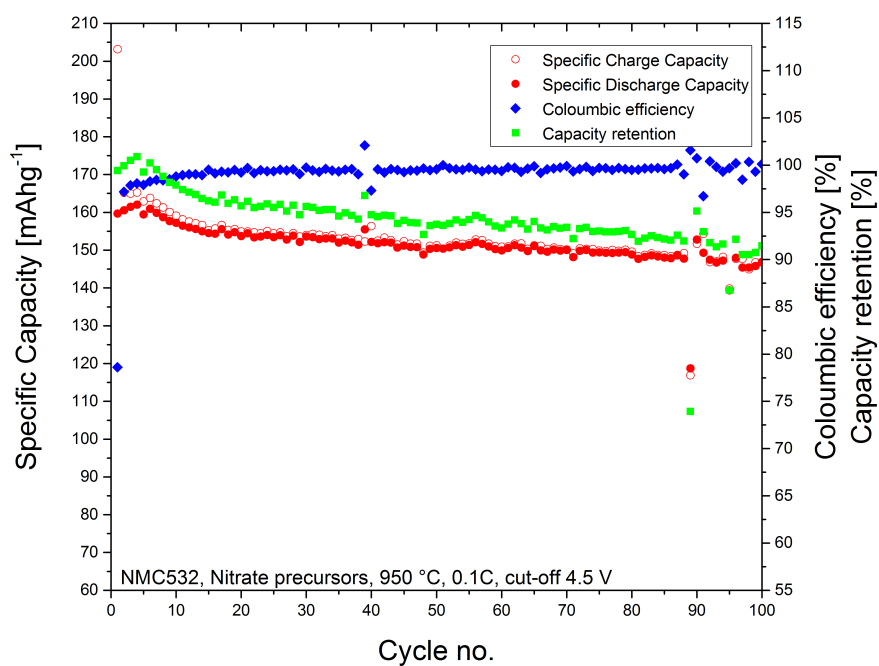


Figure 6.24: Cycling behaviour at 0.1C of NMC532 using nitrate precursors at 950 °C at a cut-off voltage of 4.5 V.

Overall, this reveals that NMC532 is suitable for operation at higher cut-off voltages, ready-to-market, thus enable an increase in the energy density, and can increase the overall voltage operation window and therefore decrease the amount of battery cells for electric drives.

6.3 Conclusion

Electrochemical characterization by means of cyclic voltammetry, galvanostatic intermittent titration technique, and cycling tests at different C-rates was performed. In addition to the electrochemical methods, *ex situ* X-ray diffraction was also applied in order to gain more information about structural changes at different stages of lithiation. Symmetric and non-symmetric NMC cathodes were evaluated and compared in terms of type of precursor, calcination temperature, and gas atmosphere.

It was proved that in the applied cycling range, nickel oxidation occurs from 2+ to 4+ during charging, and reduction during discharging. The results of both cyclic voltammetric measurements and *ex situ* X-ray diffraction analysis confirmed this statement. In addition, at higher cut-off voltages, cobalt oxidation from 3+ to 4+ state takes place. The unit cell parameter changes during cycling correspond to the calculated ionic radii.

The lithium ion diffusion coefficient during cycling varied between $10^{-15.5}$ and $10^{-13.0}$ cm^2s^{-1} , with minima at 3.65 V for discharging and 3.8 V during charging versus Li/Li⁺. The typical plateau region was observed in the 80% state-of-charge voltage window between 3.6 - 4.0 V, which is the commercially applied limitation of NMC111.

The performance of the symmetric NMC samples strongly depends on the amount of oxygen present in the oven during the thermal treatment. This behaviour is more pronounced in the case of the nitrate-based materials. The specific capacity of the synthesized material is significantly higher for those samples prepared under synthetic air flow. To the author's knowledge, this phenomenon has not been published yet for comparing muffle oven versus tube furnace and constant air flow; which only slightly differ in terms of atmospheric conditions.

Based on the findings described above, as well as on literature reports regarding this phenomenon for nickel-rich cathode materials, the non-symmetric NMC532 was synthesized under constant synthetic air flow using both chloride and nitrate precursors.

It was shown that the cycleability of chloride-based samples is significantly lower than of nitrate ones. This can be related to the formation of insoluble species - e.g. oxy- or hydroxychlorides. The assumption was confirmed by thermogravimetric analysis of the nickel precursor, NiCl₂·6H₂O.

Overall, for the symmetric composition, chloride-prepared samples show similar or in some cases even better results compared to nitrate-prepared ones. If the amount of nickel in the composition is increased, the formation of intermediate nickel side products leads to drastic decreases in terms of capacity and efficiency. Therefore, when synthesizing NMC materials with a higher amount of nickel, nitrate precursors should be preferred to the chloride ones.

Some NMC samples showed a monotonic decreasing trend in the capacity values within the first cycles, which could be related to the film formation at the cathode surface, similar to the SEI at the anode. The layer is usually formed during the first cycles (also called formation cycles) and has the role of stabilizing the surfaces - especially of the anode - and thus the cycleability of the whole cell.

By applying higher cut-off voltages - i.e. 4.5 V instead of 4.2 V - it is possible to significantly increase the specific capacity of NMC532. However, this seems to have a detrimental effect on the efficiency and cycle stability. Since state-of-the-art electrolytes for Li-ion batteries suffer from poor anodic stability, additional tests should be performed on NMC532 in advanced, high-voltage stable electrolytes.

7 Conclusions and further perspective

7.1 Conclusions

In this work, different compositions of NMC (NMC111 and NMC532) were characterized using *ab initio* techniques combined with physico-chemical and electrochemical characterization.

Electronic structure calculations of NMC111 demonstrated that above the usually applied cut-off voltage of 4.2 V, structural rearrangement occurs which can be associated with spinel formation. Combining all calculated information (bond lengths, magnetic moments and density of states), nickel and cobalt contribution to the overall cell reaction is much higher compared to manganese.

The unit cell parameter changes during cycling, as determined via *ex situ* X-ray diffraction analysis, showed the same trend as predicted by first principles calculations (see Section 3), but less pronounced. Real crystal structures always have a certain amount of impurities, cation mixing as for NMC, or a certain extend of crystal disorder, which is not pictured in the calculated “ideal” unit cells and can therefore lead to small deviations from experimental data.

Additionally, as already mentioned, due to the measurement procedure of *ex situ* analysis, the cell was allowed to relax between stopping the CV measurement and transferring the cathode to the X-ray diffractometer. Therefore, some discrepancy between the real composition and the calculated one, or re-intercalation of lithium ions might be observed. Overall, the parameter variations of both, experimental and theoretical observation show similar behaviour even though in less specificity.

In conclusion, the proposed reactions for x in $\text{Li}_x\text{Ni}_{1/3}\text{Mn}_{1/3}\text{Co}_{1/3}\text{O}_2$ are

$2/3 \leq x \leq 1$: Nickel oxidation from 2+ to 3+

$1/3 \leq x \leq 2/3$: Nickel oxidation from 3+ to 4+

$0 \leq x \leq 1/3$: Cobalt oxidation from 3+ to 4+

In this regions, the belonging ionic radii for the assumed oxidation states were calculated. It was shown that the unit cell parameter a, representing the interslab distance, correlates well with the average ionic radii assuming the oxidation states in the corresponding states of lithiation as proposed above.

The reduction of the critical raw material, cobalt, in favor of nickel, which shows the highest contribution to the overall cell reaction, is therefore reasonable, as in NMC532 for next generation Li-ion battery systems for EV applications.

The coprecipitation route was chosen as a convenient synthesis method, which lead to small spherical particles in nanometer scale, which further agglomerate into secondary particles of some micrometers of size to ensure high tap density.

To determine the influence of the different precursors and the corresponding impurities, physico-chemical characterization of the synthesized powders, NMC111 and NMC532, was performed. ICP analysis revealed that the amount of impurities, namely unreacted precursor species, is higher for lower synthesis temperature for nitrates, but can be removed at higher syntheses temperatures. For chloride-prepared samples, precursor impurities, which have not been removed during the synthesis procedure at the beginning, remain in the structure and can not be removed by thermal treatment.

The washing step is therefore crucial in the coprecipitation route for synthesis of NMC, especially when chloride precursors are used; but still, excessive rising with water can lead to ion-exchange between lithium and hydrogen and further on lithium deficiency in the structure.

The effect of the cation mixing between lithium and nickel, due to their similar ionic radii, was shown to be more pronounced for lower syntheses temperatures (< 850 °C). Additionally, calcination temperatures below 900 °C are not beneficial regarding electrochemistry and crystallinity, whereas low electrochemical activity was observed for these NMC samples. Enhancing the nickel content leads to a higher degree of cation-mixing, as observed for synthesized NMC532 samples.

For lower amounts of oxygen in the synthesis atmosphere, oxygen deficiency in the synthesized NMC samples was observed and the corresponding cathodes showed a constant decrease in terms of specific capacity during cycling without stabilization.

It was shown that for chloride prepared-samples, the atmospheric conditions are not as crucial compared to nitrate ones. For symmetric NMC composition, the electrochemical performance and cycleability showed encouraging similar behaviour (116.8 mAhg⁻¹ and 99.83% after 100 cycles at 0.1 C), which shows that chloride precursors can be applied for large-scale synthesis of NMC111 cathode material.

Nevertheless, when the nickel content in NMC is increased, the differences between both precursor types become more evident. This is caused by the formation of nickel hydroxychlorides or oxychlorides, which are insoluble and additionally, can cause serious problems related to side reactions in the electrolyte and further instability of the battery cell. Therefore, chloride precursors are not suitable for synthesis of high-nickel mixed transition metal oxides, especially at lower calcination temperatures.

Overall, it was shown that nitrate-prepared high-nickel NMC cathodes are stable and show encouraging specific energy density at 0.1 C up to 100 cycles (117.40 mAhg⁻¹ and 99.54% efficiency) even at higher cut-off voltages of 4.5 V (146.88 mAhg⁻¹ and 100% efficiency), which means an increase of more than 20% in terms of specific capacity.

Taking into account that no adjustment of the electrode preparation procedure was performed for any of these materials, the obtained results can be increased when optimizing the routine.

7.2 Further perspective

Interestingly, nitrate prepared samples synthesized at 900 °C showed different behaviour compared to all other samples. It was discussed that this can be linked to lithia losses, which must be further verified in ongoing research.

The increase of nickel content in unfavor of manganese and cobalt is the next logical step towards cheaper, high energy density Li-ion batteries. The stability of these materials (namely NMC622 and NMC811) is questionable and the safety is concerning. Further research must be performed to stabilize these compositions and improve their safety in order to make them a reasonable replacement for symmetric NMC.

The usage of chloride precursors for large-scale production of mixed metal oxides using spray roasting techniques should be tested for symmetric NMC, but difficulties might arise when the nickel content is enhanced. The temperatures, which were applied in this work, are too high for spray roasting techniques and are therefore not applicable. Pilot line tests for large-scale production using chloride precursors were already performed and are still ongoing (PyroBat project, GA no. 848603, founded by the Austrian Research Promotion Agency, FFG).

The formation of spinels at above 4.2 V can be predicted by calculation of the corresponding structure and comparison of the stability between the layered and the spinel structure, when less lithium is incorporated into the host matrices. Additionally, non-symmetric NMC compositions are to be calculated in comparison with NMC111. All properties can thereafter be related to the nickel content of the structure.

As already mentioned, the slurry preparation procedure was not optimized, having a relatively high amount of inactive material (carbon black and binder, 20%) in the electrodes. Enhancing the amount of active material (NMC, 80%) is favorable for commercial applications as the overall specific energy density can be greatly enhanced. The slurry preparation process can be optimized via determination of the viscosity, variation of the electrode thickness and loading, as well as usage of specific cathode binders, as commercially used.

The electrolyte plays an important role for the electrochemical performance of the battery cell. Additional tests using high-voltage electrolytes with better anodic stability, even at higher cut-off voltages, can show even better stability and cycleability of the presented optimized NMC532 cathode material.

Parts of this work were already published as follows:

Poster presentation

Fröhlich, K., Legotin, E., Trifonova, A.: *Estimation of Synthesis Parameters for Large-Scale Production of Lithium Nickel Manganese Cobalt Oxide* – in: European Materials Research Society Fall Meeting, Warsaw, 2016 (Best Presentation Award).

Fröhlich, K., Kahr, J., Abrahams, I., Trifonova, A.: *Crystallographic analysis of structural changes in lithium nickel manganese cobalt oxides at different stages of lithiation* – in: 18th International Meeting on Lithium Batteries, Chicago IL 2016.

Fröhlich, K., Trifonova, A.: *Density functional theory as a powerful tool for battery material research* – in: 2nd Workshop in the Advances of Li-Battery Research, Liverpool 2014.

Oral presentation

Fröhlich, K., Abrahams, I., Blaha, P., Trifonova, A.: *Application of density functional theory for design and understanding of NMC cathodes* – in: European Materials Research Society Fall Meeting, Warsaw, 2017 (Best Student Presentation Award).

Fröhlich, K., Trifonova, A., Blaha P.: *Understanding of electrochemical processes in lithium nickel manganese cobalt oxide using density functional theory* – in: 5th Regional Symposium on Electrochemistry –South East Europe, Pravets, 2015.

Publication

Fröhlich, K., Legotin, E., Bärhold, F., Trifonova, A.: *New large-scale production route for synthesis of lithium nickel manganese cobalt oxide*, Journal of Solid State Electrochemistry 21/12 (2017): 3403-3410.

Pichler, F., Fröhlich, K., Stankov, S., Trifonova, A., Cifrain, M.: *Thermodynamical modeling of lithium nickel manganese cobalt oxide electrodes*, International Journal of Electronics Communication and Computer Engineering - IJECCE 8/3 (2017): 188-193.

Fröhlich, K., Bimashofer, G., Fafilek, G., Pichler, F., Cifrain, M., Trifonova, A.: *Electrochemical Investigation of Thermodynamic and Transport Phenomena in LP30 Electrolyte with Various Concentrations of Conducting Salt*, ECS Trans. 73/1 (2016): 83-93.

Bibliography

- [1] R. Berger, Automotive Competence Center & Forschungsgesellschaft Kraftfahrwesen mbH Aachen. *Study, E-mobility Index Q1* (2017).
- [2] X. Wu, X. Hu, S. Moura, X. Yin, V. Pickert. *Journal of Power Sources* 333 (2016), pp. 203–212.
- [3] B. Nykvist, M. Nilsson. *Nature Climate Change* 5 (2015), pp. 329–332.
- [4] K. Fröhlich, E. Legotin, A. Trifonova. *Poster, European Materials Research Society Fall Meeting, Warsaw*. 2016.
- [5] K. Fröhlich, E. Legotin, F. Bärhold, A. Trifonova. *Journal of Solid State Electrochemistry* 21 (12 2017), pp. 3403–3410.
- [6] P. Busch. German. Pat. DD 290 979 A5. 1991.
- [7] N. Nitta, F. Wu, J. T. Lee, Gleb. Yushin. *Materials Today* 18, 5 (2015), pp. 252–264.
- [8] L. Jiao, Z. Liu, Z. Sun, T. Wu, Y. Gao, H. Li, F. Li, L. Niu. *Electrochimica Acta* 259 (2018), pp. 48–55.
- [9] J. Zheng, W.H. Kan, A. Manthiram. *ACS Applied Materials & Interfaces* 7 (12 2015), pp. 1944–8244.
- [10] S.-T. Myung, F. Maglia, K.-J. Park, C.S. Yoon, P. Lamp, S.-J. Kim, Y.-K. Sun. *ACS Energy Letters* 2 (2017), pp. 196–223.
- [11] H. J. Gores, H. G. Schweiger, M. Multerer. Ed. by S.S. Zhang. *Research Signpost Special Review Books*, 2007. Chap. 11.
- [12] D. Aurbach, Y. Talyosef, B. Markovsky, E. Markevich, E. Zinigrad, L. Asraf, J.S. Gnanaraj, H.-J. Kim. *Electrochimica Acta* 50 (2004), pp. 247–254.
- [13] K. Fröhlich, G. Bimashofer, G. Faflek, F. Pichler, M. Cifrain, A. Trifonova. *ECS Transactions* 73 (1). 2016.
- [14] J. B. Goodenough, Y. Kim. *Chemistry of Materials* 22, 3 (2010), pp. 587–603.
- [15] L. Yang, B. Ravdel, B.L. Lucht. *Electrochemical and Solid-State Letters* 13 (8 2010), A95–A97.
- [16] K. Xu. *Chemical Reviews* 104 (10 2004), pp. 4303–4418.
- [17] K. Yamaguchi, Y. Domi, H. Usui, M. Shimizu, K. Matsumoto, T. Nokami, T. Itoh, H. Sakaguchi. *Journal of Power Sources* 338 (2017), pp. 103–107.
- [18] L. Yue, J. Ma, J. Zhang, J. Zhao, S. Dong, Z. Liu, G. Cui, L. Chen. *Energy Storage Materials* 5 (2016), pp. 139–164.
- [19] J.-M. Tarascon, M. Armand. *Nature* 414 (2001), pp. 359–367.
- [20] R. Yazami, P. Touzain. *Journal of Power Sources* 9.3 (1983), pp. 365–371.
- [21] X.M. Liu, Z.D. Huang, S.W. Oh, B. Zhang, P.C. Ma, M.M.F. Yuen, J.K. Kim. *Composites Science and Technology* 72 (2012), pp. 121–144.

- [22] R. Raccichini, A. Varzi, S. Passerini, B. Scrosati. *Nature Materials* 14 (2015), pp. 271–279.
- [23] S. Wen, G. Li, R. Ren, C. Li. *Materials Letters* 148 (2015), pp. 130–133.
- [24] Y. Yan, L. Ben, Y. Zhan, Y. Liu, Y. Jin, S. Wang. *Progress in Natural Science: Materials International* 26 (2016), pp. 368–374.
- [25] B. La, L. Eude, K. Pereira ramos, C. Sorin. *Electrochimica Acta* 53 (2008), pp. 5528–5532.
- [26] A. Rezqita, R. Hamid, S. Schwarz, H. Kronberger, A. Trifonova. *ECS Transactions* 66 (2015), pp. 17–27.
- [27] K. Mizushima, P.C. Jones, P.J. Wiseman, J.B. Goodenough. *Solid State Ionics* 3-4 (1981), pp. 171–174.
- [28] Commission of the European Parliament, Tackling the Challenges in commodity markets on raw materials. European Commission, 2011.
- [29] M. Labrini, I. Saadoune, A. Almaggoussi, J. Elhaskouri, P. Amoros. *Materials Research Bulletin* 47 (2012), pp. 1004–1009.
- [30] B. Ammundsen, J. Desilvestro, T. Groutso, D. Hassell, J.B. Metson, E. Regan, R. Steiner, P.J. Pickering. *Journal of The Electrochemical Society* 147 (11 2000), pp. 4078–4082.
- [31] I.J. Davidson, R.S. McMillan, J.J. Murray, J.E. Greedan. *Journal of Power Sources* 54 (2 1995), pp. 232–235.
- [32] L. Croguennec, P. Deniard, R. Brec. *Journal of The Electrochemical Society* 144 (10 1997), pp. 3323–3330.
- [33] J. Reed, G. Ceder. *Electrochemical and Solid-State Letters* 5 (7 2002), A145–A148.
- [34] T. Ohzuku, Y. Makimura. *Chemistry L* 7 (2001), pp. 642–643.
- [35] I. Belharouak, Y.-K. Sun, J. Liu, K. Amine. *Journal of Power Sources* 123 (2003), pp. 247–252.
- [36] I. Belharouak, W. Lu, D. Vissers, K. Amine. *Electrochemistry Communications* 8 (2006), pp. 329–335.
- [37] A.K. Padhi, K.S. Nanjundaswamy, J.B. Goodenough. *Journal of The Electrochemical Society* 144 (4 1997), pp. 1188–1194.
- [38] Z. Gong, Y. Yang. *Energy & Environmental Science* 4 (2011), pp. 3223–3242.
- [39] F. Schipper, E.M. Erickson, C. Erk, J.-Y. Shin, F.F. Chesneau, D. Aurbach. *Journal of The Electrochemical Society* 164 (1 2017), A6220–A6228.
- [40] C.M. Julien, A. Mauger, K. Zaghib, H. Groult. *Inorganics* 2.2 (2014), pp. 132–154.
- [41] M.M. Thackeray. *Progress in Solid State Chemistry* 25 (1 1997), pp. 1–71.
- [42] D. Liu, W. Zhu, J. Trottier, C. Gagnon, F. Barray, A. Guerfi, A. Mauger, H. Groult, C.M. Julien, J.B. Goodenough, K. Zaghib. *RSC Advances* 4 (2014), pp. 154–167.
- [43] M.M. Thackeray. *American Ceramics Society* (2000), pp. 1–23.
- [44] T. Numata, C. Amemiya, T. Kumeuchi, M. Shirakata, M. Yonezawa. *Journal of Power Sources* 97-98 (2001), pp. 358–360.
- [45] G. Kresse, J. Hafner. *Physical Review B* 47 (1993), p. 558.
- [46] P. Giannozzi, S. Baroni, N. Bonini, M. Calandra, R. Car, C. Cavazzoni, D. Ceresoli, G. L. Chiarotti, M. Cococcioni, I. Dabo, A. Dal Corso, S. Fabris, G. Fratesi, S. de Gironcoli, R. Gebauer, U. Gerstmann, C. Gougoussis, A. Kokalj, M. Lazzeri, L.

- Martin-Samos, N. Marzari, F. Mauri, R. Mazzarello, S. Paolini, A. Pasquarello, L. Paulatto, C. Sbraccia, S. Scandolo, G. Sclauzero, A. P. Seitsonen, A. Smogunov, P. Umari, R. M. Wentzcovitch. *Journal of Physics: Condensed Matter* 21 (2009), p. 395502.
- [47] P. Blaha, K. Schwarz, P. Sorantin, S.B. Trickey. *Computer Physics Communications* 59 (2 1990), pp. 399–419.
- [48] G. Ceder, A. Van der Ven. *Electrochimica Acta* 45 (1999), pp. 131–150.
- [49] A. Van der Ven, G. Ceder. *Physical Review B* 59.2 (1999), pp. 742–749.
- [50] X. Lv, Z. Xu, J. Li, J. Chen, Q. Liu. *Journal of Solid State Chemistry* 239 (2016), pp. 228–236.
- [51] Y. Xiao, F.C. Zhang, J.I. Han. *Solid State Ionics* 294 (2016), pp. 73–81.
- [52] A. Liivat, J.O. Thomas. *Computational Materials Science* 50 (2010), pp. 191–197.
- [53] M.K. Aydinol, A.F. Kohan, G.Ceder. *Journal of Power Sources* 68 (1997), pp. 664–668.
- [54] Y.S. Meng, Y.W. Wu, B.J. Hwang, Y. Li, G. Ceder. *Journal of the Electrochemical Society* 151.8 (2004), A1134–A1140.
- [55] M.S. Islam, C.A.J. Fisher. *Chemical Society Reviews* 43 (2013), pp. 185–204.
- [56] K. Fröhlich, H. Vasilchina, S. Stankov, A. Trifonova. *oral presentation, 3rd Indo-Austrian Symposium: Advances in Materials Engineering* (2016).
- [57] R. E. Doe, T.K. Müller, G. Ceder, J. Barker, K.A. Persson. Pat. US 2012/0279856 A1. Aug. 30, 2012.
- [58] G. Vallerverdu, M. Minvielle, N. Andreu, D. Gonbeau, I. Baraille. *Surface Science* 649 (2016), pp. 46–55.
- [59] X. Lu, Z. Xu, J. Li, J. Chen, Q. Liu. *Journal of Alloys and Compounds* 681 (2016), pp. 253–259.
- [60] B.J. Hwang, Y.W. Tsai, D. Carlier, G. Ceder. *Chemistry of Materials* 15 (2003), pp. 3676–3682.
- [61] Y. Koyama, I. Tanaka, H. Adachi, Y. Makimura, T. Ohzuku. *Journal of Power Sources* 119-121 (2003), pp. 644–648.
- [62] K. Min, K. Kim, C. Jung, S.-W. Seo, Y.Y. Song, H.S. Lee, J. Shin, E. Cho. *Journal of Power Sources* 315 (2016), pp. 111–119.
- [63] S. Miao, M. Kocher, P. Rez, B. Fultz, Y. Ozawa, R. Yazami, C.C. Ahn. *Journal of Physical Chemistry B* 109 (49 2005), pp. 23473–23479.
- [64] E. Schrödinger. *Annalen der Physik* 4.80 (1926), pp. 361–376.
- [65] M. Born, R. Oppenheimer. *Annalen der Physik* 389.20 (1927), pp. 457–484.
- [66] P. Hohenberg, W. Kohn. *Physical Review* 136B (1964), p. 864.
- [67] W. Kohn, L.S. Sham. *Physical Review* 136B (1965), p. 864.
- [68] Richard M. Martin. Cambridge University Press, *Electronic Structure: Basic Theory and Practical Methods*, 2008.
- [69] D.M. Ceperley, B.J. Adler. *Physical Review Letters* 45 (7 1980), p. 566.
- [70] J.P. Perdew, Y. Wang. *Physical Review B* 45 (23 1992), p. 13244.
- [71] J.C. Slater. *Physical Review* 51 (1937), pp. 840–846.
- [72] P. Blaha, K. Schwarz, GKH Madsen, D. Kvasnicka, J. Luitz. *WIEN2k, Austria: Vienna Universtiy of Technology* (2013).

- [73] M. Aykol, S. Kim, C. Wolverton. *Journal of Physical Chemistry C* 119 (2015), pp. 19053–19058.
- [74] Walter Nernst. *Habilitation* (1889).
- [75] Z. Wu, R.E. Cohen. *Physical Review B* 73 (23 2006), p. 235116.
- [76] J.P. Perdew, A. Ruzsinszky, G.I. Csonka, O.A. Vydrov, G.E. Scuseria, L.A. Constantin, X. Zhou, K. Burke. *Physical Review Letters* 102 (2009), p. 039902.
- [77] J.P. Perdew, K. Burke, M. Ernzerhof. *Physical Review Letters* 77.19 (1996), pp. 3865–3868.
- [78] M.S. Whittingham. *Chemical Reviews* 104 (10 2004), pp. 4271–4302.
- [79] T. Zhang, D. Li, Z. Tao, J. Chen. *Progress in Natural Science: Materials International* 23 (3 2013), pp. 256–272.
- [80] M. Aydinol, A. Kohan, G. Ceder, K. Cho, J. Joannopoulos. *Physical Review B - Condensed Matter and Materials Physics* 56 (3 1997), pp. 1354–1365.
- [81] A.V. Ruban, I.A. Abrikosov. *Reports on Progress in Physics* 71 (2008), p. 046501.
- [82] Y. S. Meng. PhD thesis. Singapore-MIT Alliance, 2005.
- [83] K. Momma, F. Izumi. *Journal of Applied Crystallography* 44 (2011), pp. 1272–1276.
- [84] K. Shimoda, M. Oishi, T. Matsunaga, M. Murakami, K. Yamanaka, H. Arai, Y. Ukyo, Y. Uchimoto, T. Ohta, E. Matsubara, Z. Ogumi. *Journal of Materials Chemistry A* 5 (14 2017), pp. 6695–6707.
- [85] T. Segi, R. Masuda, Y. Kobayashi, T. Tsubota, Y. Yoda, M. Seto. *Hyperfine Interactions* (2016), p. 7.
- [86] M.D. Johannes, K. Swider-Lyons, C.T. Love. *Solid State Ionics* 286 (2016), pp. 83–89.
- [87] J.R. Dahn, E.W. Fuller, M. Obrovac, U. von Sacken. *Solid State Ionics* 69 (3-4 1994), pp. 265–270.
- [88] S. Brunauer, P.H. Emmett, E. Teller. *Journal of the American Chemical Society* 60 (2 1938), pp. 309–319.
- [89] I. Langmuir. *Journal of the American Society* 38 (11 1916), pp. 2221–2295.
- [90] E.P. Barrett, L.G. Joyner, P.P. Halenda. *The Volume and Area Distribution in Porous Substances* 73 (1951), pp. 373–380.
- [91] G. Mie. *Annalen der Physik* 4.25 (1908), pp. 377–445.
- [92] W.H. Bragg. *Proceedings of the Royal Society of London Series A* 88.605 (1916), pp. 428–38.
- [93] H.M. Rietveld. *Journal of Applied Crystallography* 2.2 (1969), pp. 65–71.
- [94] A.C. Larson, R.B. Von Dreele. Tech. rep. LAUR-86-748. Los Alamos National Library, 1987.
- [95] B.H. Toby. *Journal of Applied Crystallography* 34 (2001), p. 210.
- [96] L.F. Nazar, I. Swainson, Y.-H. Rho, S.-C. Yin. *Chemistry of Materials* 18 (2006), p. 1901.
- [97] S.-T. Myung, S. Komaba, K. Kurihara, K. Hosoya, N. Kumagai, Y.-K. Sun, I. Nakai, M. Yonemura, T. Kamiyama. *Chemistry of Materials* 18 (2006), pp. 1658–1666.
- [98] C. Julien, A. Mauger, K. Zaghieb, H. Groult. *Materials* 9 (7 2016), p. 595.

- [99] R.E. García, Y.-M. Chiang, E.C. Carter, P. Limthongkul, C.M. Bishop. *Journal of The Electrochemical Society* 152 (1 2005), A255–A263.
- [100] M. Okubo, E. Hosono, J. Kim, M. Enomoto, N. Kojima, T. Kudo, H. Zhou, I. Honma. *Journal of the American Society* 129 (23 2007), pp. 7444–7452.
- [101] S.-H. Kang, C.S. Johnson, J.T. Vaughey, K. Amine, M.M. Thackeray. *Journal of The Electrochemical Society* 153 (6 2006), A1186–A1192.
- [102] X. Zhao, Y. Cui, L. Xiao, H. Liang, H. Liu. *Solid State Ionics* 192 (2011), pp. 321–325.
- [103] M.C. Biesinger, B.P. Payne, L.W.M. Lau, A. Gerson, R.St.C. Smart. *Surface and Interface Analysis* 41 (2009), pp. 324–332.
- [104] M.C. Biesinger, B.P. Payne, A.P. Grosnevor, L.W.M. Lau, A.R. Gerson, R.St.C. Smart. *Applied Surface Science* 257 (2011), pp. 2717–2730.
- [105] J. Starcevic, L. Coronado. Pat. WO2015EP56511. 2015.
- [106] M. Faraday. *Philosophical Transactions of the Royal Society of London* 124 (1834), pp. 77–122.
- [107] M.K. Aydinol, A.F. Kohan, G. Ceder, K. Cho, J. Joannopoulos. *Physical Review B* 56 (1997).
- [108] EL-CELL. Ed. by Hamburg EL-CELL GmbH. 2016.
- [109] W. Weppner, R.A. Huggins. *Journal of the Electrochemical Society* 124 (10 1977), pp. 1569–1578.
- [110] J.M. Paulsen, C.L. Thomas, J.R. Dahn. *Journal of the Electrochemical Society* 147 (3 2000).
- [111] K.M. Shaju, G.V. Subba Rao, B.V.R. Chowdari. *Electrochimica Acta* 48 (2003), pp. 2691–2703.
- [112] M. Dubarry, V. Svoboda, R. Hwu, B.Y. Liaw. *Electrochemical and Solid-State Letters* 9 (10 2006), A454–A457.
- [113] L. Peng, Y. Zhu, U. Khakoo, D. Chen, G. Yu. *Nano Energy* 17 (2015), pp. 36–42.
- [114] P. Gao, G. Yang, H. Liu, L. Wang, H. Zhou. *Solid State Ionics* 207 (2012), pp. 50–56.
- [115] K.M. Shaju, G.V. Subba Rao, B.V.R. Chowdari. *Journal of the Electrochemical Society* 151 (9 2004), A1324–A1332.
- [116] R.D. Shannon. *Acta Crystallographica* A32 (1976), p. 751.
- [117] M.S. Idris, A.R. West. *Journal of the Electrochemical Society* 159 (4 2012), A396–A401.
- [118] G. Sun, X. Yin, W. Yang, A. Song, C. Jia, W. Yang, Q. Du, Z. Ma, G. Shao. *Physical Chemistry Chemical Physics* (44, accepted manuscript 2017).
- [119] S.-W. Lee, H. Kim, M.-S. Kim, H.-C. Youn, K. Kang, B.-W. Cho, K.C. Roh, K.-B. Kim. *Journal of Power Sources* 315 (2016), pp. 261–268.
- [120] F. Wang, Y. Zhang, J. Zou, W. Liu, Y. Chen. *Journal of Alloys and Compounds* 558 (2013), pp. 172–178.
- [121] D. Aurbach, K. Gamolsky, B. Markovsky, G. Salitra, Y. Gofer, U. Heider, R. Oesten, M. Schmidt. *Journal of the Electrochemical Society* 147 (4 2000), pp. 1322–1331.

- [122] L. Yang, B.L. Lucht. *Electrochemical and Solid-State Letters* 12 (12 2009), A229–A231.
- [123] W. Kohs, J. Kahr, A. Ahniyaz, N. Zhang, A. Trifonova. *Journal of Solid State Electrochemistry* 21 (12 2017), pp. 3389–3401.
- [124] Y. Qian, C. Schultz, P. Niehoff, T. Schwieters, S. Nowak, F.M. Schappacher, M. Winter. *Journal of Power Sources* 332 (2016), pp. 60–71.
- [125] S.-L. Wu, W. Zhang, X. Song, A.K. Shukla, G. Liu, V. Battaglia, V. Srinivasan. *Journal of the Electrochemical Society* 159 (4 2012), A438–A444.
- [126] S.K. Mishra, S.B. Kanungo. *Journal of Thermal Analysis* 38 (1992), pp. 2417–2436.

List of Figures

2.1	Schematic working principle of Li-ion batteries.	5
2.2	Electrochemical window of the electrolyte.	8
2.3	Three dimensional image of the structure of LiCoO_2	12
2.4	The ternary system between LCO, LNO and LMO.	13
2.5	Three dimensional image of the structure of LiFePO_4	14
2.6	Three dimensional image of the structure of LiMn_2O_4	16
3.1	Partition of a unit cell in the augmented plane wave method, where two different types of atoms (black and grey) are included.	22
3.2	Input parameters for <i>ab initio</i> calculations using WIEN2k.	22
3.3	Initial minimal models of $\text{LiNi}_{1/3}\text{Mn}_{1/3}\text{Co}_{1/3}\text{O}_2$ based on LiCoO_2	27
3.4	Total energy of NMC V1 with respect to the number of k-points.	29
3.5	Total energy of NMC V1 with respect to RKmax.	29
3.6	Initial super cell models and corresponding state of lithiation at various points during charging. (a) Experimentally derived NMC charging curve and selected points for electronic structure calculations (b) Initial models before optimization and their lithium content for x in $\text{Li}_{1-x}\text{Ni}_{1/3}\text{Mn}_{1/3}\text{Co}_{1/3}\text{O}_2$ (1) - fully lithiated, 27 lithium ions (2) - 25 lithium ions (3) 17 lithium ions (4) 5 lithium ions.	32
3.7	Calculated unit cell parameters trend during charging/discharging.	34
3.8	Optimized structural models at different states of lithiation for x in $\text{Li}_{1-x}\text{Ni}_{1/3}\text{Mn}_{1/3}\text{Co}_{1/3}\text{O}_2$	35
3.9	Calculated bond lengths changes during charging/discharging.	37
3.10	Calculated intercalation voltage of the super cell structures of NMC.	38
3.11	O p-states and total density of states for x in $\text{Li}_{1-x}\text{Ni}_{1/3}\text{Mn}_{1/3}\text{Co}_{1/3}\text{O}_2$	39
3.12	Total and partial density of states of the transition metals for x = 0 in $\text{Li}_{1-x}\text{Ni}_{1/3}\text{Mn}_{1/3}\text{Co}_{1/3}\text{O}_2$	40
3.13	Total and partial density of states of the transition metals for x = 0.07 in $\text{Li}_{1-x}\text{Ni}_{1/3}\text{Mn}_{1/3}\text{Co}_{1/3}\text{O}_2$	41
3.14	Total and partial density of states of the transition metals for x = 0.37 in $\text{Li}_{1-x}\text{Ni}_{1/3}\text{Mn}_{1/3}\text{Co}_{1/3}\text{O}_2$	42
3.15	Total and partial density of states of the transition metals for x = 0.63 in $\text{Li}_{1-x}\text{Ni}_{1/3}\text{Mn}_{1/3}\text{Co}_{1/3}\text{O}_2$	43
3.16	Super cell structure including numbering of particular transition metals. Green...Li, Red...O, Blue...Co, Grey...Ni, Purple...Mn.	44
3.17	Calculated magnetic moments during charging, including mean values in grey.	45

4.1	Synthesis steps for coprecipitation route to obtain NMC.	48
5.1	Representative adsorption and desorption isothermal curve.	51
5.2	X-ray diffraction on a crystal.	54
5.3	SEM image of NMC synthesized using nitrate (left) and chloride (right) precursors.	57
5.4	Example for particle size distribution of NMC.	58
5.5	Specific surface areas and pore volumes for different synthesis conditions (temperatures and precursors).	59
5.6	X-ray diffraction pattern at different stages of the synthesis.	61
5.7	TEM images of NMC using chloride (left) and nitrate (right) precursors.	61
5.8	XRD pattern of NMC using chloride (left) and nitrate (right) precursors.	62
5.9	Unit cell parameters and amount of lithium/nickel cation mixing derived by Rietveld fit.	63
5.10	Variation of the Li/M-ratio of NMC532 with synthesis temperature.	67
5.11	SEM images of NMC532 synthesized at different temperatures.	68
5.12	D50 parameter using chloride (left) and nitrate (right) precursors for different synthesis temperatures.	69
5.13	XRD pattern of NMC532 using chloride (left) and nitrate (right) precursors.	70
5.14	Unit cell parameters and amount of lithium/nickel cation mixing of NMC532 derived by Rietveld fit.	71
5.15	XPS survey spectra of self-synthesized samples NMC111 (red), NMC532 (black) and commercial NMC111 samples from BASF (green) and Sigma Aldrich (purple).	72
5.16	XPS detail spectra of the Mn 2p _{3/2} region of NMC111.	74
6.1	Illustration of the test cells for CV measurements, El Cell GmbH.	80
6.2	Example for determination of real specific discharge capacity of NMC.	80
6.3	Scheme of voltage and current trend during one pulse of the GITT measurement.	82
6.4	Specially adapted coin cells; the top was covered with Mylar foil.	84
6.5	Cyclic voltammogram of NMC.	85
6.6	Open-circuit voltage and incremental capacity evolution of Li _{1-x} Ni _{1/3} Mn _{1/3} Co _{1/3} O ₂ during delithiation (charging).	86
6.7	Diffusion coefficient of lithium ions in NMC111 for charging/discharging from 3.2 V to 4.2 V.	87
6.8	Reference pattern of different cathode and sealing compounds.	89
6.9	XRD pattern of an uncycled cathode before (above) and after (below) the Mylar subtraction.	90
6.10	Unit cell parameters trend during charging/discharging.	91
6.11	Calculated average ionic radius with lithium content assuming nickel oxidation followed by cobalt oxidation.	92
6.12	Specific discharge capacities as derived from CV measurements for different synthesis of NMC111.	93
6.13	Cycling behaviour at 0.1C of symmetric NMC using nitrates (111 N SA, left) and chlorides (111 C SA, right) calcined under synthetic air flow.	95

6.14	Cycling behaviour at 0.1C of symmetric NMC using nitrates (111 N MO, left) and chlorides (111 C MO, right), calcined in the muffle oven.	95
6.15	Cycling behaviour at 0.2C of symmetric NMC using nitrates (111 N SA, left) and chlorides (111 C SA, right) calcined under synthetic air flow. . .	97
6.16	Cycling behaviour at 0.2C of symmetric NMC using nitrates (111 N MO, left) and chlorides (111 C MO, right) calcined in the muffle oven.	97
6.17	Specific discharge capacities of non-symmetric NMC using different precursors and different calcination temperatures.	101
6.18	Specific discharge capacities of NMC532 using nitrate precursors and different calcination temperatures when cycled to 4.5 V.	102
6.19	Cycling behaviour at 0.1C of NMC532 using chloride precursors at 900 °C (532 C 3, left) and 950 °C (532 C 4, right).	103
6.20	Cycling behaviour at 0.1C of NMC532 using nitrate precursors at 900 °C (532 N 3, left) and 950 °C (532 N 4, right).	103
6.21	Cycling behaviour at 0.2C of NMC532 using chloride precursors at 900 °C (532 C 3, left) and 950 °C (532 C 4, right).	104
6.22	Cycling behaviour at 0.2C of NMC532 using nitrate precursors at 900 °C (532 N 3, left) and 950 °C (532 N 4, right).	104
6.23	Results of the thermogravimetric analysis of NiCl ₂ · 6 H ₂ O under air atmosphere.	106
6.24	Cycling behaviour at 0.1C of NMC532 using nitrate precursors at 950 °C at a cut-off voltage of 4.5 V.	109

List of Tables

2.1	Commercialized cathode materials and their characteristics.	7
3.1	Crystallographic parameters of LCO.	23
3.2	Fractional atomic coordinates in rhombohedral setting and RMT values for LCO.	24
3.3	Comparison of different approximation methods for the exchange-correlation functional of intercalated and fully deintercalated LCO structures.	25
3.4	Model input parameters of lithium metal.	26
3.5	Comparison of different approximation methods for the exchange-correlation potential of bcc Li.	26
3.6	Total energy in Rydberg of the intercalated and deintercalated NMC structures.	27
3.7	Theoretical nominal voltages of NMC.	28
3.8	Initial unit cell parameters of NMC supercell.	30
3.9	Calculated super cell models and corresponding states of lithiation for x in $\text{Li}_{1-x}\text{Ni}_{1/3}\text{Mn}_{1/3}\text{Co}_{1/3}\text{O}_2$	31
3.10	Calculated structural data of optimized super cell structures.	36
5.1	Crystallographic parameters of NMC111.	55
5.2	Results of ICP-OES analysis and anion determination using chloride precursor.	56
5.3	Results of ICP-OES analysis and anion determination using nitrate precursor.	56
5.4	Particle size distribution of symmetric NMC.	59
5.5	Distribution of the transition metals and oxygen in NMC111 synthesized under different atmospheric conditions.	64
5.6	Unit cell parameters and cation mixing for NMC111 derived by Rietveld fit.	65
5.7	Results of ICP-OES analysis of NMC532 using nitrate (N) and chloride (C) precursors.	66
5.8	Particle size distribution of non-symmetric NMC.	67
5.9	Results from gas adsorption measurements of NMC532 using nitrate (N) and chloride (C) precursors.	69
5.10	Relative O, Mn, Ni and Li contents for NMC111, NMC532 and two commercial samples.	72
5.11	Determined oxidation states of the transition metals for symmetric and non-symmetric NMC.	73
6.1	Ionic radii of the corresponding transition metal ions.	92
6.2	Results from rate capability tests of NMC111 using nitrate (N) and chloride (C) precursors.	99

6.3	Parameters of the best NMC111 samples.	100
6.4	Results from rate capability tests of NMC532 using nitrate (N) and chloride (C) precursors.	107
6.5	Parameters of the best NMC532 samples.	108

Appendix

Atomic positions of the optimized super cell structures are presented in the following pages.

The numbers of lithium atoms, x in $\text{Li}_x\text{Ni}_{1/3}\text{Mn}_{1/3}\text{Co}_{1/3}\text{O}_2$ and total number of atoms for all calculated and optimized super cell structures is displayed in the following table.

x	No. Li	Total No. atoms
1.00	27	108
0.93	25	106
0.63	17	98
0.37	5	91

Atomic positions for $x = 0.37$ in $\text{Li}_x\text{Ni}_{1/3}\text{Mn}_{1/3}\text{Co}_{1/3}\text{O}_2$

Number	Atom	Label	x	y	z
1	Li	Li1	0.91417	0.25574	0.49505
2	Li	Li2	0.36850	0.04371	0.49942
3	Li	Li3	0.34613	0.63202	0.50776
4	Li	Li4	0.84303	0.76581	0.48062
5	Li	Li5	0.75796	0.14549	0.16487
6	Li	Li6	0.12431	0.67024	0.16655
7	Li	Li7	0.44330	0.50214	0.16341
8	Li	Li8	0.36827	0.04766	0.84714
9	Li	Li9	0.05813	0.39525	0.84336
10	Li	Li10	0.65376	0.77919	0.83422
11	O	O1	0.29062	0.32592	0.27097
12	O	O2	0.61772	0.32751	0.27160
13	O	O3	0.92860	0.30763	0.26266
14	O	O4	0.28628	0.65882	0.27272
15	O	O5	0.60075	0.64662	0.26670
16	O	O6	0.96578	0.65192	0.26636
17	O	O7	0.28369	0.98497	0.27373
18	O	O8	0.61532	0.98973	0.27095
19	O	O9	0.95132	0.99107	0.26731
20	O	O10	0.99646	0.96520	0.72091
21	O	O11	0.32795	0.96503	0.72630
22	O	O12	0.66384	0.95989	0.72828
23	O	O13	0.99889	0.29714	0.72713
24	O	O14	0.32772	0.29575	0.72579
25	O	O15	0.66273	0.29768	0.72820
26	O	O16	0.99914	0.63188	0.72420
27	O	O17	0.32856	0.62978	0.72615
28	O	O18	0.66560	0.63833	0.72626
29	O	O19	0.15004	0.27710	0.93630
30	O	O20	0.48822	0.26539	0.93833
31	O	O21	0.83006	0.28090	0.93860
32	O	O22	0.15176	0.59827	0.93663
33	O	O23	0.49259	0.61303	0.93653
34	O	O24	0.81877	0.60436	0.93798
35	O	O25	0.16351	0.94512	0.93685
36	O	O26	0.48443	0.94090	0.93862
37	O	O27	0.81649	0.93486	0.93610
38	O	O28	0.05534	0.20873	0.39513
39	O	O29	0.39619	0.20742	0.39938
40	O	O30	0.73607	0.21433	0.39758
41	O	O31	0.06264	0.53685	0.39668
42	O	O32	0.41066	0.55681	0.40256
43	O	O33	0.74108	0.55835	0.39369
44	O	O34	0.06516	0.88094	0.39735
45	O	O35	0.39561	0.87723	0.40125
46	O	O36	0.72923	0.87622	0.39342

Number	Atom	Label	x	y	z
47	O	O37	0.22624	0.07644	0.59817
48	O	O38	0.55039	0.07493	0.60127
49	O	O39	0.88636	0.08281	0.59619
50	O	O40	0.22443	0.41580	0.59844
51	O	O41	0.55374	0.41079	0.60261
52	O	O42	0.88406	0.40371	0.59978
53	O	O43	0.22512	0.74257	0.60054
54	O	O44	0.54768	0.74088	0.60101
55	O	O45	0.88630	0.74174	0.59838
56	O	O46	0.26378	0.16571	0.05652
57	O	O47	0.60677	0.16275	0.06648
58	O	O48	0.92730	0.15639	0.06477
59	O	O49	0.27468	0.49789	0.06617
60	O	O50	0.59363	0.49290	0.06351
61	O	O51	0.93718	0.50200	0.06836
62	O	O52	0.26102	0.82163	0.06526
63	O	O53	0.59815	0.83119	0.05984
64	O	O54	0.93689	0.83100	0.06027
65	Co	Co1	0.37666	0.38404	0.99667
66	Mn	Mn1	0.70843	0.38256	0.00170
67	Mn	Mn2	0.04689	0.38269	0.00791
68	Co	Co2	0.37839	0.71843	0.99928
69	Ni	Ni1	0.71028	0.71838	0.00144
70	Mn	Mn3	0.04533	0.72128	0.99664
71	Co	Co3	0.37821	0.05022	0.00740
72	Co	Co4	0.70947	0.04958	0.99731
73	Co	Co5	0.04309	0.05144	0.99866
74	Mn	Mn4	0.11017	0.18529	0.66113
75	Ni	Ni2	0.44267	0.18891	0.66461
76	Mn	Mn5	0.77266	0.18437	0.66662
77	Co	Co6	0.11091	0.52203	0.66272
78	Ni	Ni3	0.44182	0.52075	0.66463
79	Mn	Mn6	0.77789	0.52310	0.66422
80	Co	Co7	0.10981	0.85348	0.66180
81	Ni	Ni4	0.44050	0.85231	0.66576
82	Co	Co8	0.77427	0.85482	0.65981
83	Mn	Mn7	0.17201	0.09741	0.33263
84	Ni	Ni5	0.50865	0.10082	0.33436
85	Ni	Ni6	0.83735	0.09680	0.33148
86	Ni	Ni7	0.17340	0.43209	0.33170
87	Mn	Mn8	0.50959	0.43963	0.33748
88	Mn	Mn9	0.84362	0.43414	0.32961
89	Ni	Ni8	0.17585	0.76552	0.33749
90	Co	Co9	0.50751	0.76828	0.33358
91	Ni	Ni9	0.84165	0.76777	0.32264

Atomic positions for $x = 0.63$ in $\text{Li}_x\text{Ni}_{1/3}\text{Mn}_{1/3}\text{Co}_{1/3}\text{O}_2$

Number	Atom	Label	x	y	z
1	Li	Li1	0.91417	0.25574	0.49505
2	Li	Li2	0.36850	0.04371	0.49942
3	Li	Li3	0.34613	0.63202	0.50776
4	Li	Li4	0.84303	0.76581	0.48062
5	Li	Li5	0.75796	0.14549	0.16487
6	Li	Li6	0.12431	0.67024	0.16655
7	Li	Li7	0.44330	0.50214	0.16341
8	Li	Li8	0.36827	0.04766	0.84714
9	Li	Li9	0.05813	0.39525	0.84336
10	Li	Li10	0.65376	0.77919	0.83422
11	O	O1	0.29062	0.32592	0.27097
12	O	O2	0.61772	0.32751	0.27160
13	O	O3	0.92860	0.30763	0.26266
14	O	O4	0.28628	0.65882	0.27272
15	O	O5	0.60075	0.64662	0.26670
16	O	O6	0.96578	0.65192	0.26636
17	O	O7	0.28369	0.98497	0.27373
18	O	O8	0.61532	0.98973	0.27095
19	O	O9	0.95132	0.99107	0.26731
20	O	O10	0.99646	0.96520	0.72091
21	O	O11	0.32795	0.96503	0.72630
22	O	O12	0.66384	0.95989	0.72828
23	O	O13	0.99889	0.29714	0.72713
24	O	O14	0.32772	0.29575	0.72579
25	O	O15	0.66273	0.29768	0.72820
26	O	O16	0.99914	0.63188	0.72420
27	O	O17	0.32856	0.62978	0.72615
28	O	O18	0.66560	0.63833	0.72626
29	O	O19	0.15004	0.27710	0.93630
30	O	O20	0.48822	0.26539	0.93833
31	O	O21	0.83006	0.28090	0.93860
32	O	O22	0.15176	0.59827	0.93663
33	O	O23	0.49259	0.61303	0.93653
34	O	O24	0.81877	0.60436	0.93798
35	O	O25	0.16351	0.94512	0.93685
36	O	O26	0.48443	0.94090	0.93862
37	O	O27	0.81649	0.93486	0.93610
38	O	O28	0.05534	0.20873	0.39513
39	O	O29	0.39619	0.20742	0.39938
40	O	O30	0.73607	0.21433	0.39758
41	O	O31	0.06264	0.53685	0.39668
42	O	O32	0.41066	0.55681	0.40256
43	O	O33	0.74108	0.55835	0.39369
44	O	O34	0.06516	0.88094	0.39735
45	O	O35	0.39561	0.87723	0.40125
46	O	O36	0.72923	0.87622	0.39342

Number	Atom	Label	x	y	z
47	O	O37	0.22624	0.07644	0.59817
48	O	O38	0.55039	0.07493	0.60127
49	O	O39	0.88636	0.08281	0.59619
50	O	O40	0.22443	0.41580	0.59844
51	O	O41	0.55374	0.41079	0.60261
52	O	O42	0.88406	0.40371	0.59978
53	O	O43	0.22512	0.74257	0.60054
54	O	O44	0.54768	0.74088	0.60101
55	O	O45	0.88630	0.74174	0.59838
56	O	O46	0.26378	0.16571	0.05652
57	O	O47	0.60677	0.16275	0.06648
58	O	O48	0.92730	0.15639	0.06477
59	O	O49	0.27468	0.49789	0.06617
60	O	O50	0.59363	0.49290	0.06351
61	O	O51	0.93718	0.50200	0.06836
62	O	O52	0.26102	0.82163	0.06526
63	O	O53	0.59815	0.83119	0.05984
64	O	O54	0.93689	0.83100	0.06027
65	Co	Co1	0.37666	0.38404	0.99667
66	Mn	Mn1	0.70843	0.38256	0.00170
67	Mn	Mn2	0.04689	0.38269	0.00791
68	Co	Co2	0.37839	0.71843	0.99928
69	Ni	Ni1	0.71028	0.71838	0.00144
70	Mn	Mn3	0.04533	0.72128	0.99664
71	Co	Co3	0.37821	0.05022	0.00740
72	Co	Co4	0.70947	0.04958	0.99731
73	Co	Co5	0.04309	0.05144	0.99866
74	Mn	Mn4	0.11017	0.18529	0.66113
75	Ni	Ni2	0.44267	0.18891	0.66461
76	Mn	Mn5	0.77266	0.18437	0.66662
77	Co	Co6	0.11091	0.52203	0.66272
78	Ni	Ni3	0.44182	0.52075	0.66463
79	Mn	Mn6	0.77789	0.52310	0.66422
80	Co	Co7	0.10981	0.85348	0.66180
81	Ni	Ni4	0.44050	0.85231	0.66576
82	Co	Co8	0.77427	0.85482	0.65981
83	Mn	Mn7	0.17201	0.09741	0.33263
84	Ni	Ni5	0.50865	0.10082	0.33436
85	Ni	Ni6	0.83735	0.09680	0.33148
86	Ni	Ni7	0.17340	0.43209	0.33170
87	Mn	Mn8	0.50959	0.43963	0.33748
88	Mn	Mn9	0.84362	0.43414	0.32961
89	Ni	Ni8	0.17585	0.76552	0.33749
90	Co	Co9	0.50751	0.76828	0.33358
91	Ni	Ni9	0.84165	0.76777	0.32264

Atomic positions for $x = 0.93$ in $\text{Li}_x\text{Ni}_{1/3}\text{Mn}_{1/3}\text{Co}_{1/3}\text{O}_2$

Number	Atom	Label	x	y	z
1	Li	Li1	0.99814	0.00017	0.49297
2	Li	Li2	0.32689	0.98829	0.50246
3	Li	Li3	0.65994	0.98665	0.49875
4	Li	Li4	0.00389	0.32716	0.49201
5	Li	Li5	0.33246	0.33453	0.49817
6	Li	Li6	0.66458	0.33435	0.49823
7	Li	Li7	0.00170	0.66070	0.49619
8	Li	Li8	0.31971	0.65527	0.49652
9	Li	Li9	0.66349	0.67120	0.49840
10	Li	Li10	0.09693	0.19725	0.16339
11	Li	Li11	0.45571	0.22654	0.16669
12	Li	Li12	0.77825	0.19798	0.17061
13	Li	Li13	0.10893	0.55917	0.17498
14	Li	Li14	0.45857	0.57593	0.16661
15	Li	Li15	0.77588	0.58202	0.17256
16	Li	Li16	0.09913	0.89157	0.16682
17	Li	Li17	0.45471	0.88048	0.17639
18	Li	Li18	0.24604	0.12907	0.83211
19	Li	Li19	0.56644	0.12842	0.83315
20	Li	Li20	0.88355	0.09825	0.83503
21	Li	Li21	0.24968	0.45004	0.83029
22	Li	Li22	0.87909	0.44869	0.83519
23	Li	Li23	0.23463	0.78224	0.82532
24	Li	Li24	0.55778	0.76424	0.84192
25	Li	Li25	0.87508	0.77063	0.84014
26	O	O1	0.34517	0.33063	0.26360
27	O	O2	0.67732	0.36196	0.26060
28	O	O3	0.98683	0.33994	0.25740
29	O	O4	0.33329	0.67453	0.26784
30	O	O5	0.64831	0.65838	0.26549
31	O	O6	0.00687	0.66281	0.26468
32	O	O7	0.34618	0.01759	0.26390
33	O	O8	0.64727	0.99320	0.27079
34	O	O9	0.02944	0.01411	0.25991
35	O	O10	0.00243	0.00351	0.73171
36	O	O11	0.32232	0.98641	0.73249
37	O	O12	0.68941	0.01633	0.73940
38	O	O13	0.00056	0.33202	0.73117
39	O	O14	0.30973	0.32048	0.73787
40	O	O15	0.68606	0.33766	0.73646
41	O	O16	0.99891	0.66476	0.73194
42	O	O17	0.31918	0.66639	0.73155
43	O	O18	0.68675	0.68250	0.73679
44	O	O19	0.11202	0.22374	0.92899
45	O	O20	0.45394	0.22951	0.93089
46	O	O21	0.78263	0.23679	0.92713

Number	Atom	Label	x	y	z
47	O	O22	0.10437	0.55235	0.92753
48	O	O23	0.42803	0.55368	0.93222
49	O	O24	0.78814	0.55485	0.93106
50	O	O25	0.09763	0.87912	0.92653
51	O	O26	0.43288	0.87007	0.92175
52	O	O27	0.78928	0.90066	0.92628
53	O	O28	0.12017	0.21169	0.40968
54	O	O29	0.44891	0.23141	0.40615
55	O	O30	0.77083	0.23115	0.40435
56	O	O31	0.08802	0.53878	0.41182
57	O	O32	0.45498	0.55781	0.40844
58	O	O33	0.77206	0.54615	0.40682
59	O	O34	0.12870	0.89949	0.40560
60	O	O35	0.43503	0.87455	0.41008
61	O	O36	0.76559	0.88330	0.40892
62	O	O37	0.20705	0.10347	0.59286
63	O	O38	0.56679	0.10755	0.59522
64	O	O39	0.88797	0.11307	0.59396
65	O	O40	0.20719	0.43481	0.59122
66	O	O41	0.57225	0.45333	0.59230
67	O	O42	0.88214	0.44190	0.59627
68	O	O43	0.20137	0.76663	0.59274
69	O	O44	0.56549	0.79087	0.60000
70	O	O45	0.88431	0.77619	0.59799
71	O	O46	0.22168	0.11307	0.06485
72	O	O47	0.57550	0.13136	0.07717
73	O	O48	0.90926	0.12648	0.06724
74	O	O49	0.21718	0.44080	0.06547
75	O	O50	0.55096	0.43448	0.06998
76	O	O51	0.89259	0.44598	0.06638
77	O	O52	0.20877	0.76142	0.07423
78	O	O53	0.52398	0.76460	0.07360
79	O	O54	0.90690	0.78329	0.06887
80	Co	Co1	0.33386	0.33364	0.99817
81	Mn	Mn1	0.66450	0.33613	0.99949
82	Mn	Mn2	0.00105	0.33194	0.99737
83	Co	Co2	0.32297	0.66100	0.99965
84	Ni	Ni1	0.66353	0.67440	0.00029
85	Mn	Mn3	0.00318	0.67299	0.99886
86	Co	Co3	0.34477	0.99105	0.00208
87	Co	Co4	0.65610	0.98550	0.00335
88	Co	Co5	0.00484	0.00274	0.99815
89	Mn	Mn4	0.11322	0.22147	0.66320
90	Ni	Ni2	0.44427	0.22284	0.66716
91	Mn	Mn5	0.77748	0.22003	0.66490
92	Co	Co6	0.10688	0.55419	0.66296
93	Ni	Ni3	0.44528	0.55481	0.66676
94	Mn	Mn6	0.77376	0.55764	0.66693

Number	Atom	Label	x	y	z
95	Co	Co7	0.10706	0.88546	0.66415
96	Ni	Ni4	0.44216	0.88635	0.66542
97	Co	Co8	0.78075	0.89339	0.66592
98	Mn	Mn7	0.22571	0.11328	0.33428
99	Ni	Ni5	0.55440	0.11311	0.33684
100	Ni	Ni6	0.88759	0.10752	0.33308
101	Ni	Ni7	0.21823	0.44130	0.33328
102	Mn	Mn8	0.55831	0.45209	0.33528
103	Mn	Mn9	0.88968	0.44500	0.33300
104	Ni	Ni8	0.22484	0.77850	0.33603
105	Co	Co9	0.55173	0.77865	0.33741
106	Ni	Ni9	0.88846	0.78299	0.33473

Atomic positions for $x = 1$ in $\text{Li}_x\text{Ni}_{1/3}\text{Mn}_{1/3}\text{Co}_{1/3}\text{O}_2$

Number	Atom	Label	x	y	z
1	Li	Li1	0.99829	0.99646	0.49648
2	Li	Li2	0.33644	0.99812	0.50242
3	Li	Li3	0.66175	0.99569	0.49738
4	Li	Li4	0.99915	0.32923	0.49626
5	Li	Li5	0.33577	0.33627	0.50141
6	Li	Li6	0.66163	0.32966	0.49974
7	Li	Li7	0.00499	0.66717	0.49849
8	Li	Li8	0.33024	0.66581	0.50097
9	Li	Li9	0.66171	0.66928	0.50173
10	Li	Li10	0.11136	0.22112	0.16899
11	Li	Li11	0.44100	0.21841	0.16227
12	Li	Li12	0.77490	0.21641	0.17079
13	Li	Li13	0.11663	0.55647	0.17177
14	Li	Li14	0.44762	0.55637	0.16177
15	Li	Li15	0.77599	0.55866	0.16536
16	Li	Li16	0.11652	0.89669	0.16513
17	Li	Li17	0.44688	0.88851	0.16879
18	Li	Li18	0.78407	0.89139	0.16828
19	Li	Li19	0.22262	0.10792	0.83380
20	Li	Li20	0.54850	0.09904	0.83526
21	Li	Li21	0.88643	0.10696	0.83443
22	Li	Li22	0.22842	0.45196	0.83361
23	Li	Li23	0.54441	0.44541	0.83616
24	Li	Li24	0.88989	0.44334	0.83486
25	Li	Li25	0.22935	0.78084	0.83066
26	Li	Li26	0.55327	0.77344	0.83669
27	Li	Li27	0.88801	0.78174	0.83464
28	O	O1	0.34144	0.32911	0.25796
29	O	O2	0.67772	0.35326	0.25943
30	O	O3	0.98524	0.32667	0.26167
31	O	O4	0.33707	0.67387	0.26212
32	O	O5	0.65449	0.66064	0.25833
33	O	O6	0.00978	0.65649	0.26153
34	O	O7	0.33282	0.00969	0.25363
35	O	O8	0.66900	0.99449	0.26074
36	O	O9	0.01680	0.00531	0.25325
37	O	O10	0.00106	0.00112	0.73769
38	O	O11	0.32063	0.99141	0.74063
39	O	O12	0.67967	0.00878	0.74272
40	O	O13	0.99612	0.32974	0.73709
41	O	O14	0.31840	0.32462	0.74661
42	O	O15	0.68033	0.33999	0.74228
43	O	O16	0.99740	0.66480	0.73665
44	O	O17	0.31664	0.65899	0.73993
45	O	O18	0.67903	0.67204	0.74208
46	O	O19	0.09934	0.23381	0.91508

Number	Atom	Label	x	y	z
47	O	O20	0.45296	0.21547	0.92208
48	O	O21	0.78325	0.23285	0.92590
49	O	O22	0.10618	0.55486	0.92849
50	O	O23	0.43709	0.55827	0.92382
51	O	O24	0.78401	0.55040	0.92473
52	O	O25	0.11633	0.88257	0.92450
53	O	O26	0.43554	0.87908	0.92667
54	O	O27	0.78334	0.88921	0.91386
55	O	O28	0.10485	0.20418	0.40750
56	O	O29	0.43629	0.23270	0.40935
57	O	O30	0.78056	0.23400	0.41477
58	O	O31	0.09672	0.54517	0.41620
59	O	O32	0.45663	0.56123	0.40971
60	O	O33	0.77147	0.54539	0.40980
61	O	O34	0.12760	0.89715	0.40832
62	O	O35	0.44101	0.88045	0.40789
63	O	O36	0.77465	0.89217	0.40667
64	O	O37	0.20845	0.10519	0.59151
65	O	O38	0.56668	0.11474	0.58762
66	O	O39	0.88796	0.11105	0.59521
67	O	O40	0.20625	0.43367	0.59049
68	O	O41	0.56852	0.45125	0.58782
69	O	O42	0.88195	0.44105	0.59502
70	O	O43	0.20502	0.76798	0.59288
71	O	O44	0.56628	0.78496	0.59261
72	O	O45	0.88552	0.77700	0.59464
73	O	O46	0.22941	0.10422	0.07475
74	O	O47	0.55595	0.11504	0.07166
75	O	O48	0.89911	0.13043	0.08623
76	O	O49	0.21084	0.44932	0.07831
77	O	O50	0.56194	0.43703	0.07713
78	O	O51	0.88669	0.44608	0.07170
79	O	O52	0.22159	0.77826	0.07067
80	O	O53	0.53902	0.76993	0.07805
81	O	O54	0.89808	0.77352	0.07972
82	Co	Co1	0.31945	0.32510	0.99930
83	Mn	Mn1	0.66059	0.33037	0.99991
84	Mn	Mn2	0.00071	0.32910	0.00088
85	Co	Co2	0.32997	0.66439	0.00042
86	Ni	Ni1	0.66695	0.67121	0.00001
87	Mn	Mn3	0.00067	0.67403	0.00025
88	Co	Co3	0.33624	0.99798	0.99841
89	Co	Co4	0.68191	0.98936	0.99953
90	Co	Co5	0.00010	0.01516	0.00067
91	Mn	Mn4	0.11620	0.22319	0.66742
92	Ni	Ni2	0.44395	0.22178	0.66808
93	Mn	Mn5	0.77032	0.21622	0.66588
94	Co	Co6	0.10567	0.55235	0.66554

Number	Atom	Label	x	y	z
95	Ni	Ni3	0.44195	0.55367	0.66669
96	Mn	Mn6	0.77229	0.55613	0.66585
97	Co	Co7	0.10811	0.88663	0.66611
98	Ni	Ni4	0.44179	0.88660	0.66644
99	Co	Co8	0.77799	0.88974	0.66694
100	Mn	Mn7	0.22204	0.10670	0.33099
101	Ni	Ni5	0.55611	0.11462	0.33423
102	Ni	Ni6	0.88522	0.10637	0.33383
103	Ni	Ni7	0.22169	0.44284	0.33481
104	Mn	Mn8	0.55644	0.44961	0.33368
105	Mn	Mn9	0.89137	0.44241	0.33765
106	Ni	Ni8	0.22709	0.77746	0.33461
107	Co	Co9	0.55564	0.77760	0.33406
108	Ni	Ni9	0.89139	0.77767	0.33293

Curriculum Vitae

Personal data

Name: Katja Fröhlich
Nationality: Austria
Date of birth: 23. 07. 1987



Languages

Languages	Reading/Writing/Speaking	Level
German	r/w/s	mother tongue
English	r/w/s	good
Spanish	r/w/s	good

Education and trainings

Date	Name and type of organisation	Focus	Title
01/2014 – present	Technische Universität Wien	Technical Chemistry	PhD
11/2015	School of Biological and Chemical Sciences, Queen Mary University London	Ex situ XRD studies of cathode materials in lithium ion batteries	
2013-2014	Fritz Pusch, Seminar	Management training	
10/2010 – 04/2013	Technische Universität Graz	Chemical and Pharmaceutical Engineering, Chemistry	Dipl.-Ing.
09/2007 – 06/2010	FH Wr. Neustadt, Campus Tulln	Biotechnical Engineering, Bachelor thesis: The bifunctional O ₂ -electrode for zinc-air cells	B.Sc.
10/2005 - 07/2007	Technische Universität Wien	Technical Mathematics	

Work

Date	Name and type of organisation	Position	Focus
12/2017 – today	Electric Drive Technologies, Austrian Institute of Technology GmbH (AIT), Research Institute	Scientist	Battery material characterization and development (experimental, DFT) and crystallography; Project leader (PyroBat); Improvement of industrial electrode coating processes
11/2017 – today	Electric Drive Technologies, Austrian Institute of Technologie GmbH (AIT), Research Institute	Laboratory manager	Material development (experimental & DFT) for battery systems; Implementation of research pilot line for pouch cell production; Laboratory management
10/2014 – 11/2017	Electric Drive Technologies, Austrian Institute of Technologie GmbH (AIT), Research Institute	Junior Scientist	Simulation and material development for battery systems; AIT project lead (SimPore); Laboratory safety management
05/13 – 10/2014	Electric Drive Technologies, Austrian Institute of Technologie GmbH (AIT), Research Institute	Doctoral Fellow	Simulation and material development for Li-ion and Mg-ion batteries, NMC cathodes (synthesis, simulation, crystallography)
02/2010 – 12/2011	Labor für Brennstoffzellensysteme, Technische Universität Graz, University	Project Staff	Bifunctional O ₂ -electrodes for secondary zinc-air batteries

Awards

Best Student Presentation Award

Fröhlich, K., Abrahams, I., Blaha, P., Trifonova, A.: Application of density functional theory for design and understanding of NMC cathodes – in: European Materials Research Society Fall Meeting, Warsaw, 2017.

Best Presentation Award (sponsored by Mars-EV)

Fröhlich, K., Legotin, E., Trifonova, A.: Estimation of Synthesis Parameters for Large-Scale Production of Lithium Nickel Manganese Cobalt Oxide – in: European Materials Research Society Fall Meeting, Warsaw, 2016.

Publications

Fröhlich, K., Abrahams, I., Blaha, P., Trifonova, A.: Application of density functional theory for design and understanding of NMC cathodes – in: European Materials Research Society Fall Meeting, Warsaw, 2017 (Best student presentation award).

Fröhlich, K., Legotin, E., Bärhold, F., Trifonova, A.: New large-scale production route for synthesis of lithium nickel manganese cobalt oxide, *Journal of Solid State Electrochemistry* 21/12 (2017): 3403-3410.

Pichler, F., Fröhlich, K., Stankov, S., Trifonova, A., Cifrain, M.: Thermodynamical modeling of lithium nickel manganese cobalt oxide electrodes, *International Journal of Electronics Communication and Computer Engineering - IJECCE* (2017) 8 (3): 188-193.

Fröhlich, K., Vasilchina, H., Stankov, S., Trifonova, A.: Study of transition metal olivines as intercalation host for rechargeable Mg-ion system – in: 3rd Indo-Austrian Symposium “Advances in Materials Engineering (AME 2016)”.

Fröhlich, K., Legotin, E., Trifonova, A.: Estimation of Synthesis Parameters for Large-Scale Production of Lithium Nickel Manganese Cobalt Oxide – in: European Materials Research Society Fall Meeting, Warsaw, 2016 (Best presentation award by Mars-EV).

Fröhlich, K., Bimashofer, G., Fafilek, G., Pichler, F., Cifrain, M., Trifonova, A.: Electrochemical Investigation of Thermodynamic and Transport Phenomena in LP30 Electrolyte with Various Concentrations of Conducting Salt - *ECS Trans.* 2016 73(1); Published 15 September 2016.

Fröhlich, K., Trifonova, A., Blaha P.: Understanding of electrochemical processes in lithium nickel manganese cobalt oxide using density functional theory. – in: 5th Regional Symposium on Electrochemistry – South East Europe, Pravets, 2015.

Fröhlich, K., Trifonova, A.: Density functional theory as a powerful tool for battery material research. – in: 2nd Workshop in the Advances of Li-Battery Research, Liverpool 2014.

Fröhlich, K., Vasilchina, H., Trifonova, A.: New high voltage cathode material for magnesium-ion secondary batteries – in: Kraftwerk Batterie, Münster 2014.

Fröhlich, K.; Taucher-Mautner, W.; Hacker, V.: Bifunctional Air Electrodes for Electrically Rechargeable Zinc-Air Batteries. - in: 218th ECS Meeting. Las Vegas, USA, 2010.

Weinberger, S.; Rabenstein, G.; Hacker, V.; Fröhlich, K.; Duff, F.; Wede, F. B.; Schutting, S.; Taucher-Mautner, W.; Movrin, D.; Janewit, P.: New Electrode Materials for the Rechargeable Zinc-Air Battery. - in: 62nd Annual Meeting of the International Society of Electrochemistry. Niigata, Japan, 2011.

Weinberger, S.; Rabenstein, G.; Hacker, V.; Fröhlich, K.; Wede, F. B.; Movrin, D.; Schutting, S.; Taucher-Mautner, W.; Duff, F.: Novel Materials for electrically rechargeable Zinc-Air batteries. - in: 4th International Summer School on Advanced Studies of Polymer Electrolyte Fuel Cells. Yokohama Japan, 2011.

Schutting, S.; Taucher-Mautner, W.; Fröhlich, K.; Weinberger, S.; Hacker, V.: Development of Zinc-Electrodes for Rechargeable Zinc-Air Batteries. - in: 14th Austrian Chemistry Days. Linz, 2011.

Movrin, D.; Weinberger, S.; Fröhlich, K.; Wede, F. B.; Hacker, V.: Lifetime Investigations of Bi-Functional Air Cathodes Using Electrochemical Impedance Spectroscopy (EIS). - in: 2011 AIChE Annual Meeting . Minneapolis, 2011.

Hacker, V.; Fröhlich, K.; Taucher-Mautner, W.: Investigations of New Materials for Rechargeable Zinc-Air Batteries. - in: AIChE 2010, Annual Meeting, 2010.